THE UNIVERSITY OF WARWICK

Library Declaration and Deposit Agreement

1. STUDENT DETAILS

Please complete the following:

Full name: ……

University ID number: ……

2. THESIS DEPOSIT

2.1 I understand that under my registration at the University, I am required to deposit my thesis with the University in BOTH hard copy and in digital format. The digital version should normally be saved as a single pdf file.

2.2 The hard copy will be housed in the University Library. The digital version will be deposited in the University's Institutional Repository (WRAP). Unless otherwise indicated (see 2.3 below) this will be made openly accessible on the Internet and will be supplied to the British Library to be made available online via its Electronic Theses Online Service (EThOS) service.
[At present, theses submitted for a Master's degree by Research (MA, MSc, LLM, MS or MMedSci) are not being deposited in WRAP and not being made available via EthOS. This may change in future.]

2.3 In exceptional circumstances, the Chair of the Board of Graduate Studies may grant permission for an embargo to be placed on public access to the hard copy thesis for a limited period. It is also possible to apply separately for an embargo on the digital version. (Further information is available in the *Guide to Examinations for Higher Degrees by Research*.)

2.4 *If you are depositing a thesis for a Master's degree by Research, please complete section (a) below. For all other research degrees, please complete both sections (a) and (b) below:*

(a) Hard Copy

I hereby deposit a hard copy of my thesis in the University Library to be made publicly available to readers (please delete as appropriate) EITHER immediately OR after an embargo period of ……..... months/years as agreed by the Chair of the Board of Graduate Studies.

I agree that my thesis may be photocopied. YES / NO (*Please delete as appropriate*)

(b) Digital Copy

I hereby deposit a digital copy of my thesis to be held in WRAP and made available via EThOS.

Please choose one of the following options:

EITHER My thesis can be made publicly available online. YES / NO (*Please delete as appropriate*)

OR My thesis can be made publicly available only after…..[date] (Please give date)
YES / NO (*Please delete as appropriate*)

OR My full thesis cannot be made publicly available online but I am submitting a separately identified additional, abridged version that can be made available online.
YES / NO (*Please delete as appropriate*)

OR My thesis cannot be made publicly available online. YES / NO (*Please delete as appropriate*)

3. GRANTING OF NON-EXCLUSIVE RIGHTS

Whether I deposit my Work personally or through an assistant or other agent, I agree to the following:

Rights granted to the University of Warwick and the British Library and the user of the thesis through this agreement are non-exclusive. I retain all rights in the thesis in its present version or future versions. I agree that the institutional repository administrators and the British Library or their agents may, without changing content, digitise and migrate the thesis to any medium or format for the purpose of future preservation and accessibility.

4. DECLARATIONS

(a) I DECLARE THAT:

- I am the author and owner of the copyright in the thesis and/or I have the authority of the authors and owners of the copyright in the thesis to make this agreement. Reproduction of any part of this thesis for teaching or in academic or other forms of publication is subject to the normal limitations on the use of copyrighted materials and to the proper and full acknowledgement of its source.

- The digital version of the thesis I am supplying is the same version as the final, hard-bound copy submitted in completion of my degree, once any minor corrections have been completed.

- I have exercised reasonable care to ensure that the thesis is original, and does not to the best of my knowledge break any UK law or other Intellectual Property Right, or contain any confidential material.

- I understand that, through the medium of the Internet, files will be available to automated agents, and may be searched and copied by, for example, text mining and plagiarism detection software.

(b) IF I HAVE AGREED (in Section 2 above) TO MAKE MY THESIS PUBLICLY AVAILABLE DIGITALLY, I ALSO DECLARE THAT:

- I grant the University of Warwick and the British Library a licence to make available on the Internet the thesis in digitised format through the Institutional Repository and through the British Library via the EThOS service.

- If my thesis does include any substantial subsidiary material owned by third-party copyright holders, I have sought and obtained permission to include it in any version of my thesis available in digital format and that this permission encompasses the rights that I have granted to the University of Warwick and to the British Library.

5. LEGAL INFRINGEMENTS

I understand that neither the University of Warwick nor the British Library have any obligation to take legal action on behalf of myself, or other rights holders, in the event of infringement of intellectual property rights, breach of contract or of any other right, in the thesis.

Please sign this agreement and return it to the Graduate School Office when you submit your thesis.

Student's signature: .....…… Date: .....

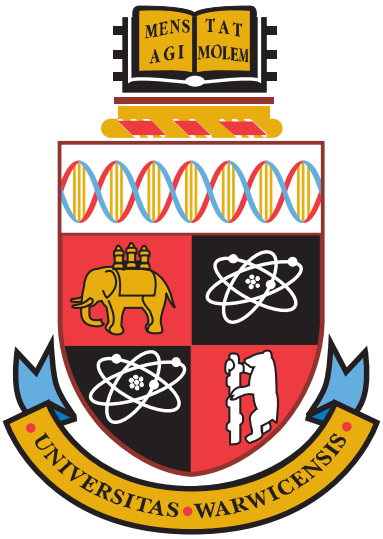

Magnetic Compton scattering studies of novel phases

by

Matthew William Butchers

Thesis

Submitted to the University of Warwick

for the degree of

Doctor of Philosophy

Department of Physics

March 2013

THE UNIVERSITY OF WARWICK

Contents

List of Tables

List of Figures

Acknowledgments

First and foremost I am hugely grateful to my supervisor Jon Duffy. I thank him for introducing me to the wonderful world of Compton scattering and for his constant support and readiness to help in whatever the subject over four years of work.

Away from Warwick in the Compton scattering world I would like to thank Jon Taylor for his banter and support during beamtime and advice during my four years; all I ever needed to learn about magnetism was summarised in a neat little experiment involving a superconducting magnet placed perilously close to a ferromagnetic lab-jack, thanks Jon. I would like to thank Steve Dugdale for his extensive knowledge on all things theory and Sean Giblin for teaching me how to ride a bike (almost).

I am grateful to friends at Warwick who made my PhD experience what it was. Friends like Ian Maskery, Dave #1 and #2, Chris Hussey, Chris Burrows, Dave Duncan, Joao Bento, Steve Parsons, Matt Bradley and Cal Lister, they have been excellent company for Friday evening pub outings. I have been very fortunate to have been able to work with some great people at Bristol University. The Bristol crew over four years: Jude Laverock, Claudia Utfeld, Tom Haynes, Dave Billington and Dave Ernsting are each thanked for valuable explanations and cracking beamtime company!

I gratefully acknowledge the advice and technical help of Dr. Martin Lees, Dr. Tom Hase and Prof. Malcolm Cooper. Dave Sutherland and Andy Sheffield are thanked for all the work they did turning my crude sketches of furnaces and sample holders into devices that inexplicably worked! None of this work would have been possible without the beamline staff at ID15 (ESRF), BL08w (SPring-8) and I06 (Diamond), the hard work of Veijo Honkimäki, Thomas Buslaps, Yoshiharu Sakurai, Masayashi Itou and Sarnjeet

Dhesi is very gratefully acknowledged and they are each thanked.

I thank my Exeter friends (plus extensions!) Joe Pickard, Nikki Chowen, Holly Probert, Suze Clarke, James Pilkington, Ben Aitken who, during my PhD, would always put me up at the weekends, visits and generally be the most lovely group of people anyone could meet.

Finally, I would like to thank my parents whose love and support I have always been able to rely on, for this reason I dedicate this thesis to them.

Matt Butchers

March 2013.

Declarations

This thesis has been submitted to the University of Warwick in support of my application for the admission to the degree of Doctor of Philosophy. It contains an account of my own independent research except where acknowledged in the text. The work was performed in the Department of Physics under the supervision of Dr. J. A. Duffy during the period from October 2008 to September 2012. The research reported here has not been submitted either wholly or in part in this or any other academic institution for the admission to a higher degree. Details of the research to which I have contributed appear in the following publications:

1. Bulk electronic structure of optimally doped $Ba(Fe_{1-x}Co_x)_2As_2$.

   C. Utfeld, J. Laverock, T. D. Haynes, S. B. Dugdale, J. A. Duffy, **M. W. Butchers**, J. W. Taylor, S. R. Giblin, J. G. Analytis, J. Chu, I. R. Fisher, M. Itou, and Y. Sakurai. *Phys. Rev. B.* **101** 064509 (2010)

2. Spin and orbital moments in Fe_3O_4.

   J. A. Duffy, J. W. Taylor, S. B. Dugdale, C. Shenton-Taylor, **M. W. Butchers**, S. R. Giblin, M. J. Cooper, Y. Sakurai and M. Itou. *Phys. Rev. B* **81** 134424 (2010)

3. Ferrimagnetism in Fe-rich $NbFe_2$.

   T. D. Haynes, I. Maskery, **M. W. Butchers**, J. A. Duffy, J. W. Taylor, S. R. Giblin, C. Utfeld, J. Laverock, S. B. Dugdale, J. R. Stewart, Y. Sakurai, M. Itou, C. Pfleiderer, M. Hirschberger, A. Neubauer, W. Duncan and F. M. Grosche *Phys.*

Rev. B. **85** 115137 (2012)

4. Measurements of Magnetic Exchange in Ferromagnet-Superconducting $La_{2/3}Ca_{1/2}MnO_3$ / $YBa_2Cu_3O_7$ Bilayers.
   S. R. Giblin, J. W. Taylor, J. A. Duffy, **M. W. Butchers**, C. Utfeld, S. B. Dugdale, T. Nakamura, C. Visani and J. Santamaria. *Phys. Rev. Lett.* **109** 137005 (2012)

Work with which the author has been associated with which is currently awaiting submission to a refereed journal:

1. Determination of spin density and orbital occupation in $Ca_3Co_2O_6$.
   M. W. Butchers, J. A. Duffy, J. W. Taylor, S. B. Dugdale, T. D. Haynes, S. Agrestini, and M. R. Lees (2012)

2. Determination of the spin density and orbital occupation in the quasi-2D ruthenate $Sr_3Ru_2O_7$: A magnetic Compton study.
   M. W. Butchers, J. A. Duffy, J. W. Taylor, S. B. Dugdale, T. D. Haynes, E. M. Forgan, I. Maskery and R. S. Perry. (2012)

3. Spin and orbital magnetism in UCoGe.
   M. W. Butchers, J. A. Duffy, J. W. Taylor, S. R. Giblin, I. Maskery, C. Stock, S. S. Dhesi and E. D. Bauer. (2012)

4. $4f$ occupation of $TbMnO_3$ determined by magnetic Compton scattering.
   I. Maskery, **M. W. Butchers**, D. Kersh, D. Ernsting, J. A. Duffy, J. W. Taylor, S. R. Giblin, D. O'Flynn, G. Balakrishnan, M. Itou and Y. Sakurai. (2012)

The work described in this thesis has also been presented in talks and posters at the following conferences:

1. Determination of spin density and orbital occupation in the spin chain $Ca_3Co_2O_6$,
   M. W. Butchers, J. A. Duffy, J. W. Taylor, I. Maskery, S. B. Dugdale, T. D. Haynes, S. Agrestini and M. R. Lees. Poster presentation at the IOP Magnetism Group Conference (CRIM), 11th September 2011, University of Durham UK.

2. Determination of spin density and orbital occupation in the spin chain $Ca_3Co_2O_6$, **M. W. Butchers**, J. A. Duffy, J. W. Taylor, I. Maskery, S. B. Dugdale, T. D. Haynes, S. Agrestini and M. R. Lees. Poster presentation at the Condensed Matter and Materials Physics Conference, 14th - 16th December 2010, University of Warwick UK.

3. Spin density in UCoGe, **M. W. Butchers**, J. A. Duffy, J. W. Taylor and C. Stock. Contributed talk and poster at the X-ray Magnetic Scattering Conference, 10th - 11th June 2010, Diamond Light Source UK.

4. Spin moments in metamagnetic materials, **M. W. Butchers**, J. A. Duffy, J. W. Taylor and M. J. Cooper. Poster presentation at the Condensed Matter and Materials Physics Conference, 15th - 17th December 2009, University of Warwick UK.

5. High field magnetic Compton experiments at the ESRF, **M. W Butchers**, J. A. Duffy, J. W. Taylor and M. J. Cooper, Contributed talk and poster at Sagamore XVI Conference on Charge, Spin and Momentum Densities, 23rd - 31st August 2009, Santa Fe, New Mexico USA.

Abbreviations

AFM	antiferromagnet
AMPW	asymmetric multipole wiggler
AO	atomic orbital
ARPES	angle-resolved photoemmision spectroscopy
ASA	atomic sphere approximation
CCD	charge coupled device
CCR	closed-cycle refrigerator
CPA	coherent potential approximation
DDSCS	double differential scattering cross-section
DFT	density functional theory
DLM	disordered local moment
DMFT	dynamical mean-field theory
DZV	double-zeta valence
ECP	effective core potential
EFP	effective fragment potential
EMD	electron momentum distribution
ESRF	European Synchrotron Radiation Facility
FLAPW	full potential linearised augmented plane wave
FM	ferromagnet
FMQCP	ferromagnetic quantum critical point
FP	full potential
FS	Fermi surface
FT	Fourier transform
FWHM	full-width half-maximum
FY	fluorescence yield
GGA	generalised gradient approximation
ITC	intelligent temperature controller
KKR	Kohn-Korringa-Rostiker
LCAO	linear combination of atomic orbitals
LDA	local density approximation
LMTO	linear muffin-tin orbital
LSDA	local spin density approximation

LSDA + U	local spin density approximation + U
MCP	magnetic Compton profile
MCS	magnetic Compton scattering
MO	molecular orbital
NMR	nuclear magnetic resonance
OPC	orbital polarisation correction
PM	paramagnet
PND	polarised neutron diffraction
QCP	quantum critical point
RHF	relativistic Hartree-Fock
ROHF	restricted open Hartree-Fock
SC	superconductor
SCF	self-consistent field
SQUID	superconducting quantum interference device
STO	Slater type orbitals
TEY	total electron yield
TZV	triple zeta valence
UHV	ultra-high vacuum
VRH	variable range hopping
VTI	variable temperature insert
XAS	X-ray absorption spectroscopy
XMCD	X-ray magnetic circular dichroism

Abstract

Magnetic Compton scattering is already a well established technique for the study of ferromagnetic and ferrimagnetic systems. The inelastic collision of a photon with an electron is sensitive to the electron momentum density. Advances in X-ray beam technology with the advent of dedicated synchrotron radiation facilities have allowed the tunability of various properties of the X-ray beam, permitting the weak coupling between it and the spin, **S**, of a target electron to be exploited. Recent developments in sample conditions (field, temperature, pressure) have enabled previously forbidden regions of the phase diagram of a sample to be explored. Other improvements in recent years of the technique combined with novel analytic interpretation via *ab initio* band structure calculations allow for a deeper understanding of the ground state to be gained from magnetic Compton scattering experiments. In this thesis, the unique properties of magnetic Compton scattering are applied to novel materials where high magnetic fields are essential and in conjunction with modelling methods the underlying electronic structure is elucidated.

In the first study, investigations into the spin density of two complex oxides, $Ca_3Co_2O_6$ and $Sr_3Ru_2O_7$, are detailed. $Ca_3Co_2O_6$ is a frustrated, metamagnetic spin chain compound which has been the subject of much investigation over recent years. From magnetic Compton scattering experiments, direct measurements of the bulk spin moment (1.78 $\pm$ 0.05 μ_B for 2 T and 3.93 $\pm$ 0.05 μ_B at 5 T and 7 T) confirms the existence of a large unquenched Co orbital moment (1.3 $\pm$ 0.1 μ_B at 7 T) together with an oxygen spin moment of $\approx$ 0.9 μ_B. Calculations from which theoretical magnetic Compton profiles have been extracted are shown to be in good agreement with the experimental data and unexpectedly reveal the existence of a Fermi surface in this system. With regards to the orbital occupation, molecular orbital calculations on the active $[CoO_6]^{9-}$ cluster are discussed and from which the Co 3*d* orbitals responsible for the observed electronic and magnetic behaviour are determined. It is suggested that it is the double occupation of the $d_{x^2-y^2,xy}$ orbital that gives rise to the large unquenched orbital moment. The second magnetic oxide, $Sr_3Ru_2O_7$, is a model system displaying a metamagnetic quantum critical point (MMQCP) reached via field tuning. Magnetic Compton profiles were measured in the metamagnetic phase along three crystallographic directions. LSDA band structure calculations and molecular orbital simulations were performed to reveal the extent of Ru 4*d* - oxygen 2*p* hybridisation, and also determine

the occupation numbers of the t_{2g} and the e_g orbitals in the metamagnetic phase. The oxygen spin density is estimated to be approximately 30 - 31 % of the total spin density in agreement with NMR results. Furthermore, a spin moment of 0.70 $\pm$ 0.03 μ_B in the *ab*-plane reveals a negligible orbital moment.

In the second study, the magnetic properties of the uranium superconductors UCoGe and UGe_2 are presented. For UCoGe, the spin and orbital moments have been measured using a combination of magnetic Compton scattering, X-ray magnetic circular dichroism and density functional calculations to reveal the magnetic structure of this ferromagnetic superconductor. The compound is found to be a weak ferromagnet with a small total moment of 0.16 $\pm$ 0.01 μ_B. The uranium spin and orbital contributions nearly cancel, it is suggested that the uranium 5*f* electrons carry a spin moment of $\approx$ -0.30 μ_B and an opposing orbital moment of $\approx$ 0.38 μ_B, these values imply a strongly delocalised system. This is in contradiction with recent *ab initio* calculations which over-estimate the moments and also at odds with recent polarised neutron diffraction data. In addition to the uranium magnetism, there exists a cobalt spin moment of 0.06 μ_B anti-aligned to the uranium spin moment induced via significant 3*d*-5*f* hybridisation which could be responsible for delocalising the uranium electrons. The magnetic structure is verified by X-ray magnetic circular dichroism measurements at the cobalt $L_{2,3}$ edges which confirm that the uranium and cobalt moments are anti-parallel. For the compound UGe_2, temperature dependent magnetic Compton scattering experiments were conducted to investigate the shape of the momentum density across the T^* phase transition. It is this transition which is thought to play a vital part in the observed superconducting phase. A change in the orbital occupation is inferred from a small shape change in the magnetic electron distribution with increasing temperature, lending evidence to a Fermi surface driven phase transition. For both compounds attention has been given to the degree of delocalisation of the uranium 5*f* electrons.

In the final study, results from high temperature magnetic Compton scattering experiments on the Invar alloys $Fe_{1-x}Ni_x$ and pure nickel are presented. The aim of which is to investigate any change in the shape of the spin-polarised momentum distribution. The spin density of $Fe_{1-x}Ni_x$ (x = 0.20, 0.35 and 0.60) was first studied over a temperature range 50 - 450 K to investigate a possible change in band structure associated with the mechanism behind the Invar effect. The magnetic Compton profiles for the non-Invar compositions (x = 0.20 and 0.60) show no significant change in the electron momentum distribution in accordance with a similar study on Fe_3Pt. However, the Invar composition ($x = 0.35$) shows a distinct change between the high temperature and low temperature momentum density. We associate this with a change in the electron momentum density occupation. In addition, the size of the occupation change is shown to be temperature dependent. The study into the spin density of pure nickel within the ferromagnetic phase and at its Curie temperature revealed no change in the momentum distribution in the two temperature regimes along the [100] crystal direction. This observation is in accordance with a Stoner-like reduction in the exchange-splitting with no enhancement or reduction of the *sp*-hybridisation, but at odds with other experimental work.

Chapter 1

Introduction

1.1 Motivation

This thesis details investigations into a wide range of strongly correlated electron systems using the technique of magnetic Compton scattering. Strongly correlated electrons are a result of the interaction and competition between different properties of an electron system, such as the spin, orbital or lattice degrees of freedom. The effect of strong correlation between electrons can manifest itself as long range magnetic order, where the electron spins of atoms align. Magnetism offers us a glimpse into the way electrons interact with each other and their environment, it can be used as an indication of spin ordering and electron localisation and as such is a vast area of research in solid state physics.

Magnetism through the elements is a very varied phenomenon. The first row of transition metal elements are characterised by their large electronic wavefunctions, resulting in itinerant magnetism which is usually only composed of the spin of the electron, **S**. As well as **S**, magnetism can arise from the motion of an electron, **L**, which is generally negligible for the first row transition metals. Lanthanide magnetism is characterised by the far more localised extent of their wavefunctions. This localised behaviour typically leads to a large orbital moment as well as a spin moment [1]. Actinide

magnetism lies somewhere in between, and can be localised or itinerant depending on the crystal structure, often giving rise to interesting behaviour [2].

There are many techniques available to investigate the magnetic behaviour of solids. There are bulk techniques such as superconducting quantum interference device (SQUID) and vibrating sample magnetometry, these bulk techniques measure the *total* magnetisation, **J** ($\mathbf{J} = \mathbf{S} + \mathbf{L}$). Bulk techniques are used to investigate the *macroscopic* behaviour of the magnetisation and are widely employed for the magnetic characterisation of materials. To properly understand the physics of a strongly correlated electron systems however it is vital to understand the behaviour of *both* spin and orbital components.

As well as bulk magnetisation techniques there are also *microscopic* techniques for probing magnetism on an atomic scale, used in particular to separate the total moment, **J**, into the spin and the orbital contributions. Techniques to separate **S** and **L** exist which utilise the scattering or absorption of a particle which possesses sensitivity to an atoms magnetic moment. Neutrons possess a finite magnetic moment which interacts with the magnetic moment of an atom. The neutron measures the *total* moment, although in principle **S** and **L** can be extracted through further modelling. X-rays are also sensitive to the magnetic moments of an atom and as such there are various spectroscopies which can be used to separate **S** and **L**, this is due to the different ways the way the photon **E** and **B** fields interact with the electrons spin and orbital degrees of freedom. The magnetic probe used for the majority of the work in this thesis is the X-ray magnetic Compton scattering technique which is based on the Compton effect.

1.2 The Compton effect

The Compton effect was discovered in 1923 [3] by Arthur Holly Compton and is the observation that when a high energy photon is inelastically scattered from an electron, the energy of the scattered photon is dependent on the angle of scattering, ϕ, and the

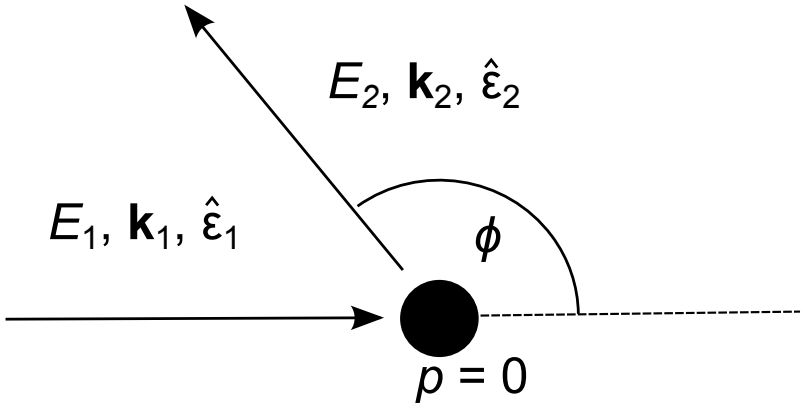

Figure 1.1: Schematic diagram of a photon being Compton scattered from a stationary electron.

initial energy of the photon, E_1. The scattering is shown in Fig 1.1 and describes the equation

$$E_2 = \frac{E_1}{1 + (E_1/m_e c^2)(1 - \cos\phi)}. \tag{1.1}$$

Here E_2 is the energy of the X-ray after scattering, m_e the electron rest mass and c is the velocity of light. Even the earliest experiments, however, showed a broadening of the Compton peak at E_2 beyond the instrument resolution. This broadening is due to the motion of the electrons which Doppler broaden the scattered X-rays, as such, Compton scattering not only provides information about the scattering process through the energy shift $E_2 - E_1$, but also provides information on the electronic motion of electrons in a sample.

The link between Compton scattering and the motion of the electrons makes it possible to probe the momentum distribution of the electrons in a target. The momentum distribution is an invaluable measurement as the shape reflects *all* of the electronic wavefunctions in a crystal measured in momentum space.

An extension to the Compton technique is *magnetic* Compton scattering which utilises a degree of circular polarisation in the X-ray beam. The circular polarised light couples to the spin of an electron. Quantitative information on the spin moment of a

sample, **S**, can be extracted precisely and without the need for further modelling. With knowledge of the spin moment and a bulk moment from bulk techniques, a value of the orbital moment, **L**, can be deduced, thus a complete picture of the magnetism may be obtained.

The capabilities of the X-ray magnetic Compton technique are that:

- It provides an accurate measurement of the spin moment of a ferromagnetic system, see Refs. [4, 5, 6] for prototypical examples.

- A magnetic Compton scattering experiment yields the electron momentum distribution of spin polarised electrons through what is called the magnetic Compton profile. With modelling techniques such as band-structure calculations and molecular orbital calculations, the contribution each magnetic electron orbital makes to the magnetic Compton profile can be determined. Understanding which electrons contribute to the moment help explain the energy ordering of the orbitals and can elucidate the underlying electronic structure. The electron wavefunction overlap of one electron with another (hybridisation) is hugely important when discussing the origins of magnetism in a crystal, this hybridisation is also reflected in the shape of the magnetic Compton profile. See Refs. [7, 8, 9, 10] for prototypical examples.

- There is no restriction on the sample conditions unlike other techniques described in §4.4, for example, there is no requirement on a magnetic Compton scattering experiment to be performed in ultra-high vacuum (UHV), at low temperatures, or even have a clean surface. Single crystal, amorphous alloys, liquids are all measured routinely. See Refs. [11, 12, 13] for prototypical examples.

1.3 Organisation of the thesis

Detailed in this thesis are investigations into three classes of strongly correlated electron systems where the magnetism is fundamental to understanding the underlying physics. In chapter 2 the principles of magnetism in solid state physics are outlined with reference to how magnetism is influenced by a crystal lattice. To fully understand magnetism in a crystal lattice one must have an understanding of the underlying band structure of a system which stems from the many body electron problem. Methods for investigating the many body electron problem are introduced at the end of chapter 2.

In chapter 3, the theory of magnetic Compton scattering is detailed and how a measurement of the magnetic electron momentum density is deduced from a magnetic Compton scattering experiment is explained. In chapter 4, the experimental considerations of how one can conduct a magnetic Compton experiment are detailed. Other methods and complementary techniques are also introduced with reference to how they are used in this thesis.

In chapter 5, magnetic Compton scattering studies on two strongly correlated oxides are presented. The orbital occupation of the magnetic electrons in $Ca_3Co_2O_6$ is first investigated with the aim of explaining the unusual electronic behaviour. Secondly, $Sr_3Ru_2O_7$ is investigated to better understand which electrons take part in it's metamagnetic transition by determining the orbital occupation with molecular orbital calculations.

In chapter 6, magnetic Compton scattering and X-ray magnetic circular dichroism studies into a very rare phase of matter where magnetism and superconductivity coexist are detailed. Spin and orbital moments in UCoGe are investigated to better understand the localisation of the superconducting / magnetic electrons. This is followed by a study into the temperature dependence of the shape of the magnetic Compton profiles of UGe_2 with an aim to determine the existence of a change in band structure across the T^* magnetic phase transition.

In the final experimental chapter, high temperature magnetic Compton scattering experiments are presented. Firstly, in $Fe_{1-x}Ni_x$ the shape of the magnetic Compton profile is investigated to try to explain the observed magneto-elastic behaviour. In nickel, the shape of the magnetic Compton profile is used to investigate the exchange splitting at it's Curie point to help resolve inconsistencies in previously published work. Special mention is given to the sample heaters designed and made for these experiments.

Chapter 2

Magnetism and electronic structure calculations

This thesis details magnetic Compton scattering studies on a wide range of materials possessing a huge variety of properties. The underlying physics of these properties is due to the arrangement, motion and interaction of the electrons with each other and also the lattice. The true behaviour of a materials electronic structure cannot be properly appreciated without a firm understanding of quantum mechanics. The quantum nature of electrons in solids is the subject of many solid state physics textbook (see for examples Refs. [1, 14, 15]). The focus of this chapter is not to detail the entire history of solid state physics but instead to highlight the important concepts fundamental to the work described in this thesis.

The first section of this chapter outlines the origins of magnetism, summarising how the quantum concept of exchange can dictate the arrangement of spins. The chapter continues with how electrons in a real crystal environment have their magnetic properties altered when compared to those of an ideal free atom. The chapter concludes by introducing ways of predicting how a collection of electrons behave inside a crystal. As a start, the many-body electron problem is introduced. Two methods for solving the many-body electron problem used in this thesis are briefly outlined, an orbital wavefunction

approach and density functional theory. Special mention is given to the applicability, advantages and use of each of these methods and how these methods can be used to elucidate the magnetism of a system.

2.1 Magnetism

2.1.1 Magnetic moments

Magnetism in atoms is associated with the total angular momentum **J** of an electron. For a single atom with only one electron $\mathbf{J} = \mathbf{L} + \mathbf{S}$, where **L** describes the orbital angular momentum associated with the motion of an electron and **S** is the intrinsic spin property.

There are various forms of magnetism in solids, some of which are shown in Fig. 2.1. The simplest to understand is diamagnetism, which is exhibited by all materials. The origin of diamagnetism can be understood with an appreciation of Lenz's Law, which states that when a magnetic field **H** is applied to an electronic system, the motion of the orbitals act to create a field which opposes the field creating it. The result of this is a magnetic moment *only* when there is a field applied. In a paramagnetic material the electron spins are randomly oriented resulting in no net moment. With a field applied however the electron spins align with the direction of the field thereby possessing a moment in that direction. Again, this phenomena only contributes in the presence of an applied field.

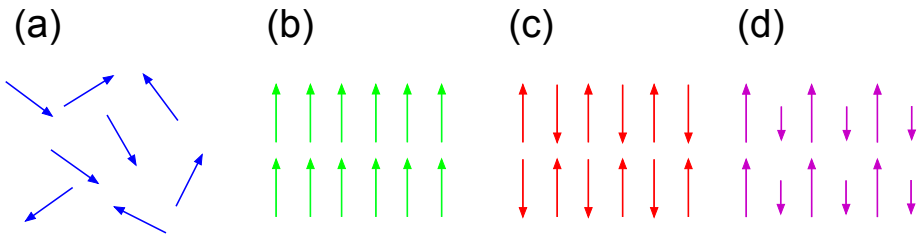

Figure 2.1: The arrangements of spins in a (a) paramagnetic (b) ferromagnetic (c) anti-ferromagnetic and (d) ferrimagnetic materials.

In strongly correlated materials, inter-electronic interactions can result in the collective phenomena of spontaneous magnetism which requires some level of "communication" between neighbouring spins to produce long range magnetic order. In 1907, Pierre Weiss inferred from empirical evidence that the alignment of magnetic moments in a ferromagnetic material was a result of an internal field, H_W, that was proportional to the magnetisation. Weiss deduced that at the temperature at which the spontaneous magnetisation disappears, T_C (the Curie temperature) the thermal energy k_BT of atomic moments becomes greater than the interaction energy with the Weiss field and the spontaneous magnetisation is destroyed. The origin of this "communication" remained unsolved until Heisenberg and the advent of quantum mechanics [15].

2.1.2 Direct exchange

In 1928, Werner Heisenberg showed that magnetic ordering can occur due to the electrostatic interactions between magnetic moments. It is a manifestation of Pauli's exclusion principle and as such has no classical analogue. Direct exchange is described within the Heisenberg model as

$$\hat{\mathscr{H}} = -\sum_{ij} J_{ij}\mathbf{S}_i \cdot \mathbf{S}_j, \tag{2.1}$$

where $\hat{\mathscr{H}}$ is the Heisenberg Hamiltonian, J_{ij} is the exchange energy constant and $\mathbf{S}_{ij}$ are the spin vectors for electron i and j. The idea behind the exchange energy is that the Pauli principle imposes a constraint on the symmetry of the total electronic wavefunction. Particles with half-integer spin such as electrons are called fermions and must obey Pauli's exclusion principle, that principle requires that upon the interchange of two electrons positions, the total electronic wavefunction must change sign. The total electronic wavefunction may be decomposed into the product of a spatial part and a spin part. If the symmetry of the spatial part of the wavefunction is symmetric it follows that the spin part must therefore be anti-symmetric and *vice versa*.

If the value of J_{ij} in Eq. 2.1 is positive a system will order ferromagnetically (spins aligned Fig. 2.1(b)). A negative value of the exchange constant will, however, result in an anti-ferromagnetic ground state (spins anti-aligned Fig. 2.1(b)). The situation for two non-interacting electrons is clearly far too simplistic to explain magnetic order in a real material. The important aspect to appreciate is that Pauli's requirement for an anti-symmetric wavefunction dictates the orientation of the spin and therefore imposes an energy difference between the two alignments. This effect requires overlap between the two neighbouring electronic wavefunctions and therefore cannot be used to explain magnetic order in localised cases such is observed in $4f$ electron systems, which require a different model to explain the magnetism.

2.1.3 Indirect exchange

The process of indirect exchange is valid where there is no orbital overlap between aligned electrons, yet the spins still feel the effect of the neighbouring spins. There are various kinds of indirect exchange, for example:

- Superexchange: superexchange occurs between two magnetic ions through the interaction with a non-magnetic ion situated between them. Fig. 2.2 shows the case of two magnetic d-metal ions (M) separated by a non-magnetic oxygen ion with two free p-electrons (O). The arrangement of the oxygen p-electrons in this

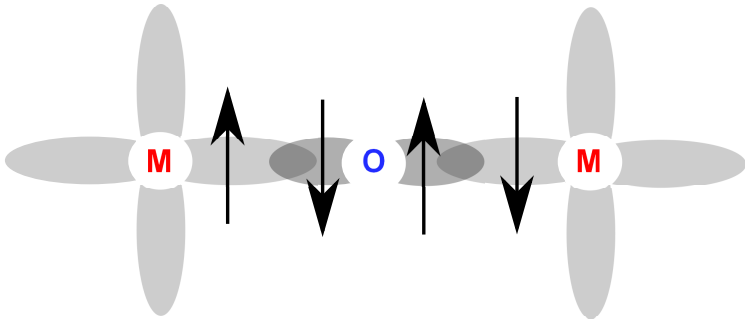

Figure 2.2: The case of two magnetic d-metal ions separated by a non-magnetic oxygen ion with two free p-electrons.

case dictates the ordering of the *d*-electron metal ions. If the two *d*-metal ions were of the same spin then the overlap of those wavefunctions with the oxygen wavefunctions would require that the oxygen *p*-electrons should be opposite to the *d*-electron spin but the same as each other and thus unfavourable. Pauli's exclusion principle in this case would limit the movement of these *p*-electrons and thus this configuration is higher in energy. An anti-ferromagnetic arrangement however, allows for the *p*-electrons to be of opposite spin resulting in a lower energy configuration. Rules to predict the spin configuration in transition metal - oxygen ion systems were developed by Goodenough and Kanamori [16] and depend on the *M*-*O*-*M* angle and the respective occupancies of the two metal ions.

- Ruderman-Kittel-Kasuya-Yosida (RKKY) exchange interaction: This exchange type occurs in metals with localised magnetic moments. The exchange is mediated via the valence electrons. The radial dependence of the exchange energy constant J_{RKKY} is complicated and often leads to non-trivial magnetic structures. The RKKY interaction is observed in rare earths such as gadolinium as an explanation to the observed magnetic ordering.

2.1.4 Magnetism in real systems.

The coupling between spin, orbital and crystallographic degrees of freedom in a magnetic crystal can be very strong. As such, in a real magnetic system the crystal can greatly influence the magnetic properties.

There are two energy scales that are of importance in a magnetic crystal: the spin-orbit energy E_{SO} and the crystal-field energy E_{CF}. E_{SO} is a consequence of relativistic quantum mechanics whereby the spin-orbit coupling links the motion of an electron to its spin, and can be very large the heavier elements. E_{CF} is the energy of the interaction of the crystal field and the electronic wavefunction. It is dependent on the geometry and the repulsion between the ions. The strength of the crystal field is a particularly important factor in *d*-electron systems where the electron wavefunctions

are large.

Roughly speaking it is the balance of these energy scales which determine how a magnetic system behaves and leads to three situations:

- $E_{\mathrm{SO}} < E_{\mathrm{CF}}$: This is usually the case for 3*d* transition metals. The spatially extended orbitals mean that the crystal field tends to arrange the energy levels and are best explained in terms of ligand theory; a powerful model which considers the ground state as molecular orbitals [17].

- $E_{\mathrm{SO}} > E_{\mathrm{CF}}$: This is usually the case for 4*f* metal ions, where due to the far more localised radial extent of the wavefunction the magnetism is best described through the coupling of spin and orbital momenta by the Russell-Saunders coupling scheme [1].

- $E_{\mathrm{SO}} \approx E_{\mathrm{CF}}$: This is usually the case for 5*f* electron systems. The competition between the energy scales is often responsible for the novel behaviour observed in actinide systems [18].

2.1.4.1 Quenching of the orbital moment

In a *d*-electron system where E_{CF} is dominant, normally degenerate orbitals are split in energy. The effect of removing this degeneracy of the otherwise free-atom like states often results in a vanishing value for the orbital moment. The reason for this is that the angular momentum operator for a wavefunction, $\hat{\mathscr{L}}$, is a complex operator, $\hat{\mathscr{L}} = -i\hbar \times \nabla$. For the degenerate case (i.e. in the absence of a crystal field or spin-orbit coupling), one is free to choose any *complex* linear combination of atomic wavefunctions as a new basis - leading to a real, finite value for the orbital moment. However, in the presence of a crystal field, the degeneracy of the orbitals is lifted - this forces one to use *real* wavefunctions. Knowing the operator is imaginary but with the constraint that the total angular momentum operator is Hermitian, the total orbital moment must vanish [19].

In order for a degenerate electron to generate an orbital angular momentum it must be possible to transform the orbital it occupies into an entirely equivalent and degenerate orbital by rotation [20]. In an octahedral environment the crystal field splits the normally degenerate *d*-electrons into the t_{2g} and e_g subsets as shown in Fig. 2.3. The t_{2g} orbitals can be rotated into each other via 90° rotations thus possessing an orbital angular momentum. The e_g set, however, are different shapes and therefore never possess an orbital angular momentum. There is one final consideration to make, and that is based on Pauli's exclusion principle which follows that a rotation can only occur if the orbital is rotating into an *unoccupied* orbital.

In reality, the orbital angular momentum may not be completely quenched, because the spin-orbit coupling cannot always be ignored. This is usually the case for 4*d* rare-earths and actinides, where the strength of the spin-orbit interaction can be comparable to that of the crystal field energy. Additionally, by coupling the spin to the orbital motion which is influenced by the crystal field, the spin-orbit coupling provides a linking between the spin and the crystal axes. It is this coupling that drives the phenomenon

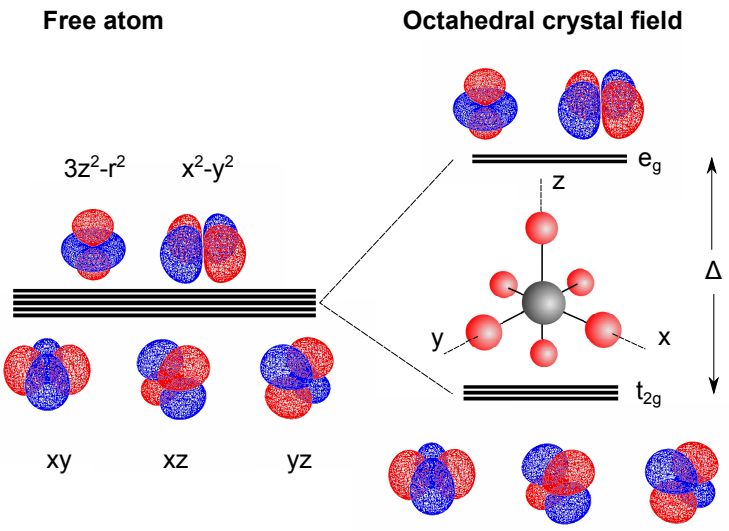

Figure 2.3: Shapes and energy levels of the *d*-electron orbitals. Degenerate in the free-atom case and split into t_{2g} and e_g levels when subject to an octahedral crystal field. Where Δ is the crystal field splitting energy.

of magnetic anisotropy arises.

Methods for calculating the magnetic properties of crystals have been developed over the decades. These methods solve the interacting, many body electron problem introduced in the next section.

2.2 Electronic structure calculations

The aim of this section is to detail two schemes for calculating the electronic structure of materials. The basis of the problem stems from the need to solve the Schrödinger equation for *all* the electrons in a unit cell inside a periodic potential determined by the three dimensional positions of the atomic cores.

The Hamiltonian for a collection of electrons and nuclei is shown in Eq. 2.2. The second line shows that the total Hamiltonian can be split into a kinetic term for electrons, a potential term for the interaction of an electron with a nucleus and a Coulomb term, sometimes called the Hartree term, which describes the interaction of one electron with another. There is an additional term due to the kinetic energy of the nucleus, however the Born-Oppenheimer approximation assumes that the ionic cores are frozen and thus is not included.

$$\begin{aligned} \hat{\mathscr{H}}\psi_i(\mathbf{r}_i) &= \varepsilon_i\psi_i(\mathbf{r}_i) \\ \hat{\mathscr{H}} &= \hat{\mathscr{T}}_{\mathrm{el}} + \hat{\mathscr{U}}_{\mathrm{el-nucl}} + \hat{\mathscr{U}}^{C}_{\mathrm{el-el}}, \end{aligned} \tag{2.2}$$

where ε_i and ψ_i are the eigenvalues and eigenfunctions of the many-body Hamiltonian $\hat{\mathscr{H}}$. $\hat{\mathscr{T}}_{\mathrm{el}}$, $\hat{\mathscr{U}}_{\mathrm{el-nucl}}$ and $\hat{\mathscr{U}}^{C}_{\mathrm{el-el}}$ are the kinetic energy operator for the electrons, the potential energy of the electron-nuclei interaction and the Coulomb potential respectively. The expanded Hamiltonian for the many body problem is therefore

$$\left[-\frac{\hbar}{2m_e}\nabla^2 + \hat{\mathscr{U}}_{\mathrm{el-nucl}}(\mathbf{r}) + \frac{1}{4\pi\epsilon_0}\sum_j{}' \int \frac{e^2}{|\mathbf{r}-\mathbf{r}\,'|}\left|\psi_j(\mathbf{r}\,')\right|^2 \,\mathrm{d}^3r'\right]\psi_i(\mathbf{r}_i) = \varepsilon_i\psi_i(\mathbf{r}_i), \tag{2.3}$$

where ϵ_0 is the permittivity of free space. One complication to solving Eq. 2.3 is that each electron has three spatial dimensions so that the problem scales vastly as the number of electrons increases. Methods for approaching this many body problem are

detailed below.

2.2.1 Wavefunction methods

The basic idea of the Hartree-Fock wavefunction method is that we require a solution for the true eigenvalues ε_i and eigenfunctions $\psi_i(\mathbf{r})$ of Eq. 2.3. We start by constructing a total wavefunction of N, non-interacting particles of the general form

$$\Psi_{\mathrm{HP}}(\mathbf{r}_1, \mathbf{r}_2 ... \mathbf{r}_N) = \chi_1(\mathbf{r}_1)\chi_2(\mathbf{r}_2)..\chi_N(\mathbf{r}_N) = \prod_i \chi_i(\mathbf{r}_i). \tag{2.4}$$

Eq. 2.4 is known as the *Hartree Product* and was introduced by D. R. Hartree to calculate approximate wavefunctions and energies for atoms and ions . Whilst the functional form is fairly convenient, it has at least one major shortcoming, it does not describe the properties of electrons as required by quantum mechanics. It is known that:

- two electrons cannot occupy the same state
- for spin orbitals the sign of the wavefunction is required to swap under interchange of their positions.

Neither of these conditions are satisfied by the Hartree Product. This was rectified by Slater and Fock who proposed the *Slater determinant* [21]. It can be seen in Eq. 2.5 in the determinant of χ_1 and χ_2, that if we interchange $\mathbf{r}_1$ and $\mathbf{r}_2$ the sign of the wavefunction changes and that if $\mathbf{r}_1 = \mathbf{r}_2$ the determinant vanishes

$$\Psi_{\mathrm{SD}} = \frac{1}{\sqrt{N!}} \begin{vmatrix} \chi_1(\mathbf{r}_1) & \chi_2(\mathbf{r}_1) & \cdots & \chi_N(\mathbf{r}_1) \\ \chi_1(\mathbf{r}_2) & \chi_2(\mathbf{r}_2) & \cdots & \chi_N(\mathbf{r}_2) \\ \vdots & \vdots & \ddots & \vdots \\ \chi_1(\mathbf{r}_N) & \chi_2(\mathbf{r}_N) & \cdots & \chi_N(\mathbf{r}_N) \end{vmatrix}. \tag{2.5}$$

The solutions to the Schrödinger equation for free atoms are the atomic orbitals, which describe the radial and angular distribution of each atomic state. Molecular theory

allows one to be able to describe each one electron molecular orbital (χ_i) as a linear combination of atomic orbitals (LCAO). This combination allows for bonding/anti-bonding effects to be accounted for and can be far more instructive for systems with significant orbital overlap. In general, each one electron molecular orbital wavefunction is described by

$$\chi_i(\mathbf{r}) = \sum_j c_{i,j}\phi_{i,j}(\mathbf{r}), \tag{2.6}$$

where $\phi_j(\mathbf{r})$ is an atomic orbital (AO) (or basis function), and c_j is the weighting coefficient for each AO. In a quantum chemistry calculation the variational theorem then minimises the self-consistent field (SCF) energy and calculates these coefficients by solving

$$\varepsilon_{\mathrm{SD}} = \left\langle \psi_{\mathrm{SD}} | \hat{\mathscr{H}} | \psi_{\mathrm{SD}} \right\rangle. \tag{2.7}$$

2.2.1.1 Basis sets

In a molecular orbital calculation the single electron wavefunctions are approximated by a set of functions $\phi_1(\mathbf{r}), \phi_2(\mathbf{r}), ..., \phi_j(\mathbf{r})$. The molecular orbital is defined as $\chi_i(\mathbf{r}) = \sum_j c_{i,j}\phi_{i,j}(\mathbf{r})$. The aim is to find the expansion coefficients for each atomic orbital. This single electron wavefunction, $\phi_j(\mathbf{r})$, is called a basis function. Although these functions can vary greatly in their complexity, they all follow the general form

$$\phi_{i,j}(\mathbf{r}) = f_{n,l}(\mathbf{r})Y_{n,l}(\theta,\varphi). \tag{2.8}$$

Where $f_{n,l}(\mathbf{r})$ describes the radial dependence of the atomic orbital and $Y_{n,l}(\theta,\varphi)$ describes the angular dependence. The basis functions used in this thesis were obtained from "The Basis Set Exchange" website [1]. Tabulated triple zeta valence (TZV) basis functions were used for cobalt in §5.2, and ruthenium in §5.3. Triple zeta sets use three

[1] https://bse.pnl.gov/bse/portal.

basis functions per one electron AO. For ruthenium the core electrons were replaced by an effective core potential (ECP) as it is assumed that the core electrons are not important for describing the bonding. This helps to reduce the computational effort.

2.2.1.2 Cluster calculations

Computational schemes have been developed over the past few decades for calculating the quantities in Eq. 2.7. Molecular orbital calculations presented in this thesis were performed using the quantum chemistry program GAMESS, in which the molecular orbitals are computed via the Hartree-Fock scheme. For a full description see Ref. [22].

For the cases described in later chapters (§5.2 and §5.3), the magnetically active part of the unit cell is represented by *ab intitio* clusters i.e. for $Ca_3Co_2O_6$ the magnetic cluster is the $[CoO_6]^{9-}$ cluster and for $Sr_3Ru_2O_7$ a $[RuO_6]^{8-}$ cluster is used. This immediately places a limitation on the wide scale applicability of the approach. If the system is known to have many magnetic interactions via many different crystallographic sites, the problem becomes too complex to solve through this method. The reasonable assumption that magnetic effects are due to a single crystallographic site and coordinated cations has to be made. This is simply the magnetic ion and its nearest coordinated oxygens. These oxide clusters are called the *ab initio* atoms and are the only atoms in the calculation to be expanded by use of a basis set.

The other atoms in the unit cell are treated as point charges situated on crystallographic sites creating a crystal potential. This potential acts to affect the spatiality of the *ab initio* atomic wavefunctions. The value of the point charges was the formal charge of the ion in question except on the sides, edges and corners of the unit cell where the charges were a half, quarter and an eighth respectively of their formal charge ensuring charge neutrality throughout the crystal.

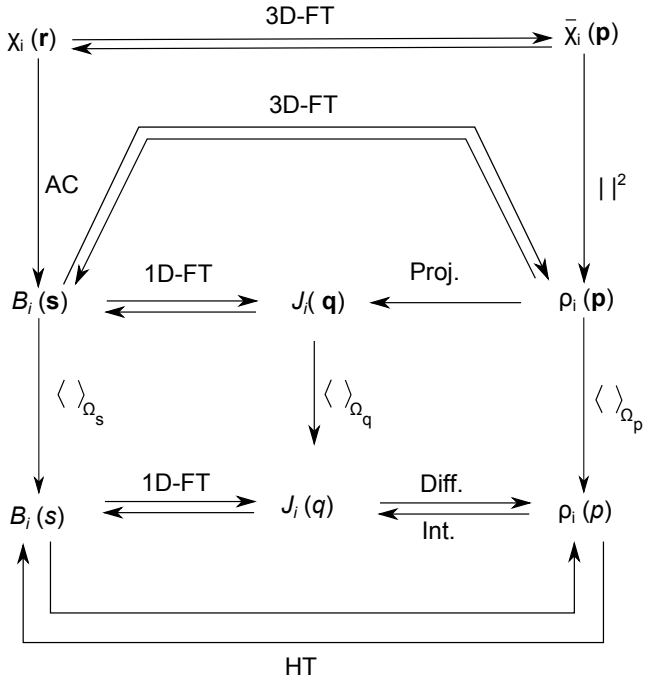

Figure 2.4: Scheme for the calculation of directional and spherically averaged Compton profiles from orbital contributions, where j is the orbital index. $||^2$ stands for square modulus, FT for Fourier or Fourier-Dirac transformation, HT for Hankel transformation, AC for autocorrelation, Proj. for projection, Int. for integration and Diff. for its reverse operation. Adapted from Ref. [23]

2.2.1.3 Representation in momentum space

The important point for this work is that real-space distortions to the electron density (e.g. hybridisation, bonding/anti-bonding effects) are reflected in momentum space. Thus a measurement in momentum space is just as instructive as a measurement in real space. The relationships between different quantities in real space and momentum space are summarised in Fig. 2.4.

The quantities of interest here are $\chi_i(\mathbf{r})$, these are each of the molecular orbitals involved in the magnetism, this quantity represents the molecular orbital wavefunction in real space. A 3D Fourier transform takes this quantity into momentum space, $\chi_i(\mathbf{p})$,

$$\chi_i(\mathbf{p}) = \frac{1}{(2\pi)^{3/2}} \iiint \chi_i(\mathbf{r}) \exp(-i\mathbf{p}\cdot\mathbf{r})\ \mathrm{d}\mathbf{r}. \tag{2.9}$$

To produce an electron momentum density, we take the modulus square of $\chi_i(\mathbf{r})$

to represent $\rho_i(\mathbf{p})$,

$$\rho_i(\mathbf{p}) = |\chi_i(\mathbf{p})|^2 . \tag{2.10}$$

Projection of $\rho_i(\mathbf{p})$ along a chosen vector q results in the Compton profile $J_i(\mathbf{q})$ for the i-th molecular orbital,

$$J_i(\mathbf{q}) = \iiint \rho_i(\mathbf{p})\delta\left(\frac{\mathbf{p}\cdot\mathbf{q}}{q} - q\right)\,\mathrm{d}\mathbf{p}. \tag{2.11}$$

This method of producing theoretical Compton profiles has been demonstrated by a few authors; for examples see Refs. [9, 7, 10]. In real terms the way the real-space wavefunctions are turned into Compton profiles is as follows: the real-space wavefunction was sampled around the *ab initio.* atoms for each molecular orbital (MO) of interest. After careful testing the size of this box and the real-space increment turned out to be very important to the meaning and the shape of the Compton profile. Special care was taken to ensure the electron density was effectively zero at the edges of the box. A 99 $\times$ 99 $\times$ 99 box of 20 $\times$ 20 $\times$ 20 Å was sufficient to adequately describe the momentum density. The matrix of 3D probability was then Fourier transformed using the `fftn` routine in Matlab$^{\mathrm{TM}}$. The resultant momentum matrix was re-ordered to ensure that the 3D momentum density was symmetric about the central matrix element so that any arbitrary rotation may be performed without moving the central point. The square modulus of this matrix was then taken.

To extract a Compton profile from this matrix, rotations were performed using the Euler angles α, β and γ so that the axis required was aligned along an integration axis. The integration was then performed by summing the matrix elements perpendicular to the axis, the resultant line shape is the Compton profile for that MO.

Once each of the Compton profiles for the MO's of interest were calculated, they were normalised and interpolated onto the experimental p_z scale. Each orbital had it's own weighting coefficient $a_1, a_2, ..., a_N$, for N orbitals. The *total* Compton profile is

therefore the sum over N MO's, so that

$$J_{\text{total}}(\mathbf{q}) = \sum_{i}^{N} a_i J_i(\mathbf{q}) \tag{2.12}$$

The sum of these orbitals was compared to the experimental data using a weighted χ^2 routine. The weighted χ^2 for each crystal direction was calculated and the sum was minimised by altering the coefficients a_i. Provided the experimental data were normalised to the total spin moment these coefficients are then the spin densities in each molecular orbital, thus allowing the contributions to the spin moment to be found. Further analysis can provide details as to the metal ion and oxygen contribution to the molecular orbital and thus the spin moment.

2.2.2 Density functional theory

The important details of density functional theory (DFT) are now addressed as a way of solving the many body electron problem introduced earlier. DFT differs in its approach to solving the many-body electronic problem in §2.2 (Eq. 2.3) in it's basic assumption which states that the ground state energy is a unique functional of the electronic charge density, $\rho(\mathbf{r})$.

In 1964, Hohenberg and Kohn proposed a theorem which stated that the total energy of a system can be formulated as a functional of the charge density [24]. Soon afterwards, W. Kohn and L. J. Sham developed self-consistent eigenvalue equations similar to those of the Hartree-Fock method which could be solved exactly [25]. By accounting for electronic correlation, DFT provides an advantage over the Hartree-Fock method described in §2.2. If we consider a set on non-interacting particles, ϕ_j, then the total electronic charge density is

$$\rho(\mathbf{r}) = -e \sum_{j}^{\text{occ}} \phi_j^*(\mathbf{r}) \phi_j(\mathbf{r}). \tag{2.13}$$

The total ground state energy, $E[\rho]$, is then formulated as a functional of the

charge density given in Eq. 2.13 as the sum of the Hartree-Fock energy approximation plus an additional exchange-correlation term.

$$E[\rho] = T[\rho] + \int V_{\mathrm{ext}}(\mathbf{r})\rho(\mathbf{r})\ \mathrm{d}r + V_{\mathrm{C}}[\rho] + E_{\mathrm{XC}}[\rho], \tag{2.14}$$

where V_{ext} is the external potential on the system, $T[\rho]$ the kinetic energy and E_{XC} is the exchange-correlation energy.

DFT is an exact method except for the E_{XC} term, which is a non-local attractive electron-electron interaction which cannot be evaluated. Modeling the exchange and correlation interaction is the difficulty in DFT and approximations have to be made to the energy functional. The simplest approximation is the local density approximation (LDA) - whereby the energy is formulated according to the exact exchange of a uniform electron gas. More complex functionals may often be more appropriate, for example the generalised gradient approximation (GGA) - which takes into account not only the value of the electron density, like the LDA, but also its first derivative.

It is assumed that the electronic charge density that minimises the energy of the overall functional is the true $\rho(\mathbf{r})$. The principle that the *charge density* is the basic variable and the electron charge density is key to all properties reduces the $3N$ variable problem of N electrons with three spatial coordinates to one variable $\rho(\mathbf{r})$ problem with three spatial coordinates, this greatly simplifies the calculation.

Whilst the Kohn-Sham equations formed the fundamental formalism and basis behind DFT, it was left to others to develop schemes to solve it. The main branches used for analysis in this thesis are the Kohn-Korringa-Rostiker (KKR) approach and the full potential linearised augmented plane wave (FLAPW) approach. The reason for their usage will be described below, but for a full review of the theoretical background on both these methods consult Ref. [26] and Ref. [27] respectively.

2.2.2.1 KKR

For the calculations of ground state properties such as magnetic moments and densities of state the Munich SPR-KKR package was used [26]. This code solves the Dirac equation through the KKR Greens function formalism. The code is written with the aim of calculating spectroscopic properties of magnetic solids, and as such can be used to compare experimental techniques such as X-ray absorption spectroscopy (XAS), X-ray magnetic circular dichroism (XMCD) and importantly for this thesis the electron momentum density distributions of electrons in a crystal. The calculated profiles can be decomposed into site specific and even orbital specific distributions. This is invaluable for analysing an experimental profile as it can describe where the magnetism is coming from.

The KKR formalism lends itself well to the calculation of disordered alloys through the application of the coherent potential approximation (CPA). The calculations shown here are based on the atomic sphere approximation (ASA), whereby the charge density and potential, $V(\mathbf{r})$, are described inside a spherical volume called a "muffin-tin" but outside the muffin tin radius, R_{MT}, the potential is constant. As such any information in the intistitial region, I is lost.

$$V(r) = \begin{cases} V\left(|\mathbf{r} - \mathbf{R}|\right) & \mathbf{r} < R_{\mathrm{MT}} \\ \mathrm{Constant} & \mathbf{r} \in I \end{cases} . \tag{2.15}$$

The use of the SPR-KKR code in this thesis is in §5.2 for $Ca_3Co_2O_6$ in deconstructing the magnetic Compton profile and investigating the metallic nature, UCoGe for deconstructing the moment and producing the magnetic Compton profile §6.2 and for calculating the spherically averaged Compton profile of the disordered alloy $Fe_{0.65}Ni_{0.35}$ in §7.2.

2.2.2.2 FLAPW

For full potential (FP) calculations, the ELK code was used [27]. This is a method for calculating the electronic structure of a periodic crystal using the linear augmented plane wave method [28]. Inside the atomic muffin tins the wavefunctions are described as atomic partial waves. The energy dependence of the basis partial waves leads to a non-linear eigenvalue problem. This was computationally difficult to solve as energy bands were found by root finding. However, the equation was linearised so that the eigenvalues can be obtained with one diagonalisation.

The code is a full potential code, which lifts the restriction of the ASA; inside the muffin-tin the wavefunction is described by atomic partial waves in a given spherical potential, but outside the muffin tin the potential is fully defined as a plane wave basis set matched at the muffin tin boundaries,

$$V(r) = \begin{cases} \sum_{LM} V_{n,l}(\mathbf{r}) Y_{n,l}(\theta, \phi) & \mathbf{r} < R_a \\ \sum_{K} V_K e^{i\mathbf{K}\cdot\mathbf{r}} & \mathbf{r} \in I \end{cases} . \tag{2.16}$$

The applicability of the code to the work presented in this thesis is the inclusion of the self interaction correction, local spin density approximation + U (LSDA + U) formalism which the SPR-KKR code lacks. The LSDA + U method takes into account the interaction of an electron with, not only the crystal potential, but also its own potential. This is extremely important when dealing with localised, strongly correlated electron systems. The codes ability to deal with disordered alloys is limited to using a supercell, which is not always appropriate for lightly doped systems. An extension to the code has been written to calculate the full potential electron momentum density distributions from potentials in ELK by D. Ernsting and S. B. Dugdale at Bristol University. This code is used in this thesis for $Ca_3Co_2O_6$ in §5.2 for investigating the U dependence.

Chapter 3

The theory of Compton scattering

There are three distinct regimes in which electromagnetic radiation interacts with matter. For low energies ($\sim 10^2$ eV) the photoelectric effect is dominant. For very high energies ($\sim 10^6$ eV) particle pair production is dominant. The Compton effect is dominant in the intermediate regime ($\sim 10^3$ eV). The cross sections shown in this chapter are for the scattering of photons in the inelastic, Compton regime. They are based on the conservation of energy and momentum and initially are treated for stationary electrons.

3.1 Compton scattering

Although many important features of Compton scattering can be explained simply by the kinematics shown in Fig. 3.1, a true understanding of the technique of magnetic Compton scattering requires a consideration of the scattering cross-section.

Compton scattering is the inelastic scattering of a photon from an electron. The scattered photon loses energy to the scattering electron. Compton showed this to be dependent on the incident angle and the incident energy. These observations can be explained if the electromagnetic radiation is transferred by photons carrying momentum, $p = \frac{E}{c}$ and if the photons are scattering off individual electrons, which behave as free particles. Compton derived the energy softening (wavelength shift) in the formula which

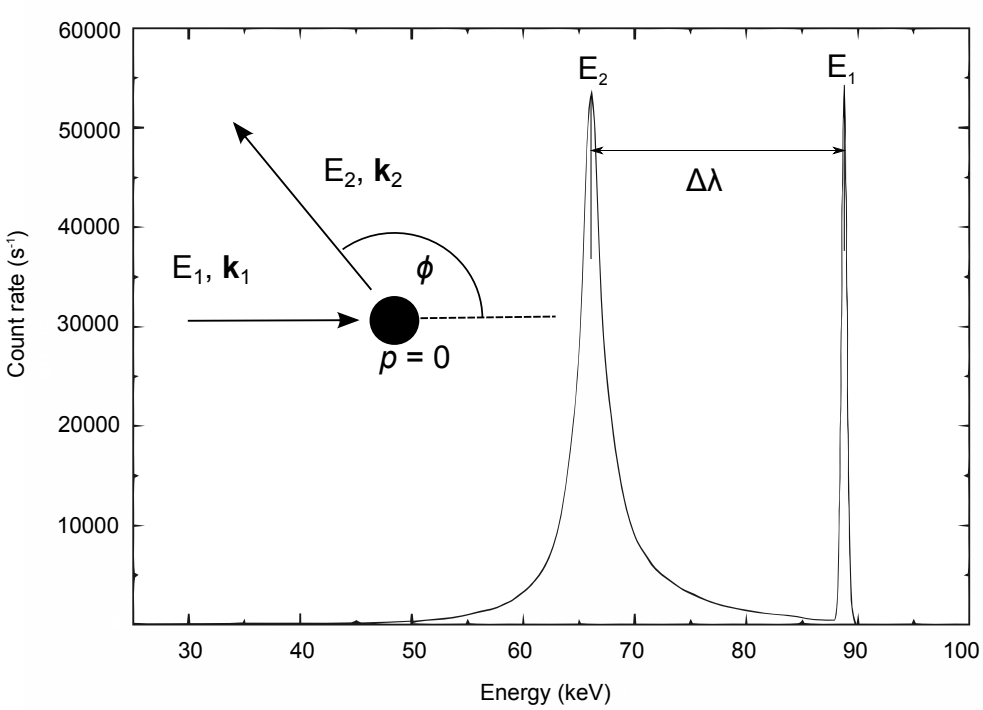

Figure 3.1: (Main) Experimental Compton scattering spectrum. (Inset) Compton scattering of a photon from a stationary electron. The terms are defined in the text.

now bears his name:

$$\Delta\lambda = \frac{hc}{E_2 - E_1} = \frac{2h}{m_e c} \sin^2 \frac{\phi}{2}, \tag{3.1}$$

where $\Delta\lambda$ is the change in wavelength E_1 and E_2 are photon energies before and after the collision respectively and ϕ is the angle of scattering and have meanings depicted in Fig. 3.1 (Inset). Eq. 3.1 is written in terms of the initial and final energies, E_1 and E_2,

$$E_2 = \frac{E_1}{1 + (E_1/m_e c^2)(1 - \cos\phi)}. \tag{3.2}$$

Where m_e is the electron rest mass. Eq. 3.2 is the case for a stationary electron; the resulting spectrum for the scattered photons would be a sharp peak of back-scattered photons at E_2 given by the Compton equation, Eq. 3.2. The terms are shown in a typical energy spectrum of high energy X-rays in Fig. 3.1. Aside from being a ratification for

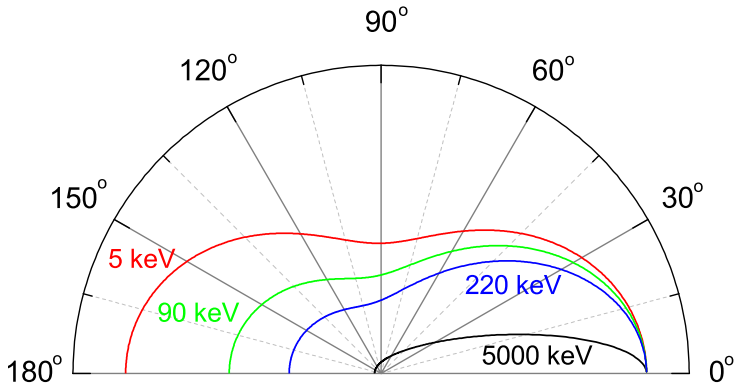

Figure 3.2: Angular variation of the Klein-Nishina scattering cross-section for four selected incident beam energies: low (5 keV), high (5000 keV) and two energies used for studies in this thesis (90 keV and 220 keV). Forward energy is defined as 0°

the then new quantum theory of light, the Compton scattering technique shows how X-ray interact with matter at high energies.

3.1.1 The Klein-Nishina cross-section

In 1929, Klein and Nishina performed a quantum electrodynamical calculation of the Compton scattering cross-section [29]. It was shown that the cross-section for scattering of an unpolarised photon is given by

$$\left(\frac{\mathrm{d}\sigma}{\mathrm{d}\Omega}\right)_{\mathrm{KN}} = \frac{1}{2}\left(\frac{e^2}{m_e c^2}\right)^2 \left(\frac{E_2}{E_1}\right)^2 \left(\frac{E_1}{E_2} + \frac{E_2}{E_1} - \sin^2\phi\right), \tag{3.3}$$

where e, m_e and c is the charge on an electron, electron rest mass and the speed of light respectively. The solutions of the Klein Nishina cross-section for four energies are shown in Fig. 3.2. $E_1 = 90$ and 220 keV are included as these are the energies used for work in this thesis. Fig. 3.2 shows that forward scattering (scattering in the 0° direction) is increasingly favoured as the energy of the incident photon is increased. For low energies photons, the Klein-Nishina cross-section reduces to the classical Thomson cross-section, which is symmetric for forward and back-scattering geometries. The Klein-Nishina cross-section describes the nature of the scattering process of a high energy X-ray with an

electron, but is devoid of any information about the target electron.

3.1.2 Compton scattering and electron momentum density

Compton scattering was used in the early part of the twentieth century as a ratification of the quantum theory of light. However, even the earliest experiments showed that the Compton peak was broader than expected. Compton associated this with the experimental resolution. It was quickly suggested by J. W. M. DuMond [30] that this broadening was not resolution based, but instead a result of the motion of the electrons involved in the scattering. The line broadening is because the scattered photon is Doppler broadened along the direction of momentum transfer. DuMond went on to show that the energy spectrum of scattered photons is directly related to the momentum distribution of the electrons in the scatterer.

From DuMond's reasoning, it was shown that the secondary photon energy was not only dependent on the primary energy and scattering angle, but also on the component of the initial electron momentum, parallel to the scattering vector. Referring to Fig. 3.1 initial and final energies can be equated,

$$E_2 - E_1 = \frac{1}{2m_e}[\mathbf{p} + \hbar(\mathbf{k}_1 - \mathbf{k}_2)]^2 - \frac{|\mathbf{p}|^2}{2m_e} = \frac{\hbar^2 \mathbf{q}^2}{2m_e} + \frac{\hbar \mathbf{q} \cdot \mathbf{p}}{m_e}, \tag{3.4}$$

where $\mathbf{k}_1$ and $\mathbf{k}_2$ are wavevectors for the incident and scattering photons respectively and $\mathbf{q} = \mathbf{k}_1 - \mathbf{k}_2$ is the scattering vector. By inspection of Eq. 3.4, there exists not only the fixed Compton shift, but a term which is linearly dependent on one component, p_z, of the momentum of the electron. For target electrons where the momentum density distribution is given by $\rho(\mathbf{p})$, the component of the momentum parallel to the scattering vector, p_z is the so called *Compton profile*

$$J(p_z) = \iint \rho(p_x, p_y, p_z)\ \mathrm{d}p_x \mathrm{d}p_y. \tag{3.5}$$

It can be seen as a measurement of the probability density of *all* the electronic

wavefunctions in a sample, albeit in the rather unfamiliar domain of momentum space. As such a Compton scattering experiment can be highly instructive in the identification of states in a target.

A description of how electronic states are related to the electron momentum distribution (EMD) is described below. Through the Bloch theorem, $\Psi_{j,k}(\mathbf{r})$ may be written as a product of a real-space wavefunction and a Bloch function describing the periodicity of the crystal lattice,

$$\Psi_{j,\mathbf{k}}(\mathbf{r}) = \frac{1}{\sqrt{V}} u_{j,\mathbf{k}}(\mathbf{r}) \exp(i\mathbf{k}\cdot\mathbf{r}), \tag{3.6}$$

because the Bloch function possesses the periodicity of the reciprocal lattice, it can therefore be can expanded in terms of the reciprocal lattice vector **G** so that

$$\Psi_{j,\mathbf{k}}(\mathbf{r}) = \frac{1}{\sqrt{V}} \sum_{G} a_{j,\mathbf{k}}(\mathbf{G}) \exp(i\mathbf{G}\cdot\mathbf{r}) \exp(i\mathbf{k}\cdot\mathbf{r}). \tag{3.7}$$

Because of the reciprocal relationship between real space and momentum space and in the independent particle approximation, the spin independent momentum density of Bloch electrons is then the square modulus of the Fourier transformed wavefunction, so that

$$\begin{aligned} \rho(\mathbf{p}) &= 2 \sum_{j,\mathrm{occ}} \left| \int_V \Psi_{j,\mathbf{k}}(\mathbf{r}) \exp(-i\mathbf{p}\cdot\mathbf{r}) \, \mathbf{d}r \right|^2 \\ &= 2 \sum_{j,\mathbf{k},\mathbf{G}} \theta(E_f - E_{k,j}) \left| a_{j,\mathbf{k}}(\mathbf{G}) \right|^2 \delta(\mathbf{p} - \mathbf{k} - \mathbf{G}) \end{aligned} \tag{3.8}$$

where $\theta(E_f - E_{k,j})$ is a step function expressing the sum over all occupied states, i.e. it is one for $E_{\mathbf{k},j} \leq E_f$ and zero otherwise. Contributions for higher-momentum components, that is those with wavevector greater than the first Brillouin zone, are expressed by delta functions. The intensities of these components are determined by

the Fourier components $a_{j,\mathbf{k}}(\mathbf{G})$ of the real-space wavefunctions. Eq. 3.8 demonstrates that the EMD is composed of plane wave contributions at not only $\mathbf{p} = \mathbf{k}$, but also at $\mathbf{p} = \mathbf{k} + \mathbf{G}$. This highlights the difference between reciprocal space, k, and momentum space p, where contributions above the first $\mathbf{G}$ are called higher momentum components.

For a more rigorous derivation, one involving spin and for relativistic energies approaching mc^2, quantum electrodynamics must be used which treats electron momentum and spin on an equal footing and is the subject of the next section.

3.1.3 Charge Compton scattering cross-section

How is the Compton integral in Eq. 3.5 determined in a scattering experiment? In a Compton scattering experiment the quantity measured is the double differential scattering cross-section (DDSCS); this is the flux scattered into a certain solid angle, Ω, with a certain energy, E_2. Following the logic of Ref. [31] the DDSCS is written as the product of a term describing the nature of the scattering, for which the Klein-Nishina cross-section for high X-ray energies may be used, $(\mathrm{d}\sigma/\mathrm{d}\Omega)_{\mathrm{KN}}$, and a term describing the nature of the target, the charge response function $S(\mathbf{q}, E)$,

$$\frac{\mathrm{d}^2\sigma}{\mathrm{d}\Omega \mathrm{d}E} = \left(\frac{\mathrm{d}\sigma}{\mathrm{d}\Omega}\right)_{\mathrm{KN}} S(\mathbf{q}, E). \tag{3.9}$$

The charge response function is determined through the Born approximation, which is valid in cases where the energy of the interaction is much smaller than the energy of the scattering photon [32]. The scattering process can then be described as a transition between initial and final momentum states given by Fermi's Golden Rule. Assuming the perturbation of an electromagnetic wave acting on an electron within the Born approximation, the result for the charge response function is given as,

$$S(\mathbf{q}, E) = \sum_f \left| \left\langle f \left| \sum_j \exp\left(i\mathbf{q} \cdot \mathbf{r}_j\right) \right| i \right\rangle \right|^2 \delta(E_2 - E_1 - \omega_2). \tag{3.10}$$

where the δ-function restricts the summation to those states accessible with energy

conservation. The exponential gives the phase of the j-th electron, and the sum is carried out over all j electrons.

The Compton profile from the double differential scattering cross-section can now be obtained with one further approximation: *the impulse approximation*. This is the assumption that the scattering occurs impulsively. In other words, the potential seen by the target electron is the same immediately before and after the interaction. This is the case for high energies where the incident X-ray is much larger than the binding energy of the electrons. Under this approximation the charge response function reduces to an integral over the ground state momentum,

$$S(\mathbf{q}, E) = \int \rho(\mathbf{p}) \delta \left(\omega - \frac{k^2}{2m_e} - \frac{k}{m_e} p_z \right) \, \mathrm{d}\mathbf{p}, \tag{3.11}$$

leading to our DDSCS being of the form,

$$\frac{\mathrm{d}^2\sigma}{\mathrm{d}\Omega \mathrm{d}E_2} = \left(\frac{\mathrm{d}\sigma}{\mathrm{d}\Omega} \right)_{\mathrm{KN}} \frac{E_2}{E_1} \frac{m_e}{|\mathbf{q}\,|} \iint \rho(\mathbf{p}) \, \mathrm{d}p_x \mathrm{d}p_y. \tag{3.12}$$

In this way the measured energy spectrum is sensitive to the ground state momentum density measured along the scattering vector. This cross-section is derived for an unpolarised photon interacting with an electron, neglecting spin. In the next section, consideration is given to the cross-section once spin effects are included.

3.2 Magnetic Compton scattering

The technique of magnetic Compton scattering differs from charge Compton scattering described above in its ability to separate the momentum distributions of electrons with unpaired spins, i.e. the magnetic electrons. This is possible due to a spin dependent interference term in the scattering cross-section. With high energies, the scattering becomes magnetic and sensitive to the electron spin vector and the degree of photon circular polarisation.

3.2.1 The spin dependent Compton scattering cross-section

The next stage in the derivation of the Compton cross-section investigated the dependence of the cross-section on the spin of the electron, and whether there was any magnetic contribution.

In 1970, Platzman and Tzoar derived scattering factors in the cross-section for a moving electron including spin [33]. The resulting cross-section contains three terms. There is a term which leads to the Klein-Nishina charge cross-section described in §3.1.1. The two remaining terms have spin dependencies $iA(\mathbf{B}\cdot\mathbf{S})$ and B^2S^2. The second term is what is measured in magnetic diffraction, however, in inelastic scattering, this B^2S^2 term is not measured, this is because $B \sim \left(\omega_1/mc^2\right) A$ and thus generally ignored [34]. Therefore, the second term must be used, the "interference" term between the charge and magnetic scattering, the size of which scales with the energy transfer.

The first challenge is engineering this interference term to be a real measurable quantity. A complex component to the incoming X-ray beam can be obtained by using a beam which has a degree of ellipticity, thus resulting in a real value for the $iA(\mathbf{B}\cdot\mathbf{S})$ term. It is the DDSCS quantity that is measured in a magnetic Compton scattering experiment. So like Eq. 3.12, but including the magnetic scattering term, our DDSCS becomes composed of two scattering functions,

$$\frac{\mathrm{d}^2\sigma}{\mathrm{d}\Omega \mathrm{d}E_2} = \frac{m_e}{2|\mathbf{q}|}\frac{E_1}{E_2}\left[\left(\frac{\mathrm{d}\sigma}{\mathrm{d}\Omega}\right)_{\mathrm{charge}} J(p_z) + \left(\frac{\mathrm{d}\sigma}{\mathrm{d}\Omega}\right)_{\mathrm{mag}} J_{\mathrm{mag}}(p_z)\right], \tag{3.13}$$

where the cross sections, $(\mathrm{d}\sigma/\mathrm{d}\Omega)_{\mathrm{charge}}$ and $(\mathrm{d}\sigma/\mathrm{d}\Omega)_{\mathrm{mag}}$ are the Klein-Nishina cross sections for a polarised photon scattering from a stationary electron [35],

$$\begin{aligned}
\left(\frac{\mathrm{d}\sigma}{\mathrm{d}\Omega}\right)_{\mathrm{charge}} &= \frac{r_e^2}{2}\left(\frac{E_2}{E_1}\right)^2\left[1+\cos^2\phi + P_L\sin^2\phi + \frac{\mathbf{q}}{mc}(1-\cos\phi)\right], \\
\left(\frac{\mathrm{d}\sigma}{\mathrm{d}\Omega}\right)_{\mathrm{mag}} &= \frac{r_e^2}{2}\left(\frac{E_2}{E_1}\right)^2\left[(\cos\phi - 1)P_C\hat{S}\cdot\frac{(\mathbf{k}_1\cos\phi - \mathbf{k}_2)}{m_e c}\right],
\end{aligned} \tag{3.14}$$

P_L and P_C are the Stoke parameters for linear and circular polarisation respectively and $\hat{S}$ is the unit spin vector. Shown in Fig. 3.3 is the ratio of the spin to the charge scattering cross-sections, the figure shows that not only does the spin scattering scale with the incident energy, but it also greatly favours back scattering geometries.

Once coupled to the spin vector, a method is needed for isolating $J_{\mathrm{mag}}(p_z)$. With reference to Eq. 3.13 if the sign of the spin dependent term can be reversed then the $J_{\mathrm{mag}}(p_z)$ term can be obtained. This reversal can be achieved either by flipping the photon polarisation (through P_C) or by reversing the magnetisation of the sample ($\hat{S}$) with an external field. The second technique is preferable as to change photon polarisation at the European Synchrotron Radiation Facility (ESRF) requires moving the entire set-up above and below the synchrotron beam orbit making data normalisation difficult. The resulting measurement is a projection of the momentum density of only those electrons with unpaired spins.

As with the charge scattering explained above, one can define the projection of spin-polarised electron momentum onto the scattering vector as the *magnetic Compton profile* (MCP) (sometimes called the spin-polarised Compton profile). The magnetic Compton profile (MCP) can be defined as,

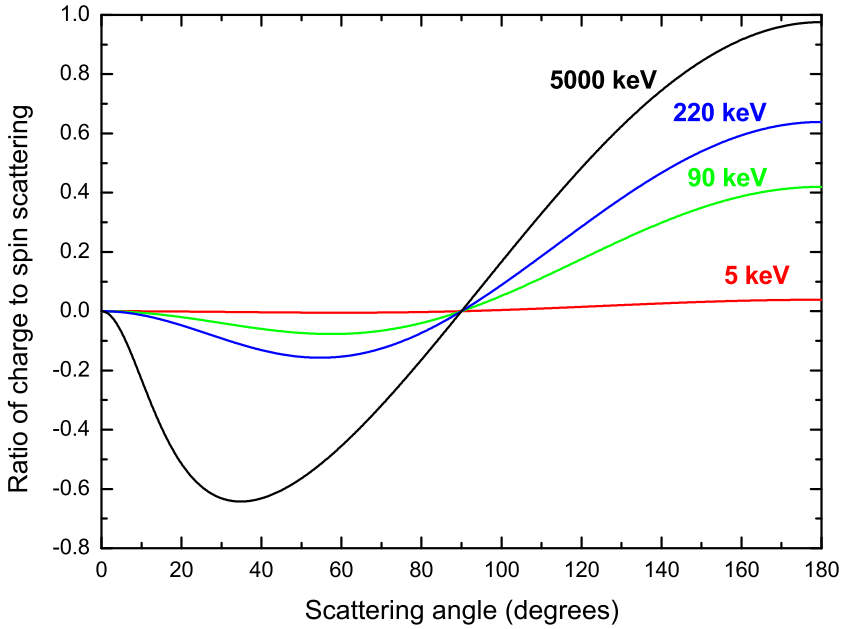

Figure 3.3: Ratio of magnetic to charge scattering as a function of scattering angle and incident energy. Adapted from Ref. [36]. Note that the spin scattering is zero at perpendicular scattering geometries.

$$J_{\mathrm{mag}}(p_z) = \iint \left[\rho^{\uparrow}(\mathbf{p}) - \rho^{\downarrow}(\mathbf{p})\right] \, \mathrm{d}p_x \mathrm{d}p_y, \tag{3.15}$$

$$\mu_{\mathrm{spin}} = \int J_{\mathrm{mag}}(p_z) \, \mathrm{d}p_z. \tag{3.16}$$

Here $\rho^{\uparrow}(\mathbf{p})$ and $\rho^{\downarrow}(\mathbf{p})$ are the momentum-dependent majority and minority spin densities, respectively. The area under the MCP (Eq. 3.16) is equal to the number of unpaired electrons, i.e. the total spin moment per formula unit in Bohr magnetons. This is the main result of performing a magnetic Compton scattering experiment; it provides an accurate, unambiguous measure of the spin moment of a sample without any need for further modeling.

The existence of a magnetic Compton profile using circularly polarised light was

experimentally ratified by Sakai and Ôno [37] who used a millikelvin cooled, oriented β-emmiting source to provide a low flux, circularly polarised γ-ray source. The first synchrotron based magnetic Compton scattering experiment was performed by Cooper *et al.* [38]. This experiment highlighted the anisotropy of magnetic electron momentum distribution in iron. Since the 1990s, magnetic Compton scattering has been performed regularly at synchrotron facilities as a measure of spin-polarised electron momentum densities, for various examples see Chapter 10 of Ref. [31].

3.2.2 Identification of magnetic species

Identification of the constituent magnetic contributions is made possible in magnetic Compton scattering because of the different characteristic line shapes of various electronic states. Tightly bound core electrons with greater momenta produce a greater Doppler shift resulting in a broader profile. The delocalised, slower moving valence

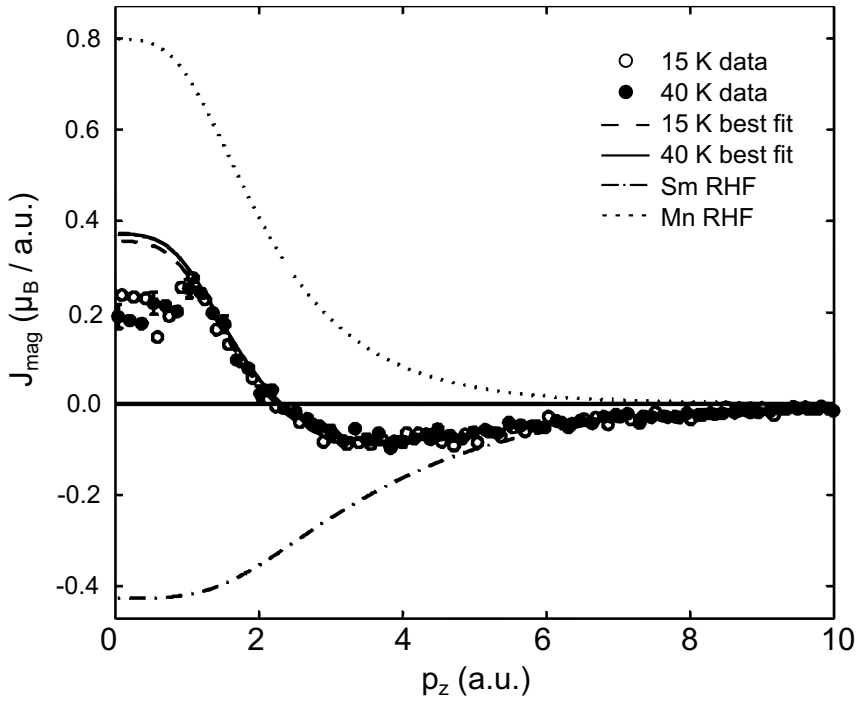

Figure 3.4: The experimental magnetic Compton profile of $SmMn_2Ge_2$. Using RHF predictions for the Mn $3d$ and Sm $4f$ moment. Adapted from [39].

electrons produce narrower Compton profiles. This is demonstrated in Fig. 3.4, where the experimental MCP for $SmMn_2Ge_2$ is deconstructed using RHF profiles of Mn 3*d* and Sm 4*f*, as to extract a spin moment for each magnetic species in the sample. The discrepancy at low momentum is expected in the free-atom approximation. Vast improvements are obtainable when modeling is performed beyond the free atom limit with molecular orbital theory or density functional theory, as is the subject of §2.2.

3.2.3 Sensitivity to the orbital moment

Eq. 3.14 shows that the cross-section defines a contribution from the spin angular momentum component, $\hat{S}$. But it is known from §2.1.1 that magnetism arises from not just the intrinsic $\hat{S}$, but also the motion of the electron cloud as defined by its orbital angular momentum $\hat{L}$. The contribution the orbital moment makes to magnetic Compton scattering is based on the impulse approximation on which the relativistic cross-section is founded. The impulse approximation states that the interaction time between the photon and the electron is negligibly short. The motion of an electron is not defined instantaneously, so it is assumed that the orbital moment does not contribute to the scattering.

This insensitivity to the orbital moment has been experimentally ratified by Cooper *et al.* in which a magnetic Compton scattering study of $HoFe_2$ was undertaken [40]. $HoFe_2$'s magnetisation is mainly derived from its orbital motion. In one geometry where the scattering vector is perpendicular to the magnetic field, the magnetic Compton scattering signal is proportional to $\left\{\hat{S}\epsilon + \hat{L}(1+\epsilon)\right\}$ [1]. The measurement should be only sensitive to the orbital contribution. It was shown that no magnetic Compton profile was observed. However, a more common geometry with the magnetic field parallel to the scattering vector sensitive to $\left\{\hat{S}(2+\epsilon+\hat{L})\right\}$ showed a large magnetic Compton profile. This is evidence that the magnetic Compton profile is sensitive solely to the spin contribution of the moment.

[1] $\epsilon = (E_1 - E_2)/E_1 \sim 0.1$.

Chapter 4

Experimental method

4.1 Introduction

This chapter outlines the various experimental techniques used in the gathering of data for this thesis. It begins with a discussion of the way X-rays are generated at third generation synchrotrons (where all X-ray data in this thesis are taken) and describes the ways of tuning these X-rays to meet the conditions required for a magnetic Compton scattering experiment. The components used in a magnetic Compton scattering experiment are then introduced.

Once data has been taken, a good understanding of the corrections which need to be made to the raw energy spectrum in vital. Proper treatment of the corrections needed is vital for the interpretation of the shape of the profile and the size of the spin moment.

The chapter continues with notes on complementary techniques, in particular techniques that yield similar information to magnetic Compton scattering (MCS), highlighting their advantages and disadvantages. The chapter concludes with details of characterisation methods used in this thesis, bulk magnetisation methods and X-ray alignment. Special mention is given to a new sample holder designed and created for this thesis that can guarantee an alignment precision of better than 0.5°.

4.2 Magnetic Compton scattering at an X-ray synchrotron facility

Magnetic Compton scattering has only become a viable technique in the study of magnetisation densities since the advent of third generation synchrotron radiation facilities. The properties necessary i.e. high energies, tunable polarisation and high brilliance are all accessible at synchrotron radiation facilities.

4.2.1 Synchrotron radiation

Synchrotron radiation is generated when a charged particle accelerates. In a synchrotron radiation facility, electrons are generated by an electron source and accelerated in the first instance by a Linac (linear accelerator). These electrons are then injected into a booster ring where they reach relativistic speeds just shy of the speed of light and with energies typically between 3 - 8 GeV. These electrons are then injected into the storage ring. The orbit of the electron beam is maintained in the ring by bending magnets that apply a magnetic field to the electron beam. The electron beam is "steered" into further insertion devices/optics around the storage ring so that they can be tuned to the beam parameters needed by the experimental user.

4.2.2 Insertion devices

As most of the data presented in this thesis come from ID15A beamline at the ESRF, the setup relevant to that beamline will be discussed. ID15A obtains high energy photons from an asymmetric multipole wiggler (AMPW). A mulitipole wiggler is a device that sits in the stream of the electron beam, an array of magnets are positioned above and below, altering the beam course. The "wiggling" of the electron beam by the wiggler results in a cone of X-rays being emitted in the forward direction. The magnetic field profile of a conventional wiggler is shown in the red line of Fig. 4.1. For a full description of the physics of wigglers and undulators consult Refs. [41, 42].

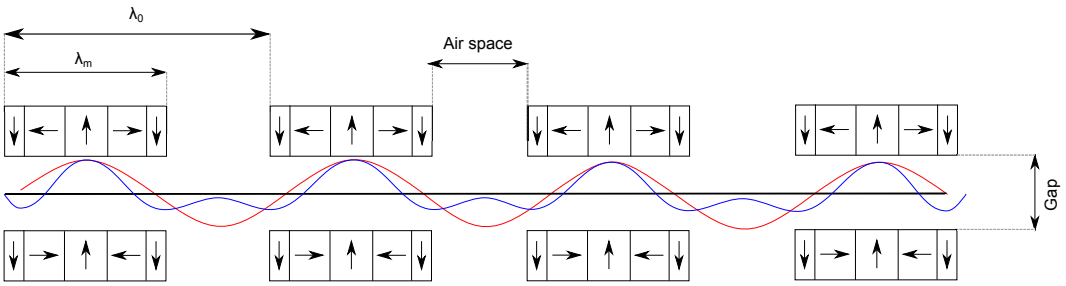

Figure 4.1: Magnetic pole and magnetic field profile of a conventional multipole wiggler (red) compared with an *asymmetric* multipole wiggler (blue). The two profiles are obtained by using different arrangements of magnets in the wiggler, adapted from Ref. [31].

Integral to the technique of magnetic Compton scattering is the production of light with a degree of circular polarisation. In a conventional wiggler right-handed and left-handed light cancel, thus resulting in no net circular polarisation. To overcome this cancellation problem one can use an *asymmetric* multipole wiggler. An asymmetric wiggler no longer has a symmetric magnetic field profile in the longitudinal direction, rather, it has a large positive field over a short distance followed by a smaller negative field over a longer distance designed as to have a net zero integrated field per period (see Fig. 4.1). In this case, the circular polarisation contributions of the two poles are not equal and so although there still exists a cancellation, there is a resultant net circular polarisation off-axis.

The increase of circular light as one moves off-orbit is opposed by a Gaussian-like fall off of the photon flux. A figure of merit is therefore used to obtain maximum flux and still obtain a decent degree of circular polarisation to maximise the magnetic signal. The off-axis or "inclined-view" method is used for all magnetic Compton scattering experiments on ID15A at ESRF. Hard circular polarised light can also be obtained from an eliptical wiggler as installed on BL08w, SPring-8. In an elliptical wiggler a periodic displacement of the field is introduced above and below the electron beam, forcing the beam to travel in an eliptical path, see Ref. [31].

At the ESRF, the beam from the bending magnet passes into a 7 pole 1.84 T AMPW ((a) in Fig. 4.2). The critical energy of AMPW is 44 keV and the useful

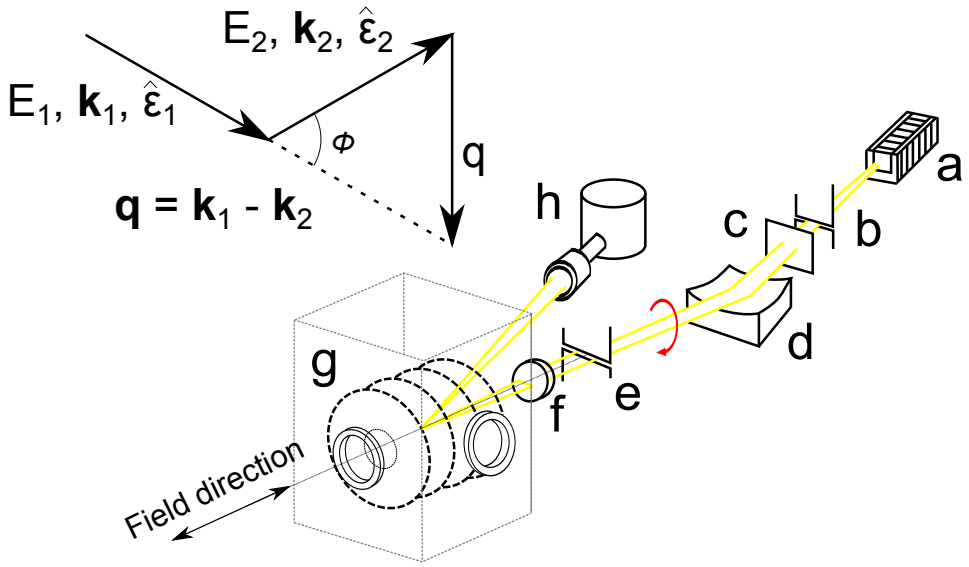

Figure 4.2: Setup of a magnetic Compton scattering experiment. The purpose of each component is described in the text. (a) the AMPW insertion device. (b) Primary slits. (c) SiC absorber. (d) Monochromator. (e) Secondary slits. (f) Monitoring diode. (g) 9 T magnet. (h) 13-element solid state Ge detector. Adapted from Ref. [43].

spectrum extends up to 500 keV. At the ESRF, an X-ray beam a few milliradian above or below orbit is typically selected with the primary slits ((b) in Fig. 4.2). The circular beam then enters the optics hutch for further tuning.

4.2.3 X-ray optics

Most of the low energy X-rays are removed by a rotating water-cooled SiC disc ((c) in Fig. 4.2). The high energy beam is monochromated by the (311) reflection of a Ge crystal monochromator ((d) in Fig. 4.2) which provides an incident energy of 220 keV. Since the flux at these high energies is relatively low, and the Bragg reflection is very selective, the monochromator is slightly bent as to 'smear' the energy range of the Bragg reflected beam. The effect of this is to broaden the momentum resolution, but as will be discussed later, this is not the main source affecting resolution. The monochromated, off-orbit beam is cut down to a shape and size appropriate for the sample, and resulting in a count rate that is reasonable ($\sim$ 6000 cps under the Compton peak) by secondary

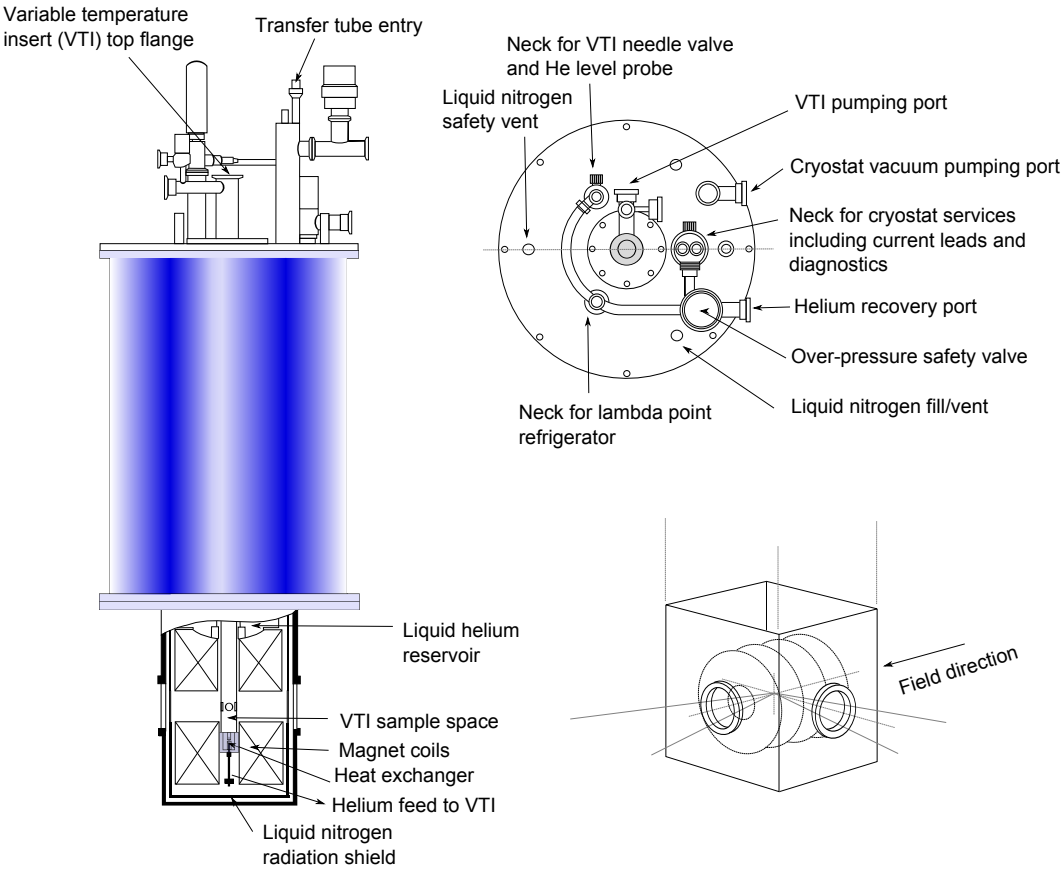

Figure 4.3: Schematic diagrams of the Spectromag cryomagnet used for magnetic Compton measurements on ID15 A

slits ((e) in Fig. 4.2). This beam is then taken into the experimental hutch.

4.2.4 9 T superconducting magnet

The sample used for Compton scattering is located between the poles of a superconducting split-pair magnet (Fig. 4.3, (g) in Fig. 4.2) with a maximum possible field $\pm$ 9 T. The sample is baffled to a variable temperature insert (VTI) where its temperature can be varied from 1.3 - 300 K (700 K with custom made furnace insert, see §7.3). The magnetic field is aligned along the scattering vector and the appropriate direction for the sample is orientated.

As the X-rays used are very high energy, the samples need not be open to the storage ring and thus can travel in air (as the attenuation of air is negligible for high

energy photons). X-ray access to the sample is through 85 μm thin aluminum windows.

4.2.5 Detectors

The multi-element detector available at the ESRF is comprised of thirteen, liquid nitrogen cooled hyperpure Ge crystals which are held at a bias of 3000 V. The large voltage bias means that the integral of the current pulse is proportional to the energy of the incident photon. A pre-amplifier integrates the current and converts it into a voltage pulse. Events are then converted as shaped pulses and logged in a multi-channel analyser. The multi-channel analyser sorts the pulses according to their heights and assigns them a channel number. The channel number is linear with the incident photon energy. This linearity however breaks down at very high photon energies and very high photon flux, therefore a reasonable photon flux should be used ($\sim$ 6000 cps in the Compton peak). Channel number to energy calibration is achieved by peak matching known fluorescence lines in a spectrum with well defined energies[1]. The count rate must be optimised to ensure that the number of counts is large enough to obtain good statistical accuracy but not so large that the time the detector is rejecting pulses; its "dead-time" is minimised. Dead-time is where the detector is blocked from measuring the next signal whilst the previous one is being registered. If the dead-time is large, in the extreme case the effective count rate may actually go down as the incident beam flux increases.

4.2.6 Experimental procedure

To measure a magnetic Compton spectrum, the beamline is set up as in Fig. 4.2. A Compton spectrum is taken in an applied field of positive polarity (A) then again in negative polarity (B) repeated in the sequence ABBA...., this sequence makes for better data normalisation and less field flipping time. The maximum field sweep rate for the 9 T Spectromag is 1 Tmin^{-1}, so minimising flipping time is essential (+ 9 T to - 9 T takes 18 minutes, during which the detector is not counting). Also, to minimise

[1] http://xdb.lbl.gov/

field flipping time, the minimum field needed is used. The other alternative is to flip the helicity of the incoming beam, as the off-axis method for circular polarisation production is being used that would require the entire setup to be moved to the other side of the synchrotron beam orbit. This was trialled in Ref. [44], however, reproducibility issues made the method unreliable.

Normalisation data (beam current) is logged every minute, this is very important as the beam at the ESRF decays due to electron-electron scattering in the storage ring. Normalisation data is acquired from an X-ray diode in the beam before the sample ((f) in Fig. 4.2).

There is a careful balance of considerations to make in the precise setup and geometry of a magnetic Compton scattering measurement. Because Compton scattering occurs at all angles (previously shown in Fig. 3.2) experimental Compton scattering can be performed in a variety of geometries. There must be careful consideration in choosing the geometry. At low energies, the scattering cross-section is almost symmetric for forward and backward scattering at low energies (10 keV) but for higher energies, forward scattering is favoured and thus provides a higher scattered count rate. However, considering a photon scattering at near transmission geometry the deflection is therefore small thus the momentum transfer is also small. This small momentum transfer affects the momentum resolution. There is another advantage to back scattering geometries, previously shown in Fig. 3.3, and that is that the spin scattering is a greater fraction of the total scattering fraction at higher angles. As such, all results in this thesis are from back-scattering experiments.

A figure of merit is also used for how much one should go off orbit to achieve the circular light. The intensity of the beam falls off following a Gaussian distribution as one moves off orbit, whilst the polarisation increases with the square root of the distance off orbit. A careful balance of all these factors is needed to optimise the experiment. Generally, back-scattering ($\sim$ 170 $^{\circ}$) at higher energies (90 - 220 keV) are used.

4.2.7 Cross section correction

The cross-section correction is how the measured energy spectrum is turned into a momentum scale, the cross-section used is that of Bell *et al.*. For the derivation, consult the original article, Ref. [45]. The important relation is that the momentum component parallel to the scattering vector is calculated from the energy spectrum with reference to the scattering cross-section

$$p_z = \left[\frac{\sqrt{E_2^2 - E_1^2 - 2E_1E_2\cos\phi}}{2} + \sqrt{1 + \frac{2m_ec^2}{E_1E_2\left(1-\cos\phi\right)}} \right] \cdot \frac{1}{\alpha m_e c^2}, \tag{4.1}$$

where α is the fine structure constant. From this it can be seen that the experimental parameters needed are the incident energy, E_1 and the scattering angle, ϕ. Derivation of the scattering angle is critical for determining the momentum scale. Each detector may have slightly different scattering angles and must be determined separately. If it is assumed the peak of the Compton profile is where there is zero momentum transfered along the scattering vector then to get the scattering angle the Compton equation is used (Eq. 3.2).

4.2.8 Experimental resolution

The resolution of the momentum density profile is given by

$$\Delta p_z = \sqrt{\left(\frac{\delta p_z}{\delta E_1}\Delta E_1\right)^2 + \left(\frac{\delta p_z}{\delta E_2}\Delta E_2\right)^2 + \left(\frac{\delta p_z}{\delta \phi}\Delta \phi\right)^2}. \tag{4.2}$$

The first term is a result of the source resolution (also encompassing the monochromator resolution mentioned earlier in §4.2.3) the second by the detector resolution and the third by geometrical factors (i.e. the scattering angle). The dominant factor affecting resolution is the detector resolution. Solid state Ge detectors suffer from poor energy resolution when compared with area charge coupled device (CCD) devices used

for high resolution charge Compton experiments which usually have a resolution of $\sim$ 0.14 a.u.. CCD devices, however, cannot measure photons quick enough to accumulate the large number of counts needed for the small signal in magnetic Compton scattering. With realistic experimental parameters, a total resolution of about 0.4 a.u. is usual.

4.3 Processing of experimental data

The process of collecting high quality, meaningful Compton data relies on the proper treatment of all aspects of the experiment. Any of the corrections below can have the effect of changing the symmetry of the profile and also the value of the flipping ratio.

4.3.1 Incident flux correction

For a magnetic Compton profile to be measured, photons must be counted for both field directions. The integrated number of counts in the detector must be normalised to the incoming photon flux or a comparison of the backscattered energy spectrum is meaningless. To do this a monitor diode is placed in the beam path after the optics hutch. The diode attenuates the beam slightly, but is an ideal and reliable measure of the photon count incident on the sample. As the beam at the ESRF decays due to electron-electron collisions and no "top-up" is used, the normalisation to the beam current is critical. Scans during sudden changes in the intensity are avoided as these are almost impossible to normalise out, so every 12 hours when the beam is "refilled" data are not taken.

A new way of normalising the data by correcting for the beam decay was trialled for a few experiments on ID15A. A perspex wedge was placed in front of the beam on a motorised stage. The motor was run in a loop where it compared the value of a diode placed in the beam path. If the current measured on the diode was too low when compared to a target value, then the wedge moved so that less perspex was in the beam and thus attenuated less. If the measured current was too high, then the wedge acted to attenuate the beam with more perspex. Despite some initial promise, problems with the motor losing steps over extended periods of time meant that the wedge correction was not usable for most experiments.

It should be mentioned here that although incident flux corrections can be made for the *number* of photons, it cannot be made for the *polarisation* of the beam. As

described before, the circular polarisation is obtained via the inclined view method, where a position a few milliradians off-orbit is taken. Any instability in this beam position not only affects the beam current but also the beam polarisation. An attempt however was made to monitor the polarisation of the beam by conducting a simultaneous magnetic Compton scattering experiment on a polycrystal of iron using the unscattered primary beam with a set up at the back of the hutch. The iron was placed in a 1 T electromagnet whose polarity could be changed in seconds. This meant that the flipping ratio of iron (which is well known) could be monitored each minute. Work is ongoing in this area.

4.3.2 Absorption correction

Absorption in X-ray scattering experiments can be a major correction. For low energy X-rays, attenuation by the air means that the experiments must be performed under UHV conditions. Luckily, for incident energies upwards of 100 keV the absorption from the air is negligible. However, other parts of the experiment may need to be corrected for.

The monochromatic beam enters the magnet bore tubes through a very thin (85 μm) aluminium window. Once the beam is scattered, the energy dispersed flux exits through the same aluminium window. However, the aluminium absorbs different parts of the spectrum differently. This can be modeled by dividing the raw spectrum by the energy dependent transmission function for aluminum

$$I = I_0 \exp(-\mu l), \tag{4.3}$$

where μ is the energy dependent mass absorption coefficient, I_0 is the original intensity and l is the thickness of the material acting as the absorber. The absorption from the hyperpure germanium detector crystals must also be included. For some experiments the addition of a tin filter was necessary. For example, $4f$ electron systems have a K-absorption line near the edge of the profile. This is the binding energy of the $1s$ electron,

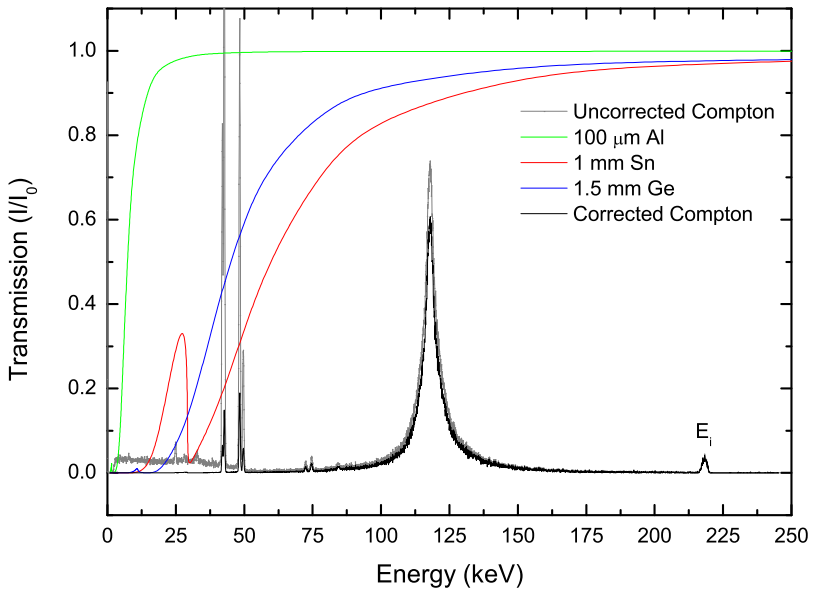

Figure 4.4: Experimental energy spectrum with absorption corrections made for Ge, Sn and Al.

with high energy X-rays this electron is ejected from the core, this process is quickly followed by a decay into this empty state by an outer electron leading to characteristic lines of emission in the spectrum. This absorption is very strong compared with the Compton profile as can be seen in Fig. 4.4. As the detector is count rate limited, it is imperative to have as many of the counts in the Compton peak. Tin has the useful property of attenuating strongly X-rays with the energy corresponding to a core state transition yet allowing transmission of the Compton energy range thus acting as an appropriate filter for our profile.

4.3.3 Multiple scattering correction

The derivation of the relativistic cross-section is based upon a *single* scattering event. In reality, however, photons can scatter twice and even three times before being registered, this is called multiple scattering. Multiple scattering can have a large effect

in Compton scattering experiments with double scattering events skewing the energy profile. Felsteiner *et al.* [46] developed a code based on a Monte-Carlo routine that simulates scattering events in a crystal given some conditions, X-ray geometry, sample density etc. The profile is then corrected for these "parasitic" scattering events.

4.3.4 Detector efficiency correction

The absorption in the detector crystals can be modeled in a similar way as detailed above. The length of the detector crystal is optimised so that maximum absorption occurs at the energies needed but not so long that the created electron-hole pairs have time to be reabsorbed before they are swept away by the 3000 V potential applied across the crystal.

4.3.5 Magnetic Compton normalisation

Once the corrected magnetic Compton profile is obtained, to derived a spin moment, the flipping ratio needs to be defined,

$$R = \frac{I^{\uparrow} - I^{\downarrow}}{I^{\uparrow} + I^{\downarrow}}, \tag{4.4}$$

where $I^{\uparrow\downarrow}$ are the integrated intensities for positive and negative polarities, it is the ratio of spin scattering to charge scattering. Referring to Eq. 3.16, the area under the magnetic Compton profile is proportional to the spin moment. The process of normalisation to obtain the spin moment is simple. It requires no further modeling, only the measurement of a known calibration sample to scale the flipping ratio according to the number of electrons involved in the scattering. This flipping ratio depends on experimental conditions (degree of circular polarisation) and thus will not be same on each experiment. Therefore, each sample being measured needs a corresponding calibration sample. To scale the flipping ratio to a spin moment one uses

$$\mu_S = \frac{R_{\text{Sample}}}{R_{\text{Ni}}} \times \frac{n_{\text{electrons}}(\text{Sample})}{n_{\text{electrons}}(\text{Ni})} \times 0.56\mu_B. \tag{4.5}$$

Nickel is generally used as it is known that the spin moment is 0.56 μ_B. Any known sample can be used, for example Fe also may be used. However, as Ni has a relatively small signal, any mistakes in the set up can be identified easily, whereas with Fe where the signal is significantly stronger, subtle differences can be lost.

4.4 Complementary techniques

As a matter of comparison the complementary techniques that are used to gather similar information as magnetic Compton scattering are discussed. The basis logic, advantages and disadvantages behind each of the techniques are discussed.

4.4.1 X-ray magnetic circular dichroism

XMCD is a resonant X-ray absorption technique. Magnetic signals are strongly enhanced on resonance, however, the signals contain information not only on **S** and **L**, but also on the selection rules making determination of these quantities more difficult than with magnetic Compton scattering. **S** and **L** can be estimated utilising the magneto-optical sum-rules [47]. One of the main advantages of the technique is that it uses core level spectroscopy and thus is capable of resolving element specific information.

In an XMCD experiment, a circularly polarised photon is absorbed by a magnetic material into a core state, see (Fig. 4.5). The polarised photon possesses an angular momentum of $m_l = \pm 1$ depending on the helicity of the photon. The core state absorber gains the angular momentum of the photon. Transition probabilities for the absorption of the now spin polarised photoelectron depend on the states available at the Fermi energy thus the spin-up and spin-down bands can be probed dependent on the photon helicity.

In a transition metal, for example, the imbalance of the spin-up and spin-down

populations in the 3*d* shell leads to different absorption coefficients $\mu^{\pm}$ of left and right circularly polarised light at the $L_{2,3}$ edge. Information about the magnetic properties are thus contained in the XMCD spectra, defined as $\Delta\mu(E) = \mu^{+}(E) - \mu^{-}(E)$. The analysis can be extended via the magneto-optical sum rules which can be used to gather great amounts of information of the magnetic properties [49].

The spectra in Fig. 4.6 is from pure cobalt measured at 200 K in an applied field of 3 T on beamline I06 at Diamond, Oxford. The moments are derived by application of the magneto-optical sum rules which work well for early transition metals. Quantitative information is derived through the knowledge of the number of holes, n_h. This quantity is readily calculated with many band structure programs. The application of these rules to non-transitional metal systems can be fraught with difficulty if the system exhibits strong spin-orbit coupling, *jj*-mixing and a non-negligible $\langle T_z \rangle$ term. The technique is

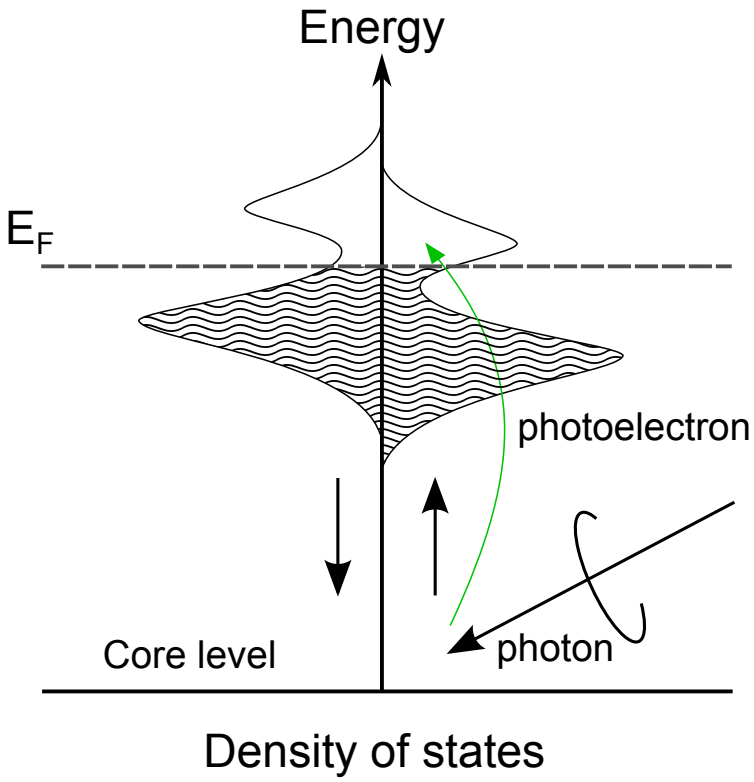

Figure 4.5: Schematic diagram of the absorption of a circularly polarised photon by a ferromagnetic target. Adapted from Ref. [48].

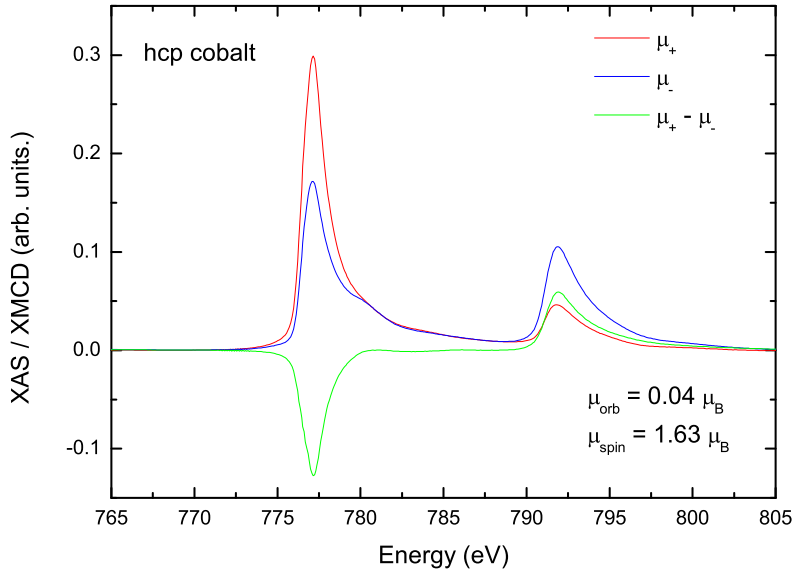

Figure 4.6: XAS and XMCD for hcp cobalt measured on I06 beamline, Diamond. With spin and orbital moments derived from the sum rules.

surface sensitive (when compared with a bulk probe such as Compton scattering) and as such can be seen as either an advantage or a disadvantage depending on what one wishes to measure.

For example, n_h in cobalt is 7.51 [50]. The $\langle T_z \rangle$ operator reduces to zero in this structure. The sum rules in this case are $\mu_{\mathrm{orb}} = -4q(10 - n_h)/3r$ and $\mu_{\mathrm{spin}} = -(6p - 4q)(10 - n_h)/r$. Where the values of q, p and r are values obtained from various points along the integration of the normalised spin split edges. The moments in this case are found to be $\mu_S = 1.63\ \mu_B$ and $\mu_L = 0.04\ \mu_B$.

4.4.2 Polarised neutron diffraction

A polarised neutron diffraction experiment allows the spatially varying components of the magnetisation to be measured because neutrons interact with condensed matter both through the strong nuclear interaction and through electromagnetic interactions. In a polarised neutron diffraction (PND) experiment the magnetisation density $\mathbf{M}(\mathbf{r})$ is measured in the presence of an applied field $\mathbf{B}$.

If the neutron momentum transfer $\mathbf{q} = \mathbf{q}_i - \mathbf{q}_f$ equals a reciprocal lattice vector **G**, i.e. Bragg's condition is satisfied, then scattering occurs both because of the periodicity of the nuclear density and because of the microscopic periodicity of the magnetisation density.

For studies of magnetisation, neutron scattering is an ideal family of techniques and out of these the PND method is one the best known and most widely used. The technique can be used to measure magnetic form factors, which are a reflection of the real space distribution of **J**. To extract **S** and **L**, free atom model form factors are fitted. Furthermore, the technique relies on being able to measure Bragg peaks, some instruments however do not have the range to be able to measure these and therefore observe diffuse moments. When compared to Compton scattering, the techniques reliability on models and Bragg peaks can be a disadvantage. PND however has the ability to measure very small total moments, well below the sensitivity of magnetic Compton scattering. For better sensitivity than neutrons still, muon spectroscopy can be used.

4.5 Sample characterisation techniques

4.5.1 SQUID magnetometry

The method used throughout this thesis for the measurement of total magnetic moments is the technique of SQUID magnetometry. The technique utilises Faraday's Law of electromagnetic induction. The magnetic sample is scanned vertically through a set of superconducting pick-up coils carrying a supercurrent. As the magnetic sample passes through the coils a change in the persistent current is induced in the coils. These coils are in turn coupled to a SQUID device.

The SQUID is a loop generally consisting of two Josephson junctions. A Josephson junction comprises two superconductors bridged by a thin, insulting "weak-link". If the flux through the loop changes (e.g. as a result of a change in the induced current from the pick-up coils) then circulating currents will arise in the ring that will cancel the

change. These currents can be detected by using a phenomenon called the Josephson effect. The Josephson effect is due to Cooper pair tunneling through the weak-link; the supercurrent in a Josephson loop is given by

$$i_s = i_c \sin \Delta\phi, \tag{4.6}$$

where $\Delta\phi$ is the phase difference across the junction and i_s is the critical current. The phase is affected by the vector potential **A** of the induced current. Using this technique, minute changes in the phase result in measurable outputs from the SQUID ring.

The capabilities of commercial SQUID devices vary but the use of Josephson junctions means that it is possible to detect changes in field associated with one quantum of magnetic flux. Sample and SQUID coils are isolated and shielded, so that the sample can be exposed to a range of experimental conditions T = 1.8 - 800 K with fields as high as 7 T. Some commercial SQUID systems can however reach $\sim$ 300 mK with a special He-3 insert.

4.5.2 Laue diffraction

Single crystal samples used in this thesis were checked for quality and alignment using the X-ray Laue technique. The Laue technique uses a polychromatic beam. Using a polychromatic beam means that the sample can be stationary whilst multiple parts of reciprocal space can be sampled simultaneously using the multiple wavelengths of the incident beam. The X-ray beam is incident on the sample and a scintillator screen in back scattering geometry measures the two-dimensional interference pattern. Samples are mounted on a triple-axis goniometer which allows for translations and rotations in all three-dimensions. Once orientated, the crystals are glued to a sample plate, and the rotations needed are transfered to the precision alignment miniature sample goniometer, introduced in the next section.

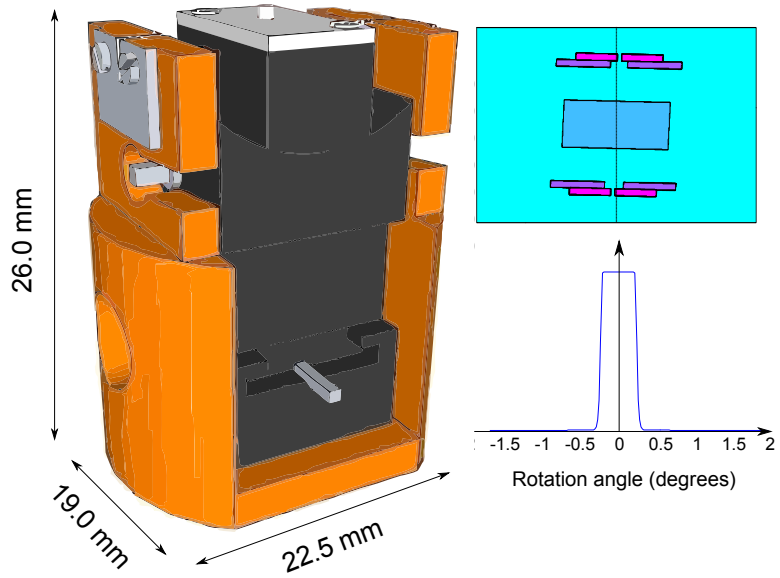

Figure 4.7: (Left) Diagram of the specially designed goniometer used to align the single crystals. The goniometer is the black device inside a brass holder. The tungsten slits are the grey sections. (Right) The angular sensitivity was modeled by using a matrix of attenuation coefficients to describe the goniometer. The matrix was then rotated and the absorption through the center was calculated. From the top of the peak the angular variation is estimated to be 0.5 °

4.6 Precision alignment miniature sample goniometer

To accurately transfer sample orientation from the Warwick Laue diffractometer to the beamline setup on ID15A, a special, high-precision sample holder was created. The holder works by having two tungsten slits about a millimetre below the sample positions, this is used as a reference path in the Laue (see Fig. 4.7). A low power X-ray detector [2] is placed behind the sample holder on the opposite side from the X-ray source. The X-ray beam is then incident on the tungsten slits. The holder is then rotated to maximise the signal from the detector. At this point the rotational position is zeroed. All subsequent angles are taken about this reference point.

The sample holder is then lowered so that the beam is incident on the crystal. Using a backscattering Laue diffraction camera the crystal is orientated until the

[2] The detector is an amplified $CdWO_4$ crystal acting as a scintillator, a second layer which detects scintillations is on top and acts as a current source. Chip from Centronic Ltd.

diffraction pattern of the desired axis is found and aligned. Any adjustments to the θ and ϕ angles are made on a non-magnetic goniometer [3] inside the alignment holder. To realign *in situ* at the ESRF, the same reference zero rotation is found inside the cryomagnet. The synchrotron beam is used to align our sample. The tungsten is found via its fluorescence and the slits located by a drop in intensity as the magnet is rastered along. An X-ray pin diode is placed behind the beam and then the sample is rotated in the magnet until maximum intensity is found. The back detector peak moves in along y as the angle of the goniometer is varied. When the back detector peak is in the middle of the tungsten slit gap the holder is aligned with the beam.

[3] Miniature Charles Supper goniometer. www.charles-supper.com.

Chapter 5

Momentum density studies of complex oxides

5.1 Introduction

The following section details two investigations into the spin density of two ferromagnetic oxides; the spin chain $Ca_3Co_2O_6$ and the metamagnetic ruthenate $Sr_3Ru_2O_7$. The aim of this research was to ascertain which electrons are responsible for the electronic behaviour through a comparison of measured magnetic Compton profiles with molecular orbital calculations and density functional theory. The work in this chapter also outlines some of the highest continuous field magnetic Compton scattering experiments yet attempted.

5.2 Determination of spin density and orbital occupation in $Ca_3Co_2O_6$

5.2.1 Introduction

Low dimensional compounds have been an area of vast interest in recent years; the reduced dimensionality often gives rise to many interesting and novel behaviours, for example low dimensional magnetism, metamagnetism and geometrical magnetic frustration [51, 52, 53]. $Ca_3Co_2O_6$ is in the unique position of providing the opportunity to study of all these phenomena in a single compound as such it is an excellent testing ground for many experimental techniques and theoretical studies.

The rhombohedral structure is shown in Fig. 5.1 (a). The structure consists of ferromagnetic chains of CoO_6 octahedral and trigonal prisms extending up the *c*-axis. These ferromagnetic chains are sat on the hexagonal lattice of the rhombohedral cell (Fig. 5.1 (b)). As well as the strong ferromagnetic intra-chain coupling ($J_{\mathrm{FM}} \sim +$ 25 K), there is also a weaker inter-chain antiferromagnetic coupling ($J_{\mathrm{AFM}} \sim$ - 0.25 K) both shown in Fig. 5.1 from Ref. [54]. This antiferromagetic arrangement on a hexagonal lattice leads to strong geometrical frustration of the CoO_6 chains. A strong magnetocrystalline anisotropy prevents any canting of the moments, and the moment remains highly uniaxial [55].

$Ca_3Co_2O_6$ magnetically orders below 25 K and shows a number of metamagnetic steps in the high field magnetisation (see Fig. 5.3) [56]. It has been suggested that these steps are associated with the formation of metastable states or quantum tunneling of magnetisation [55, 57].

The different crystal fields on the two symmetrically inequivalent cobalt sites result in a high spin state (S= 2) on the trigonal sites (Co_{tri} Co^{3+} $3d^6$) and a low spin state (S=0) on the octahedral sites (Co_{oct} Co^{3+} $3d^6$). Polarised neutron diffraction finds a difference in total moment on the Co_{tri} compared to the Co_{oct} sites. The Co_{oct} is essentially magnetically inactive [58]. The octahedral site has cubic coordination and the

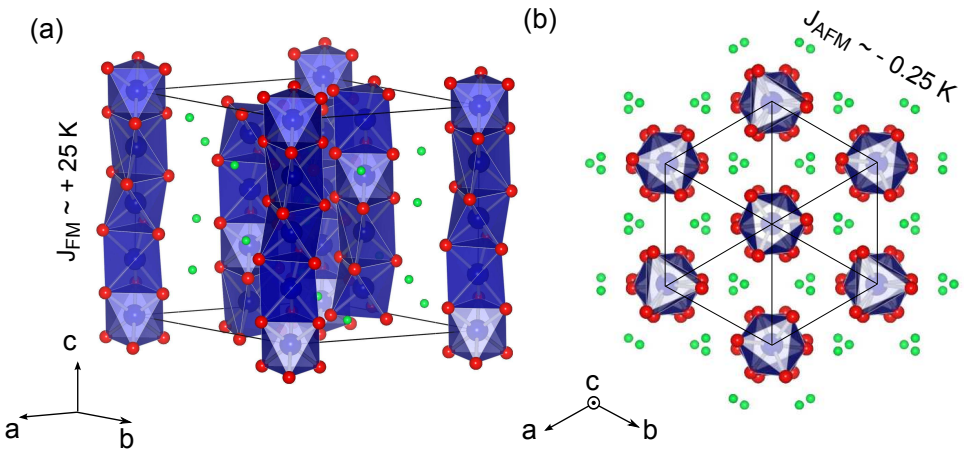

Figure 5.1: Structure of $Ca_3Co_2O_6$, showing (a) the Co_2O_6 chains formed along the *c*-axis and (b) projection along the *c*-axis. Also shown are magnetic coupling constants, in (a) the ferromagnetic in-plane coupling and in (b) the weaker anti-ferromagnetic coupling between chains. Green atoms are calcium, blue are cobalt and red oxygen.

orbital moment is therefore quenched, as per §2.1.4.1. The Co_{tri} site, however, possesses a large spin moment and more surprisingly a large unquenched orbital moment. This is related with the unusual coordination (D_{3h}) of the trigonal prism shown in Fig. 5.2. Unlike the octahedral (O_h) case, the D_{3h} symmetry group allows for the unquenching of the orbital moment. The energy level scheme for both the Co_{oct} and Co_{tri} are shown in Fig. 5.2.

Recent work by Wu *et al.* explored the ground state of the system using the LSDA + U method [59]. They predict that $Ca_3Co_2O_6$ is a ferromagnetic insulator opposing the claim that it is the first one-dimensional ferromagnetic half metal as per Ref. [60]. They also predict a large unquenched orbital moment associated with the double occupation of the xy orbital, which generates a large magnetocrystalline anisotropy. The predicted moments are in good agreement with polarised neutron diffraction data which measures alternating magnetic moments of 0.08 and 3.00 μ_B on the octahedral and trigonal sites respectively [58]. XAS experiments confirmed the valency of both cobalt sites to be Co^{3+} by analysis of the XAS lineshape [61]. The authors also present dichroism studies, however, the studies were restricted to the Co *L*-edges, and unusually they record a total

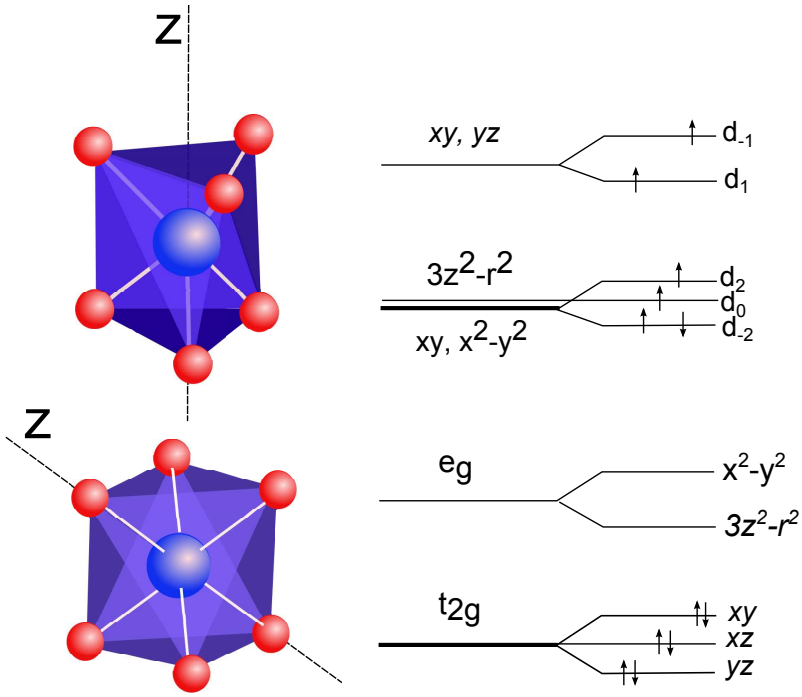

Figure 5.2: (Top) CoO_6 prism with D_{3h} symmetry. Local crystal field energy diagram for Co_{tri} site. (Bottom) CoO_6 prism with O_h symmetry octahedral prism. Local crystal field energy diagram for Co_{oct} site.

moment of 5.66 μ_B somewhat larger than their experimentally measured bulk moment of 5.30 μ_B.

The purpose of this section is to address:

- the size of the spin and orbital contributions to the magnetism.
- the existence of any oxygen magnetism
- the orbitals responsible for the observed magnetism.
- the Hubbard correlation strength U required to reproduce the observed properties.

Table 5.1: Summary of previous studies on $Ca_3Co_2O_6$. KKR, MCS, XMCD results and LSDA + U. (All values in μ_B/f.u.).

Method	Ref.	μ_s Co_{trig}	μ_l Co_{trig}	μ_s Co_{oct}	μ_s O	μ_s Total	μ_l Total	μ_j Total
LSDA + U	[59]	2.99	1.57	0.07	0.78	3.84	1.66	5.66
$XMCD_{sum}$	[61]	-	-	-	-	4.10	1.20	4.80
$XMCD_{sim}$	[61]	-	-	-	-	3.60	1.70	5.30
SP - SREL	This work	2.61	-	0.31	0.9	3.91	-	3.91
REL	This work	2.59	0.43	0.29	0.9	3.78	0.43	4.26
LSDA + U	This work	2.64	1.14	0.30	0.70	3.95	1.11	5.06
MCS	This work	-	-	-	-	3.93	1.3	5.2

5.2.2 Experimental details

5.2.2.1 Sample characterisation

Single crystal samples of $Ca_3Co_2O_6$ were grown by Stephano Agrestini [1] by a flux method. Using a standard solid state reaction, polycrystals of $Ca_3Co_2O_6$ were prepared at 800 °C for 24 hrs, followed by pelleting. The pellets were then heated for 24 hrs at 1000 °C, ground up and then heated again at 1000 °C for 24 hrs. Using 7 - 15 times the mass of KCO_3 to $Ca_3Co_2O_6$ slightly mixed. The mixture was heated in an alumina crucible with an alumina lid. The mixture was then heated in a furnace to 1000 °C to form single crystals, sieved in running water and cleaned in an ultrasonic bath. The high quality of the single crystal was confirmed by energy dispersive X-ray, magnetisation (see Fig. 5.3), specific heat measurements [62] and Laue X-ray diffraction which showed no sign of twinning. The same single crystals have also been measured with neutrons, observing the slow magnetic order-order transition (see Ref. [63]), the field and temperature dependence of ferromagentic and anti-ferromagentic Bragg peaks (see Ref. [64]), nuclear magnetic resonance (NMR) (see Ref. [65]) and resonant X-ray scattering (see Refs. [51, 66, 67]).

[1] Now at Max Planck Institut, Dresden.

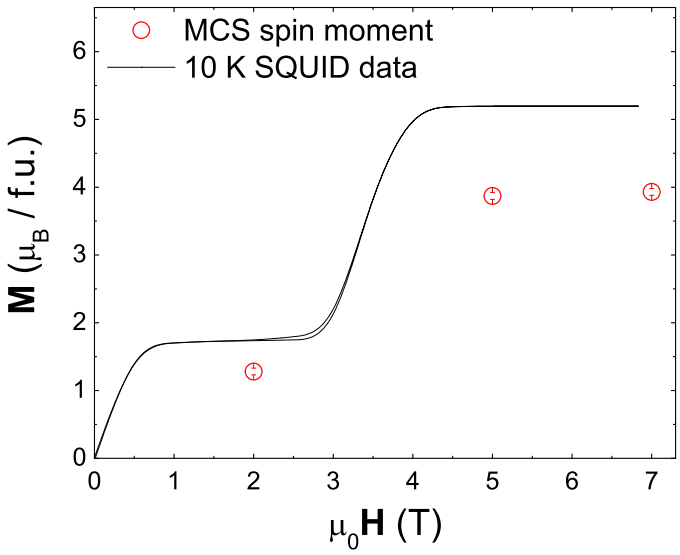

Figure 5.3: SQUID magnetometry for $Ca_3Co_2O_6$ aligned along the *c*-axis at 10 K. Red points are spin moment measurements from magnetic Compton scattering (errors on the spin moment are smaller than the symbol size).

It is known that $Ca_3Co_2O_6$ has an extremely anisotropic magnetisation axis. To characterise by SQUID magnetometry, the sample was placed in a gelatin capsule filled with APIEZON vacuum grease. A large field (7 T) was applied; due to the large magnetocrystalline anisotropy, the torque oriented the *c*-axis along the field. With the field still applied the temperature was lowered to freeze the grease and hold the crystal [68].

Due to this extreme magnetic anisotropy care was needed to transfer the alignment of the *c*-axis from the Laue spectrometer at Warwick to the beamline on ID15A. To achieve this sensitivity a new sample holder was created, from which the angular sensitivity is estimated to better than 0.5°. Details of this sample holder can be found in §4.6.

5.2.3 Results and analysis

5.2.3.1 Band structure calculations

The electronic structure of $Ca_3Co_2O_6$ was calculated using the Munich SPR-KKR package, which utilises a multiple scattering formalism to solve the Dirac equation [26]. The system was calculated in the spin-polarised scalar-relativistic and fully-relativistic mode using lattice parameters from Ref. [69] and using the GGA exchange parameratisation described by Perdew, Burke and Ernzerhof [70]. This exchange parameterisation takes into account not only the local charge density but also the gradient of the charge density to account for sharply changing charge densities as expected in 3*d* electron systems.

The magnetic EMD, $\rho^{\uparrow}(\mathbf{p}) - \rho^{\downarrow}(\mathbf{p})$, was calculated from the self-consistent potentials and projected along the *c*-axis to produce the magnetic Compton profile. The partial densities of state are shown in Fig. 5.4 and shows a half-metallic ground state similar to the bare local spin density approximation (LSDA) calculations of Wu *et al.* [59]. Moments from the calculation are shown in Table. 5.1 and the calculated site specific magnetic Compton profile is shown overlaid with the experimental profile in Fig. 5.5.

5.2.3.2 Magnetic Compton results

The spin polarised Compton profiles were measured along the crystallographic *c*-axis on beam line ID15A at the ESRF. The measurements were made in applied magnetic fields of 2, 5 and 7 T using a superconducting solenoid at a temperature of 10 K.

The magnetic Compton profile at 7 T is shown in Fig. 5.5. Spin moments of 1.78 $\pm$ 0.05 μ_B at 2 T and 3.93 $\pm$ 0.05 μ_B at 5 T and 7 T are shown in Fig. 5.3. In conjunction with SQUID magnetometry, which shows a total moment of 5.2 $\pm$ 0.1 μ_B, the existence of a large unquenched Co orbital moment (1.3 $\pm$ 0.1 μ_B) is confirmed.

There are some surprising features in the profile in Fig. 5.5, at A, B and C, there are "bumps" in the momentum density. These are Fermi surface (Umklapp) features. The presence of these Fermi surface features indicates that there must exist Bloch-like

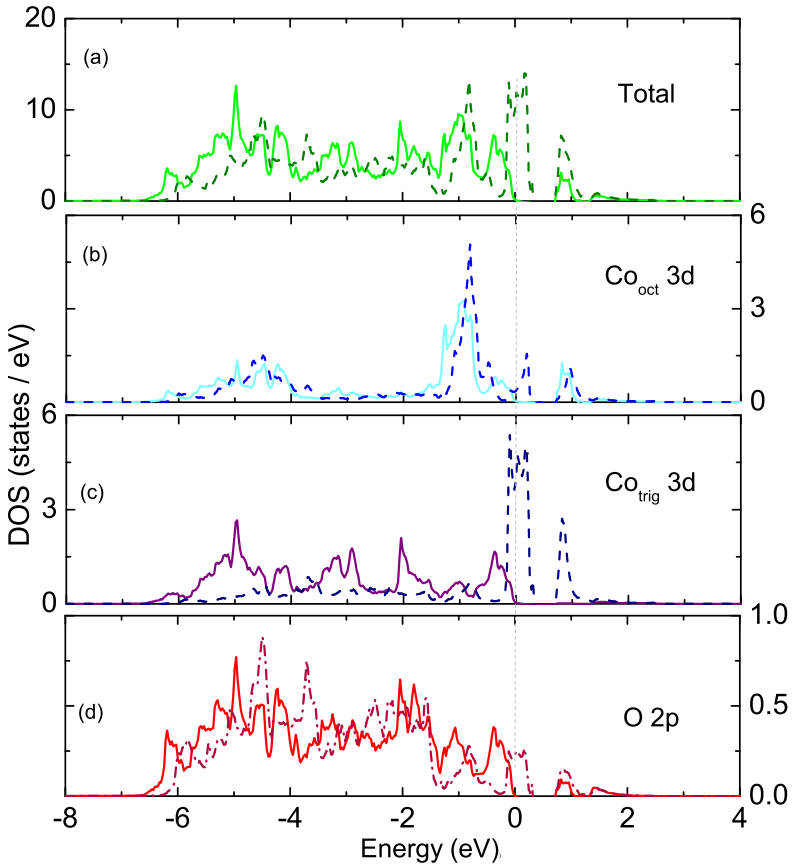

Figure 5.4: Partial densities of state for $Ca_3Co_2O_6$, calculated in the spin polarised state; solid (dashed) line represents spin up (down) states. (a) Total states, (b) Co 3*d* states for the octahedral site, (c) Co 3*d* states for the trigonal site (d) oxygen 2*p* states.

electron states implying some level of metallicity, similar to GGA calculations performed here and by other authors [71, 72]. The data were carefully checked to see if the "bumps" were real. They exist on both sides of the profile (before folding) and are also periodic with the reciprocal lattice vector, **G**, making the existence of the Umklapp features indisputable.

In the calculated momentum density profile shown in Fig. 5.5 it is interesting to note that the Fermi surface features are only visible in the interference term between Co_{oct} and Co_{tri}. The interference term is a term which represents the momentum density of one atomic site on another atomic site. The Umklapp in the interference term suggests that the states at E_F are hybridised cobalt states. Although the size of

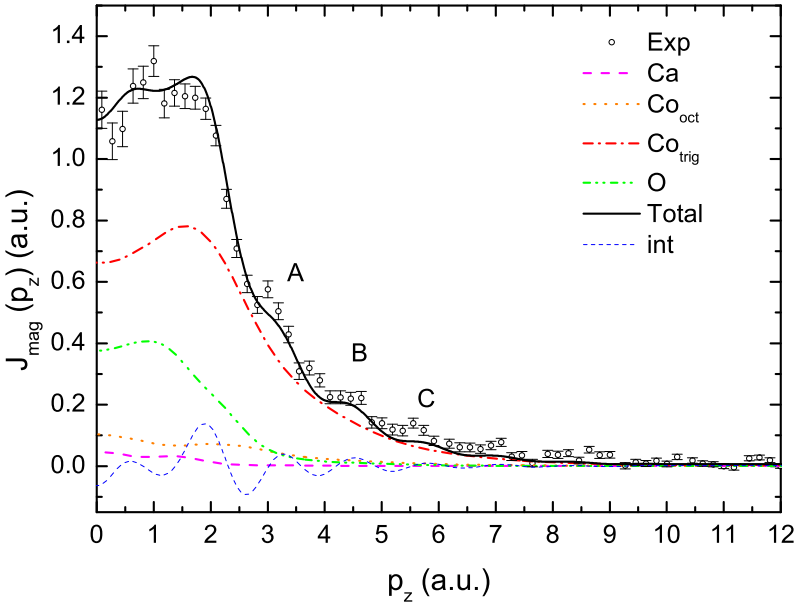

Figure 5.5: Measured MCP at 10 K and 7 T plotted with the corresponding deconstructed KKR predicted profiles.

the interference term looks significant, the moment associated with this interference is only $\approx 0.02\ \mu_B$.

An appreciation of the effect metalicity has on the shape of the MCP can be gained from inspection of Fig. 5.6 where E_F was moved 0.5 eV into a nearby bandgap. The real profile shows sharp peaks associated with the Fermi surface topology. The shifted profile, however, shows a much smoother profile where the Umklapp bumps have disappeared.

5.2.3.3 Resistivity

Resistivity measurements can be highly instructive in elucidating the transport properties of a material. Temperature and field dependencies can identify the transport regime of the charge carriers. Systematic measurements by Raquet *et al.* [73] report that ferromagnetic ordering within the chains does not induce a conductivity change towards

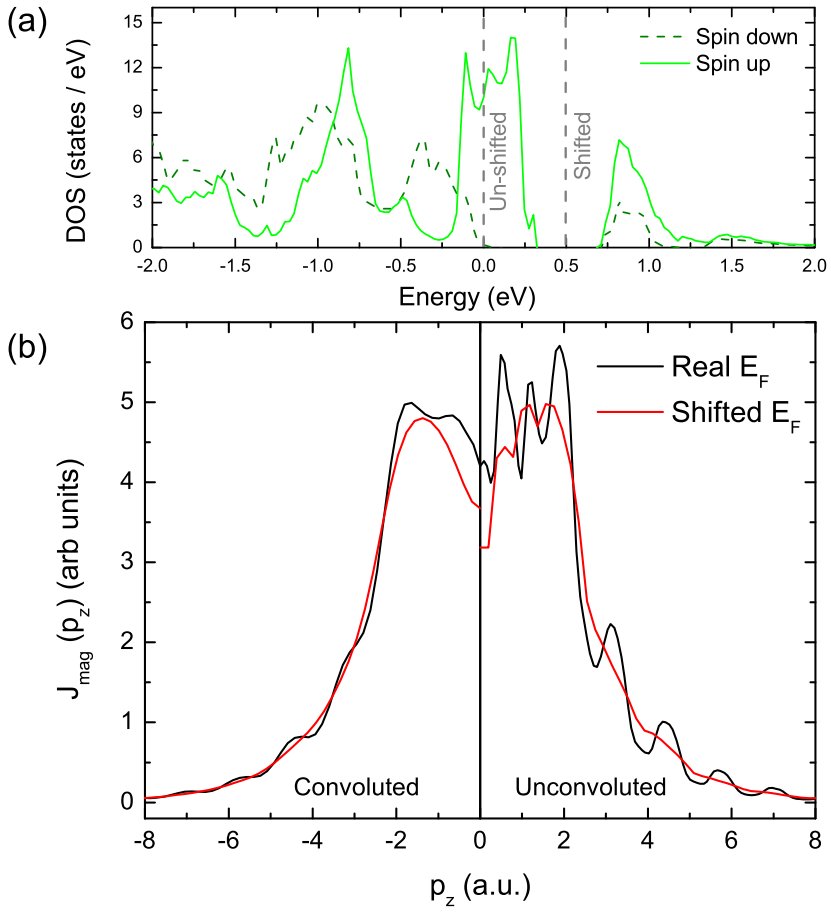

Figure 5.6: Comparison of MCP dependent of the position of E_F, proving that the oscillations in the profile are Fermi surface related. (a) Position of E_F for the unshifted and shifted profiles (b)(Left) Convoluted profiles (Right) Unconvoluted profiles.

metallicity, as is usually observed in transition-metal oxides. They conclude that for the low temperature regime, the resistivity behaviour was consistent with Efros-Shklovskii type conduction, characterised as variable range hopping (VRH) with a soft Coulomb gap, Δ_c, due to Coulomb interactions between the localised electrons [74].

The work by Wu *et al.* concludes the system is an insulator i.e. $N(E_F) = 0$ with a high Hubbard *U* parameter $\geq$ 5 eV, resulting in a band gap of approximately 1 eV. Whilst seemingly satisfactory for the observed magnetism this does not describe the high 1D density of states ($N_1(E_F) \approx 2.5 \times 10^{11}$ eV^{-1}n^{-1}) required for VRH shown by Raquet *et al.*.

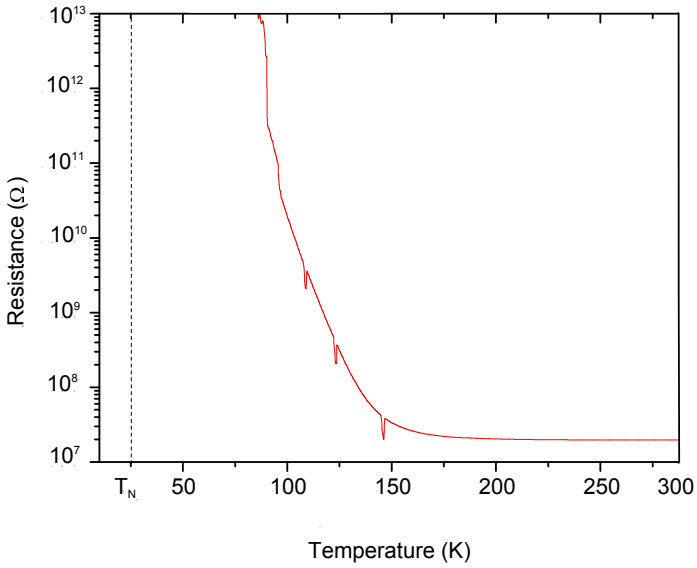

Figure 5.7: Temperature dependence of resistivity for $Ca_3Co_2O_6$ measured along the *c*-axis in a field of 7 T. The "dips" in the recorded data are associated with the electrometer autoranging its sensitivity.

To investigate the apparent Fermi surface implied by the magnetic Compton scattering data, resistance measurements were taken along the *c*-axis. Due to the large room temperature resistance ($\approx 10^8\ \Omega$) a special high resistance set up was used. The sample environment was provided by a Quantum Design PPMS with connections made to a Keithley 6517A electrometer designed for ultralow current measurements, the electrometer was then interfaced with LabView. The measurement showed a room temperature resistance of 300 kΩ rising exponentially with reducing temperature to above $10^{15}\ \Omega$. the temperature dependence of the resistivity is shown in Fig. 5.7, the little "dips" are associated with the auto-ranging feature of the electrometer.

Measurements were made with and without an applied magnetic field of 7 T applied. Measurements in the *ab*-plane were three orders of magnitude higher. No evidence was found for a metallic ground state or a field induced metallic state. As such, the nature of the observed Fermi surface effects remain a mystery. It is worth noting, however, that work by Raquet *et al.* was performed on "needle-like" single crystals, this Compton study however was performed on large crystals that were composed of many

"needle-like" single crystals. Boundaries between adjacent crystals could be the cause for the lack of any transport information in our crystals.

5.2.3.4 Effect of Hubbard-U parameter

In strongly correlated oxides such as $Ca_3Co_2O_6$, the electrons not only feel the potential from other electrons but they will also feel their own potential (self-interaction). This is not accounted for in the LSDA/GGA. In the following section, band-structure calculations for $Ca_3Co_2O_6$ have been performed in the LSDA + U formalism to better describe this self-interaction.

Spin polarised, FLAPW calculations with spin-orbit coupling in the LSDA + U formalism were performed using the ELK code [27]. The Perdew-Wang/Ceperley-Alder functional was chosen as the local-density exchange-correlation potential. For ease of comparison muffin-tin radii from Wu *et al.* were used. The basis set cut-off parameters

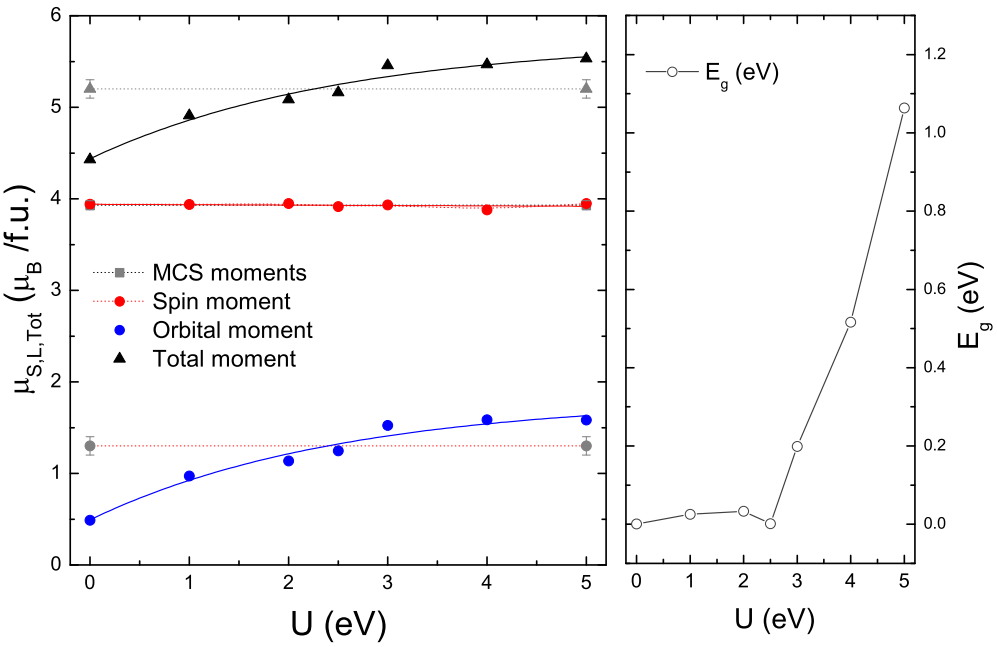

Figure 5.8: Dependence of the magnetic moments and band gap, E_g in $Ca_3Co_2O_6$ on the correlation strength U from ELK.

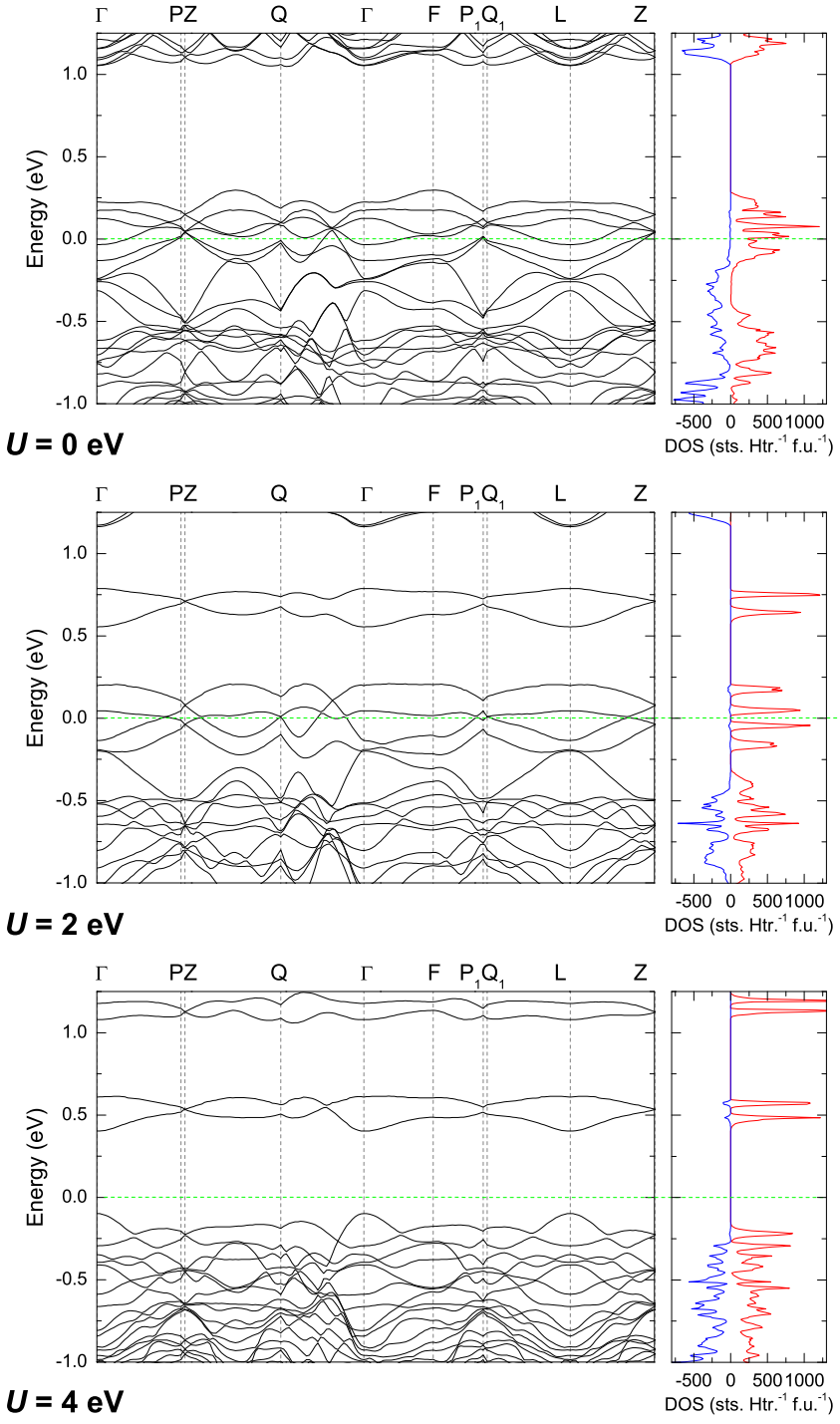

Figure 5.9: Band structure and density of states for $Ca_3Co_2O_6$ with $U = 0$, 2 and 4 eV. J = 0.9 eV.

were $G_{\max} = 14$ and $R_{\mathrm{mt}}K_{\max} = 7$. Integrations over the irreducible wedge of the Brillouin zone were performed using a 500 *k*-point regular mesh. The potential and the total energy were converged to a tolerance of 10^{-5} Ryd and 10^{-3} Ryd respectively. The calculations were performed with a fixed spin moment set to be the experimental spin moment of 3.93 μ_B / f.u. along the *c*-axis. Moment and band gap comparisons were made as a function of the Hubbard correlation parameter *U*, whilst *J* was left as the atomic value of 0.9 eV as per Ref. [59].

The aim in this section is to determine what value of *U* is required to give us the spin and orbital moments measured in the magnetic Compton scattering experiment but importantly not open a significant band gap, as signatures of a Fermi surface are clearly observed in our magnetic Compton measurement. Fig. 5.8 shows the dependence on the *L*,*S* and *J* as a function of *U*. As the moment is fixed, no significant change in the spin moment is observed. The orbital moment however shows a dramatic dependence on *U*. The value which corresponds to our experimental value is $\sim$ 2 eV.

The bandstructure of three selected *U* values is shown in Fig. 5.9. For the bare LSDA ($U = 0$ eV) it can be seen that many bands of majority spin character cross E_F consistent with the half metallic ground state previously shown by KKR calculations in §5.2.3.1. The optimum *U* value in terms of the magnetic moments is $U \sim 2$ eV and one can see that there are many states around E_F, but E_F itself lies conveniently in a hybridisation gap with a size no more than 0.03 eV. Using a higher correlation factor still leads us to the situation in the $U = 4$ eV panel and the situation suggested by Wu *et al.* The bands are further separated around E_F and there exists a large band gap $\approx$ 0.5 eV. This value is inappropriate both in terms of the orbital moment and the large bandgap. Due to a limitation of the ELK code the momentum density distributions of these calculations have not been calculated for comparison.

Further work is needed in this area to:

- confirm the existence of any Fermi surface sheets

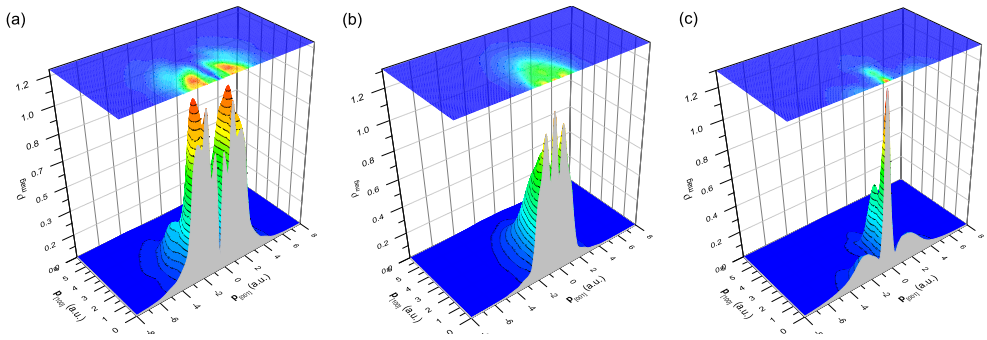

Figure 5.10: Projections of the molecular orbital electron momentum density for the (a) yz, xz orbitals (b) $x^2 - y^2, xy$ orbitals (c) $3z^2 - r^2$ orbital projected into the *ac*-plane

- see what effective masses correspond to the Fermi surface (FS) sheets with an aim to explaining the electrical transport properties.

- compare LSDA + U profiles to experiment. The momentum density of potentials calculated by ELK is a project underway at Bristol University. The shape of the profile as a function of *U* may prove greatly informative in these strongly correlated oxides.

5.2.3.5 Orbital fitting results

As detailed in §2.2.1.3 the momentum space distribution can be described by a linear combination of atomic orbitals LCAO in momentum space

The model for $Ca_3Co_2O_6$ is shown in Fig. 5.2. The model consists of six cobalt valence electrons; five electrons occupy the five 3*d* spin up orbitals, the sixth occupies one of the spin down states. Theoretical work by Wu *et al.* suggests that it is the xy orbital that is doubly occupied. As the magnetic Compton profile represents the momentum distribution of all unpaired electrons, the shape of the Compton profile should reflect which orbitals are singularly occupied.

To investigate the orbital occupancy, the magnetically active CoO_6 prism (trigonal) was modeled as a cluster using the GAMESS quantum chemistry code [22]. A restricted Hartree-Fock calculation was performed using the TZV basis set described

by Schäfer *et al.* [75]. The cluster is then embedded in ≈ 800 point charges to mimic the crystal environment. The 3D molecular wavefunctions are directly related to the momentum space wavefunctions via a 3D Fourier transform. To represent the Compton profile the momentum density is projected along the two perpendicular axes.

For the [001] direction the Compton profiles of the xy and $x^2 - y^2$ orbitals are identical, as are the yz and the xz. Only the $3z^2 - r^2$ orbital has a unique distribution along the *c*-axis. Therefore, the only profiles fitted to our data were these three.

Due to the unconstrained nature of the fitting (three independent fitting parameters and only one set of data to fit to) an argument using the virial theorem is invoked. It is assumed that the correct description of the electron distribution is the one with the lowest total energy (TE). The virial theorem tells us that the kinetic energy KE = -TE. The momentum distribution is related to the kinetic energy and note that the second moment of the momentum distribution $\rho(\mathbf{p})$ is also given by the second moment of the Compton profile:

$$\begin{aligned} \mathrm{KE} &= \frac{1}{2m}\int p^2\rho(\mathbf{p})\ \mathrm{d}\mathbf{p}, \\ \mathrm{KE} &= \frac{3}{2m}\int_{-\infty}^{\infty} p^2 J(p)\ \mathrm{d}p, \\ \mathrm{KE} &= \frac{3}{2m}\sum_i \int_{-\infty}^{\infty} a_i p_i^2 J(p_i)\ \mathrm{d}p_i, \end{aligned} \tag{5.1}$$

following the notation of Cooper *et al.* [31]. The argument followed is from an appreciation that the tails must follow those of a free-atom. If the tails did not follow the free-atom distribution then the second moments would be vastly different implying very large cohesive energies. In fact the cohesive energy is effectively associated with changes in the low-momentum line shape and the free-atom behaviour in the tails can be used to verify that the line shape has been correctly deduced from the observed spectrum.

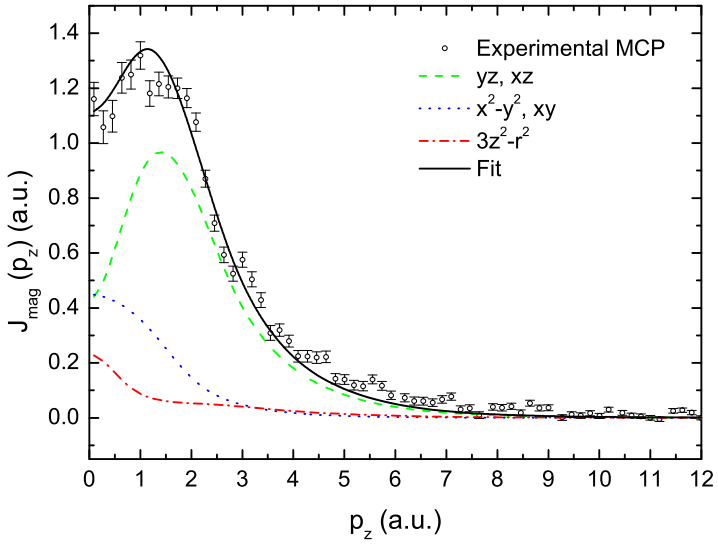

Figure 5.11: Magnetic Compton profile and fitted curves. Green curve is the xz, yz degenerate orbitals, the blue shows the $x^2 - y^2, xy$ degenerate orbitals and the red is the $3z^2 - r^2$ orbital. The black shows the fitted momentum distribution with spin moments shown in Table. 5.2.

This argument is used to better constrain the fit. It is known that the momentum profiles in any other (arbitrary) direction should (at high-momentum) closely follow that of a 3*d* free-atom profile. The tabulated calculations from Biggs *et al.* [76] are used and fitted from 3 a.u. outwards to the free atom profile for the [100], [111] and the [110] simultaneously with the [001] profile of $Ca_3Co_2O_6$. In this way the predicted orbital scheme is robust and feasible. Excluded from the fit are the band-structure related features (Umklapp bumps), which cannot be accounted for in the GAMESS method as they rely on a periodic system of Bloch states.

In the trigonal coordination the yz and the zx become degenerate and the xy becomes degenerate with the $x^2 - y^2$ shown in Fig. 5.2. The unquenching of the orbital moment is allowed on the Co_{tri} prism because of these degeneracies. The double occupation of one of the $m_l = \pm 2$ orbitals would allow a rotation of the spin down $m_l = \pm 2$ into the $m_l = \mp 2$ generating an orbital moment $\mu_l = 2\ \mu_B$, close to the observed 1.3 μ_B, (in agreement with Refs. [59, 61]). The value of the $x^2 - y^2, xy$

Table 5.2: (Upper) Spin density in respective CoO_6 molecular orbitals evaluated from the fitting analysis. Errors on fit are estimated to be $\pm$ 0.05 μ_B. The value for O 2*p* is from a Mulliken population analysis where the spin density is projected back onto an atomic site. (Lower) Spin density in the pure cobalt orbitals from GAMESS and ELK calculations (in μ_B).

CoO_6	xz, yz	x^2-y^2, xy	$3z^2-r^2$	O 2*p*
	2.65	0.77	0.33	0.91

Co	xz, yz	x^2-y^2, xy	$3z^2-r^2$	
GAMESS	1.90	0.65	0.35	-
LSDA + U ($U = 2$ eV)	1.34	0.92	0.38	-

band being nearly than unity confirms the double occupancy of one of the x^2-y^2, xy orbitals.

In Fig. 5.11, the fitted results of the CoO_6 cluster are shown, the best fit is for either the xy or the x^2-y^2 becoming doubly occupied (due to the projected nature of the measurement, determination of which one is not possible). Table 5.2 shows the spin density associated with each molecular orbital and each cobalt orbital.

A Mulliken population analysis reveals that the spin density associated with the six oxygen atoms in the CoO_6 cluster is approximately 0.9 μ_B, in excellent agreement with calculations performed here and other published band structure calculations.

Comparing the MO predictions for each cobalt orbital with those calculated by the $U = 2$ eV optimised ELK calculations can be done by examining the density matrix in the LSDA + U formalism. The comparison is shown in the lower part of Table 5.2. The reason for the comparably high predicted MO occupancy in the xz, yz band is likely due to some contamination from the Co_{oct} site, which in the MO scheme is assumed to contribute nothing to the MCP, which may not be true.

5.2.4 Conclusions

The spin density of the 1D spin chain $Ca_3Co_2O_6$ has been measured using magnetic Compton scattering from which spin and orbital moments are obtained and their origins are discuss with respect to molecular orbital calculations. The deconstructed site-projected profiles emphasises the metallic nature of the system, seemingly at odds with published LSDA + U and resistivity measurements work. Molecular orbital calculations elucidate the populations of cobalt 3*d* orbitals and their relevance to the observed magnetic and electronic behaviour. The double occupancy of either the $x^2 - y^2, xy$ degenerate orbital is confirmed providing an explanation to the giant orbital moment in-line with XMCD and LSDA + U published paper. The presence of a Fermi surface is discussed with the aid of ELK calculations to refine the correlation factor required to best explain this system. A value of $U = 2$ eV is suggested that is consistent with our experimental data and PND,XMCD and LSDA + U data. For this value of *U*, E_F sits in a hybridisation gap of majority spin electrons.

5.3 Spin density and orbital occupation in the quasi 2D ruthenate $Sr_3Ru_2O_7$

5.3.1 Introduction

The Ruddlesden-Popper phases of ruthenates $(Sr,Ca)_{n+1}Ru_nO_{3n+1}$ have been investigated intensively over recent years owing to their varied electronic properties. Amongst these varied properties the strontium members exhibit band ferromagnetism, strongly enhanced paramagnetism, spin triplet superconductivity and metamagnetism [77, 78, 79]. The subject of this section is $Sr_3Ru_2O_7$ which is a quasi-2D system on the verge of ferromagnetism but unlike its sister compound, Sr_2RuO_4, it is not a superconductor.

In zero field, and at the lowest temperatures $Sr_3Ru_2O_7$ is a paramagnet. However, susceptibility measurements show a large Wilson ratio suggesting the system is on the verge of a magnetic phase transition from paramagnetic to ferromagnetic. Ordering

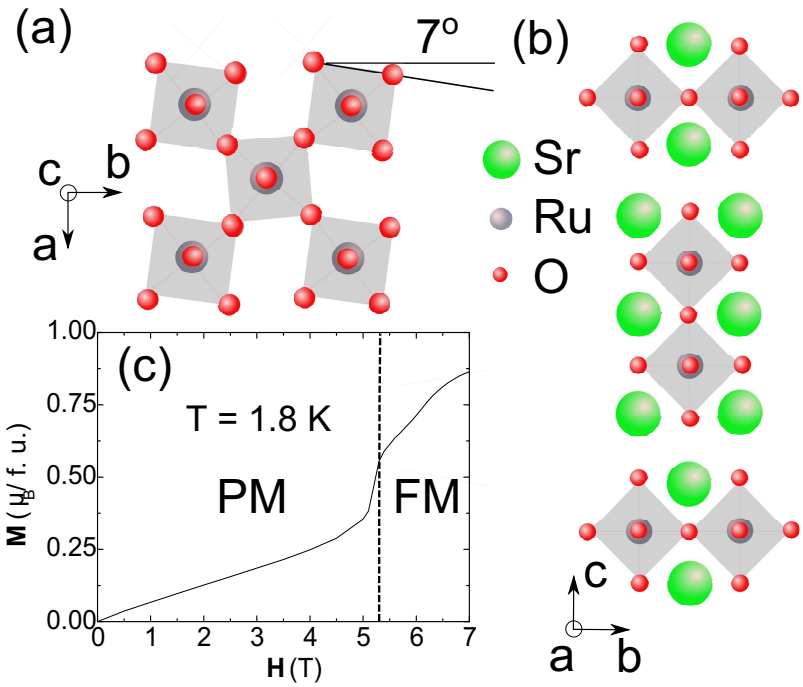

Figure 5.12: Structure of $Sr_3Ru_2O_7$. (a) *ab*-projections showing the rotations of the RuO_6 octahedra. (b) Crystal structure along the *c*-axis. (c) Metamagnetic behaviour in the *ab*-plane from a paramagnetic to ferromagnetic phase measured at 1.8 K.

occurs via a metamagnetic transition above 5.3 T and in the highest quality samples further transitions occur at 5.8 and 6.3 T, Fig. 5.12 (c) [79].

The phase diagram of $Sr_3Ru_2O_7$ reveals that the end-point temperature of phase transitions in the *ab*-plane is very low ($\sim$ 1.5 K) and in the *c*-direction vanishes. Shown in Fig. 5.13 is a phase diagram where the exponent of the resistivity expression $\rho = \rho_{\mathrm{res}} + AT^{\alpha}$ is shown to deviate from the $\alpha = 2$ expected for a correlated electron metals as $T \rightarrow 0$. This provides the opportunity to study new phases of matter where Fermi-liquid theory breaks down [80].

The understanding of the local density of states at E_F is crucial in this system. From angle-resolved photoemmision spectroscopy (ARPES) the Fermi surface was mapped and it was demonstrated that nesting was far less prominent in $Sr_3Ru_2O_7$ than Sr_2RuO_4, offering a possible explanation to why there is no observed superconductivity in $Sr_3Ru_2O_7$ [81]. This work was followed up by LSDA calculations which agreed with the reduction of nesting features and showed that the density of states at E_F consisted of lower energy Ru, crystal field split t_{2g} orbitals hybridised with O *p*-orbitals [82]. The

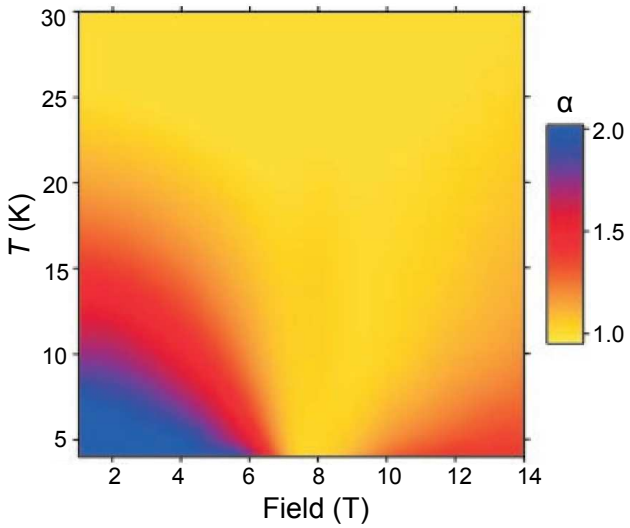

Figure 5.13: Phase diagram of $Sr_3Ru_2O_7$ determined from resistivity measurements showing the exponent for the expression $\rho = \rho_{\mathrm{res}} + AT^{\alpha}$ in the *c*-axis. Taken from Grigera *et al.* [79].

measured and predicted Fermi surface show that the Fermi surface is comprised of a largely two-dimensional sheet of Ru t_{2g} character as well as a small contribution from the e_g manifold both largely hybridised with the surrounding oxygen orbitals [83, 82]. This is in contrast to the cuprate superconductors whose Fermi surfaces are characterised by a $3z^2 - r^2$ hole. Interesting comparisons between the ruthenates and the cuprates can be made on the route to high temperature superconductivity.

All the properties of the strontium ruthenate phases are related to the coordination of the Ru^{4+} ion with six surrounding oxygens. The valence electronic structure from low energy to high should consist of O 2*p* derived states, followed by exchange split t_{2g} levels around E_F, and finally unoccupied Ru e_g levels. However, the density functional band structure is not in accord with this simple picture [84]. The t_{2g} levels have their degeneracy lifted and mix with higher energy e_g states.

The situation is further complicated by structural distortions present in some of the ruthenates where there exists a rotation of the RuO_6 octahedra. These distortions were refined by Shaked *et al.* who determined the real structure not to be the tetragonal *I4/mmm* but instead the orthorhombic *Bbcb* with a rotation of the RuO_6 octahedra of about 7° [85]. The distortion narrows the t_{2g} manifold increasing the density of states, leading to a magnetic ground state via the Stoner mechanism, this rotation induced magnetism is why ferromagnetic ordering is not observed in Sr_2RuO_4 [2].

A NMR study estimated the oxygen contribution to the spin density to be large, about 20 - 40 % of the total [86]. This is in contrast to the end series ferromagnetic member, $SrRuO_3$ which was found by a combination of magnetic Compton scattering and molecular orbital calculations to have an oxygen moment no more than 12 % [9]. The aim of this section is to:

- determine the distribution of the Ru 4*d* moment and investigate the extent of the hybridisation between the Ru d_{xz}/d_{xy} and the oxygen p_z and p_y orbitals leading

[2] The Stoner criteria is $D(E_F)I > 1$ where $D(E_F)$ is the density of states at the Fermi level and I is a measure of the strength of the exchange parameter.

to π-bonding, in contrast to the superconducting cuprates.

- investigate the size and role of any orbital moment present.
- determine which orbitals take part in the metamagnetic transition.

The value of a magnetic Compton measurement is that it measures solely the spin density, and with further analysis the constituent parts of the total spin density can be obtained. The other ferromagnetic member of the family, $SrRuO_3$ is a band ferromagnet and has been studied by magnetic Compton scattering [9]. This study, however, was performed with a powder sample, meaning that directional information such as anisotropic bonding and hybridisation effects are lost through spherical averaging. For these systems where oxygen contributions to both the ferromagnetic exchange and bonding are important, experiments must be performed on high-quality single crystals to retain the directional information.

5.3.2 Experimental details

5.3.2.1 Sample characterisation

For this investigation a single crystal of $Sr_3Ru_2O_7$ was used, the crystal was grown by Dr. Robin Perry at Edinburgh University in a floating-zone image furnace by a method described in Ref. [87], detailed specific heat, resistivity, static susceptibility and magnetisation measurements are also reported in Ref. [87]. Single crystal from the same grower have also been characterised and studied by ARPES (see Ref. [83]), NMR (see Ref. [86]), Hall effect measurements, (see Ref. [88]), ac-susceptibility under hydrostatic pressure, (see Ref. [89]) and de Haas-van Alphen (see Ref. [90]). The dimensions of the crystal used in this investigation was approximately $1 \times 2 \times 2$ mm. The high quality of the sample was confirmed by SQUID magnetometry (Fig. 5.12(c)) which confirms sharp metamagnetic transitions and by Laue diffraction which showed little sign of twinning along the *c*-axis, Fig. 5.14.

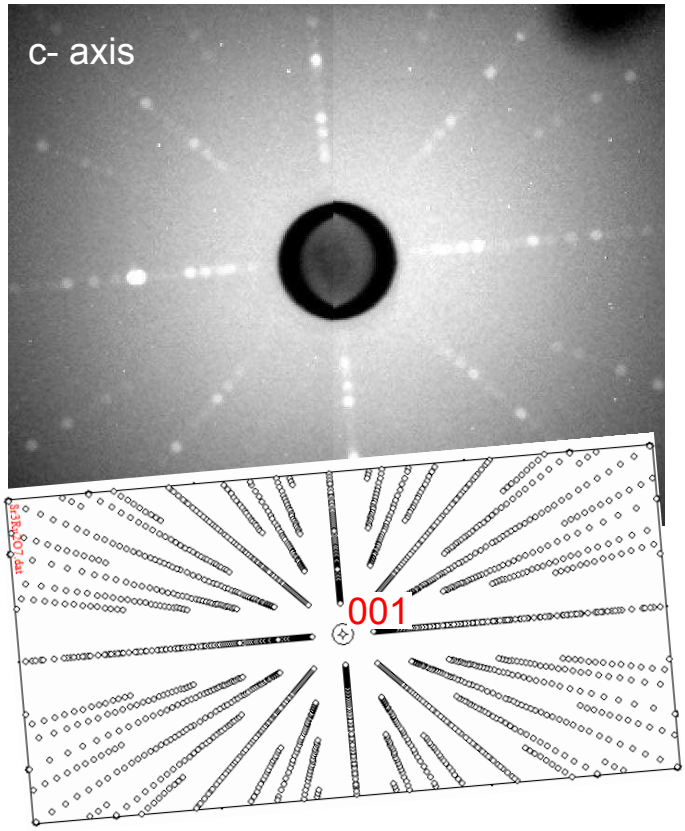

Figure 5.14: Laue images from the 1 × 1× 2 mm single crystals of $Sr_3Ru_2O_7$ along the *c*-axis.

5.3.2.2 Magnetic Compton scattering

To probe the momentum space distributions of the magnetic electrons, spin polarised Compton scattering was used. Unlike complementary techniques such as ARPES or XMCD, the high X-ray energies used in these experiments mean that the bulk electronic structure is measured.

Spin polarised Compton profiles were measured on beamline ID15A at the ESRF, Grenoble. The measurements were made in an applied magnetic field of ± 6 T for the *ab*-plane and ± 8 T for the *c*-axis using a superconducting solenoid. The sample temperature was 1.5 K, the field was reversed every 15 minutes in order to measure the difference profile.

Figure 5.15 shows the experimental MCPs, the relatively low statistics can be

attributed to the small magnetic signal of the sample and the large number of scattering electrons. It is important to note that such a continuous high-field, low-temperature magnetic Compton experiment has never been attempted.

5.3.3 Analysis

5.3.3.1 Magnetic Compton Results

By comparison with the flipping ratio of nickel, as measured under the same conditions the spin moment was found to be 0.70 $\pm$ 0.03 μ_B/ f.u.. From SQUID magnetometry in Fig. 5.12 (c) a total moment of 0.71 $\pm$ 0.01 μ_B / f.u. was shown, this suggest an negligible orbital moment of 0.01 $\pm$ 0.03 μ_B / f.u..

5.3.3.2 Band structure calculations

Band structure calculations were performed by Tom Haynes at Bristol University with the LMTO method as described elsewhere [91]. The calculations were performed in the orthorhombic *Bbcb* structure using an LSDA functional. The paramagnetic band-structure and Fermi surface were found to be in excellent agreement with previous calculations [82], and all the major sheets identified by Tamai *et al.*, corresponding to the α, β, γ and δ orbits, were found to be present [83].

A spin-polarised calculation was then performed in which the spin moment was found to be 1.5 μ_B/Ru, somewhat larger than previous calculations, found for example in Ref [82]. This may be ascribed to a combination of the use of a different form of LSDA functional and the different partitioning of space within the codes and, importantly. The spin moment was found to be 81% Ru 4*d* character with O 2*p* contributing approximately 18% of the total spin moment, see Table 5.3. Furthermore, the majority of the oxygen moment was on the in-plane atoms, suggesting strong π-bonding of the in-plane Ru 4*d* orbitals with the O 2*p*.

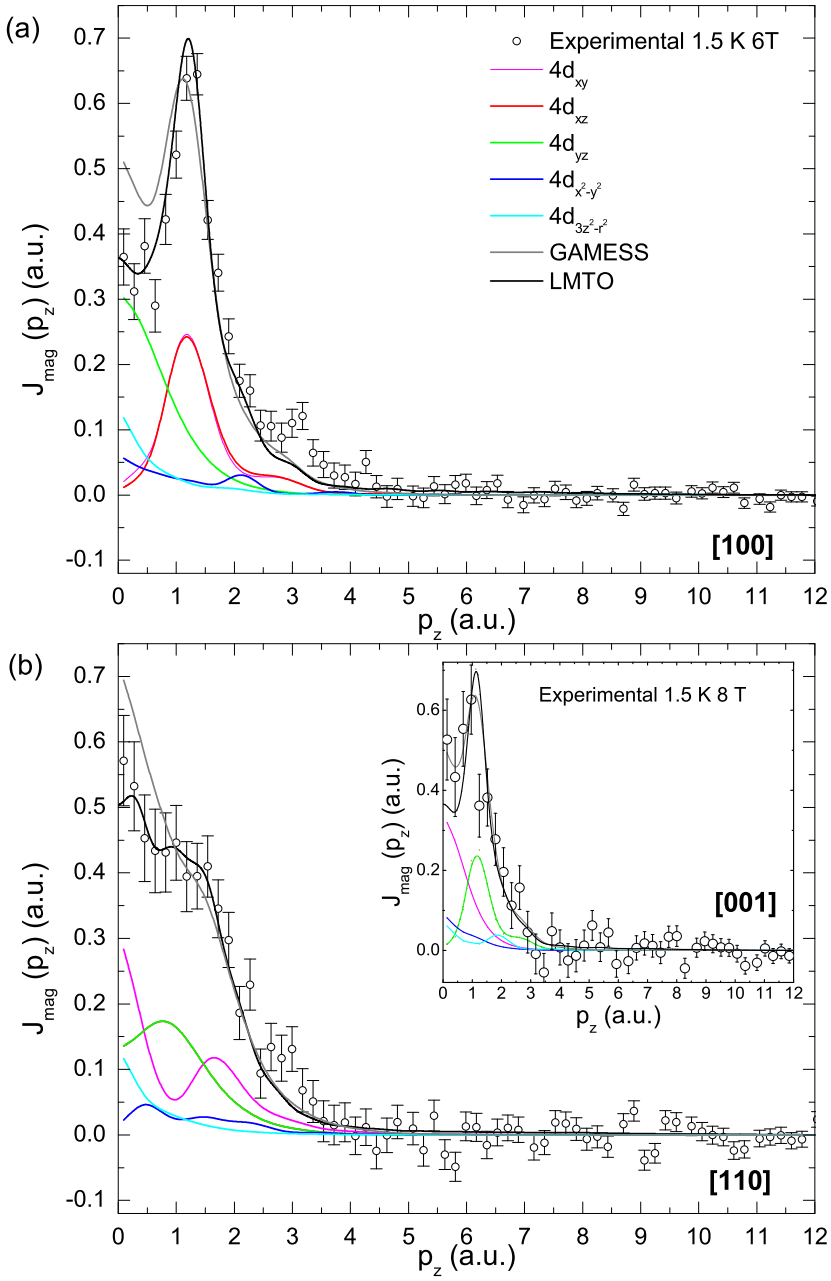

Figure 5.15: One-dimensional spin density projections of $Sr_3Ru_2O_7$ along the (a) *a* and (b) *b* and (Inset) *c* crystallographic directions. Plotted with molecular orbital predictions fitted to the *a* and *b* data and LMTO predictions.

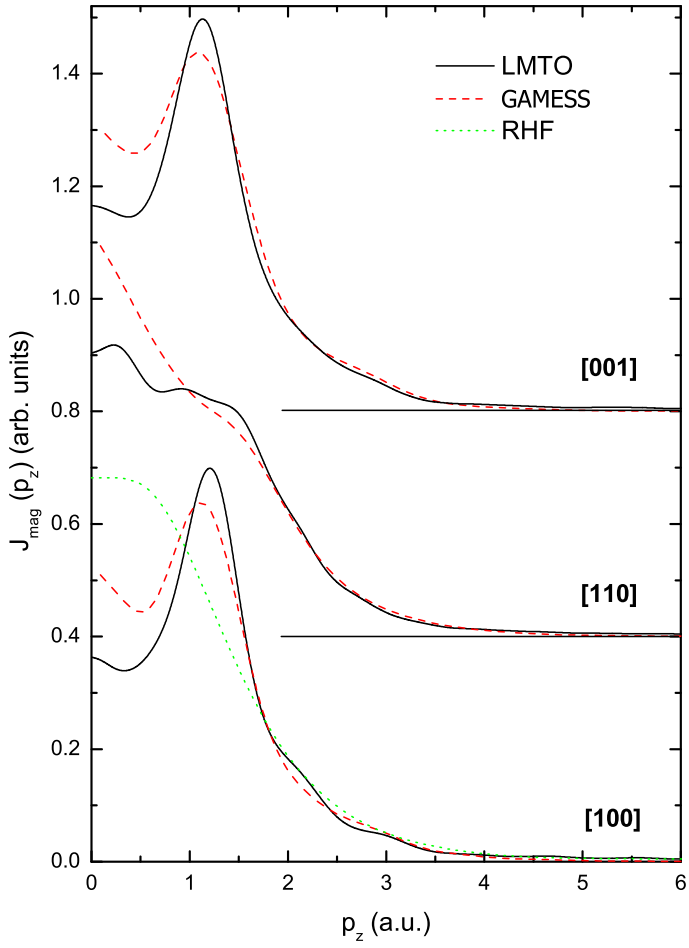

Figure 5.16: Comparison of momentum profiles, derived by three different methods (GAMESS, LMTO and RHF calculations).

5.3.3.3 Molecular orbital calculations

As with $Ca_3Co_2O_6$, the momentum space distribution can be described by a LCAO in momentum space. An *ab initio* restricted open Hartree-Fock (ROHF) molecular orbital calculation was performed for a $(RuO_6)^{8-}$ octahedra using the GAMESS quantum chemistry code [22], the valence electrons are described by a triple zeta valence basis set while the core electrons are replaced by effective core potentials described by Hay and

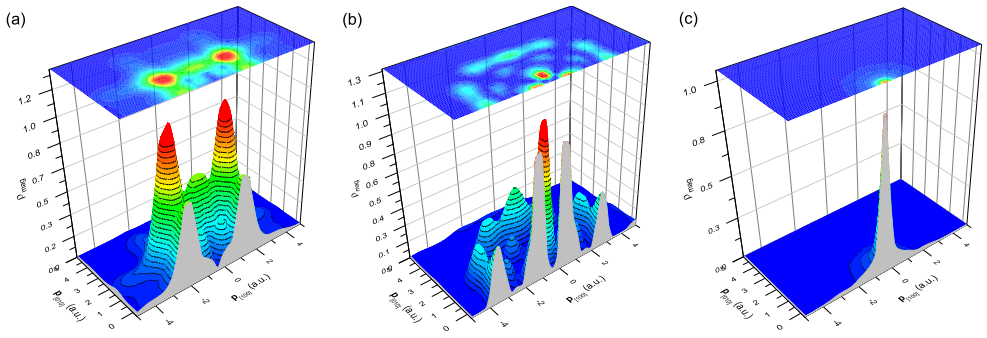

Figure 5.17: Spin density for the (a) t_{2g}, (b) $x^2 - y^2$ and the (c) $3z^2 - r^2$ manifolds projected into the *ab*-plane.

Wadt [92]. The profiles were calculated for a real-space grid of 16 $\times$ 16 $\times$ 16 Å. The $(RuO_6)^{8-}$ cluster was then embedded in an environment of about 1000 point charges to describe the crystal potential, the point charges were placed on crystallographic sites describing the *Bbcb* space group refined by Shaked *et al.* [85].

The three dimensional molecular real-space wavefunctions are directly related to the momentum-space wavefunctions via a 3D Fourier transform, and then twice projected to represent the Compton profile. The calculated profiles were broadened by the experimental resolution (0.44 a.u.) and then the respective five molecular orbitals are fitted to the experimental data, this allows us to investigate the occupancy of each orbital using the constraints of real experimental data.

Due to the lower statistical precision, for a better constrained fit, the occupancy of xy, xz and yz molecular orbitals were set to be equal, as to extract an occupancy for the total t_{2g} band. Again, the e_g states were set as the sum of $x^2 - y^2$ and $3z^2 - r^2$. A dependent fit was performed on the [100] and the [110] directions but not the [001] direction as the statistics were deemed too poor to improve the fit (though the predicted profile reproduces the [001] satisfactorily). The results of the fit are shown in Fig. 5.15. The occupancy of each orbital is shown in Table. 5.3 along with those calculated in the LMTO method.

Oscillatory features similar to those reported by Koizumi *et al.* are present in the

[100] data for the $x^2 - y^2$ orbital and in the [001] data for the $3z^2 - r^2$ orbital, these represent the bonding in those directions coordinated between the Ru and the O, the heights of the 'bumps' are larger than those seen in $La_{2-2x}Sr_{1+2x}Mn_2O_7$, indicative of the stronger hybridisation between Ru 4*d* and O 2*p* states.

In Figure. 5.16, GAMESS predictions, LMTO profiles and Hartree-Fock free atom profiles are shown for an assumed Ru^{4+} ion [76]. The RHF clearly fails to represent the nature of the momentum distribution, this is due to charge transfer from the Ru atom to the surrounding O atoms, this leads to a contraction in real space and a corresponding expansion in momentum space. The GAMESS profile does slightly better, reproducing the high end tails and low momentum dip adequately.

Hiroaka *et al.* found it necessary to consider other hybridised bands as extra contributions, they ascribe some of the low momenta discrepancy to a small negatively polarised Ru *sp* band Ref. [9]. By including a contribution from a Ru 5*s* relativistic Hartree-Fock calculation the χ^2 can be slightly improved. However, this inclusion of a 5*s* band is not physically meaningful as no 5*s* component is found in the band structure calculations. The discrepancies can instead be attributed to effects beyond the

Table 5.3: Occupation fraction in respective orbitals evaluated from the fitting analysis directions for Ru 4*d*, O 2*p* and Ru 5*s*. Shown with molecular orbital parameters from Ref. [9]. Orbital-wise decomposition from LMTO in Ru spheres and GAMESS analysis (in percentage of total Ru spin density)

		Ru 4*d*	(t_{2g}	e_g)	O 2*p*	Ru 5*s*
$Sr_3Ru_2O_7$						
	LMTO	0.81	(91 %	9 %)	0.18	-
	MO	0.70	(89 %	11 %)	0.30	-
$SrRuO_3$						
	MO	0.91	(91 %	9 %)	0.13	-0.04

	xy	yz	xz	$3z^2 - r^2$	$x^2 - y^2$
GAMESS	0.27	0.31	0.31	0.06	0.05
LMTO	0.26	0.32	0.34	0.05	0.04

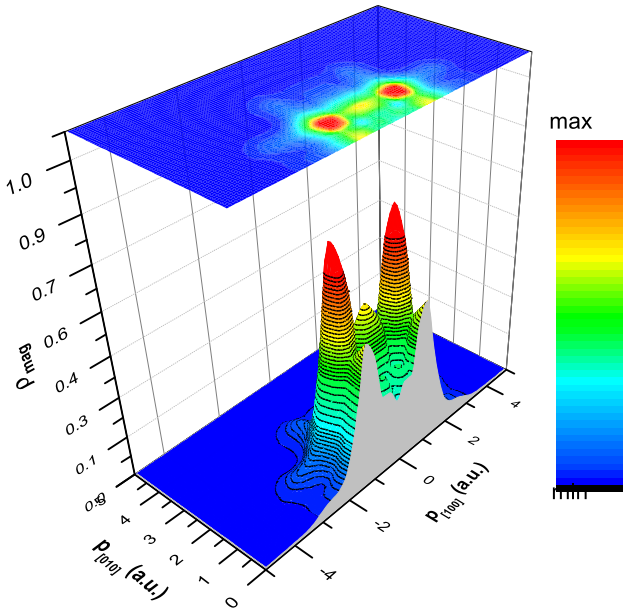

Figure 5.18: Two-dimensional spin density of $Sr_3Ru_2O_7$, reconstructed by fitting two crystallographic directions of experimental Compton profiles to refine our molecular orbital fitting scheme and projecting into the *ab*-plane.

Hartree-Fock method, as such, the method is not suitable for dealing with the low momentum part of the Compton profile. This failure has also been seen in a study on $Pr_{0.75}Ca_{0.25}MnO_3$ [8].

Turning our attention to the population analysis of the molecular orbitals, the spin density is almost entirely composed of t_{2g} derived states 89 (91) % for the GAMESS (LMTO) methods respectively, interestingly the molecular orbital calculation predicts a slightly higher e_g occupation necessary for the best fit. The preferential filling of the $3z^2 - r^2$ band can be attributed to the elongation of the [RuO_6] octehadra. This elongation also affects the occupation of the t_{2g} band with the yz and xz orbitals filling preferentially when compared with the xy band. This filling of not only the in-plane $4d_{xy}$ but also the out-of-plane $4d_{xz,yz}$ orbitals is vastly different to the superconducting cuprates, where the Fermi surface is derived from only the in-plane Cu $3d_{x^2-y^2}$ orbital.

In the molecular orbital method, the oxygen spin density as a percentage of the total spin density is estimated at $\sim$ 33 %. Using the Mulliken population analysis

method compared with $\sim$ 18 % in the oxygen LMTO spheres. This oxygen spin density is far higher than that derived in $SrRuO_3$. Both in good agreement with NMR estimates of 20 - 40 %

5.3.4 Conclusions

The spin density of the Ruddlesden-Popper ruthenate $Sr_3Ru_2O_7$ has been measured using spin polarised Compton scattering. The profiles were measured in the metamagnetic phase at 1.5 K along three crystallographic directions of a high-quality single crystal. LSDA band structure calculations and molecular orbital simulations reveal the extent of Ru 4*d* and oxygen 2*p* hybridisation and from which the occupation numbers of the t_{2g} and the e_g orbitals in the metamagnetic phase are determined. The system is almost completely (89 - 91 %) of t_{2g} Ru 4*d* character but with a non-negligible (9 - 11 %) e_g occupation similar to it's sister compound $SrRuO_3$. However unlike $SrRuO_3$ the oxygen spin density is estimated to be approximately 18 - 30 % of the total spin density in agreement with NMR results suggesting strong π-bonding between the Ru $4d_{xz,yz}$ and the O 2*p* orbitals. This strong oxygen hybridisation is in contrast to the superconducting cuprates. The excellent agreement of the LSDA calculations and published ARPES data allow us to identofy the Fermi surface sheets that take part in the metamagnetic transition. Furthermore, a spin moment of 0.70 $\pm$ 0.03 μ_B is shown in the *ab*-plane which, in comparison with SQUID data reveals a negligible orbital moment. This work highlights the benefits of perfoming magnetic Compton scattering experiments on high qulity single crystals, as unlike polycrystals the directional information is preserved, and simulatneous model fits can be fitted to multiple profiles.

Chapter 6

Spin and orbital magnetism in uranium superconductors

6.1 Introduction

The uranium class of superconductors has attracted much attention since the surprise discovery of ferromagnetism coexisting with superconductivity under pressure in UGe_2 [93]. The conventional concept of electron Cooper pairs of opposite **k** being mediated by an interaction with the lattice [94] is inappropriate for this class. The exchange interaction in a ferromagnet acts to align electron spins in a crystal, however, Cooper pair formation is most stable for *opposite* aligned electron pairs. It was for this reason that the phenomena of superconductivity and ferromagnetism were thought to be mutually exclusive.

One of the key factors determining the behaviour of actinides is the degree to which the uranium 5*f* electrons delocalise and hybridise with other atoms alloyed in the compound. There exists an empirical limit which governs the local/itinerant nature of the 5*f* electrons. This limit determined by the distance between neighbouring uranium atoms (d_{U-U}) is called the Hill limit and has a value of approximately 350 pm [95]. Compounds that bond below this limit tend to have overlapping electron wavefunctions

thus effectively delocalising the electrons. Compounds that bond above this limit tend to have their wavefunctions localise. Of interest to us here is the behaviour of the magnetism. For $d_{U-U} \leq 350$ pm the delocalised nature of the electron means that its orbital path is not well defined and the orbital moment is strongly reduced when compared with its free atom value. For $d_{U-U} \geq 350$ pm the electrons remain localised and do not form bands, this results in orbital moments that are close to the free atom value. The spin moment across this limit remains fairly constant, it is common for this reason for the value of μ_L/μ_S to be used as a measure of the degree of hybridisation of the $5f$ electrons with, not only neighbouring uranium atoms, but also transition metal ions also present in the material [96].

Another important feature of these compounds is the lack of consistent theory able to describe them. This is partially due to the ability of the uranium $5f$ electrons to possess both local and itinerant character. For the localised case, the LSDA is not an appropriate method to be used and it becomes necessary to include a U term into the Hamiltonian. This extra term accounts for the electrons interaction with its own potential. The delocalised case is easier and can be described well within the LSDA. There exists a greater problem for systems on the border of a quantum critical phase transition. The dynamic nature of the low energy spin fluctuations associated with the phase transition cannot be captured in the static LSDA. Substantial improvements are expected by using the dynamical mean-field theory (DMFT) approach [97], though this has not been applied to the uranium superconductors to the best of the authors knowledge.

6.2 Spin and orbital moments in UCoGe

The first compound of study in this chapter is UCoGe. The system demonstrates the coexistence of ferromagnetism (FM) and superconductivity (SC) at ambient pressure. It was discovered by Huy *et al.* to have a small ordered moment of $\sim 0.03\ \mu_B$ below its Curie point of 3 K which persists well in the superconducting regime below 0.8 K [98, 99]. The small ratio of the ordered moment to the effective moment, $m_0/p_{\text{eff}} \sim 0.1$, confirmed the itinerant nature of the ferromagnetic state ($p_{\text{eff}} \sim 1.7\ \mu_B$/U-atom). This led to the compound being classed as a weak itinerant ferromagnet. This small moment along with its magnetic sensitivity to doping and the much reduced value of the magnetic entropy ($S_{\text{mag}} = 0.04 \times R \ln 2$), reveal its proximity to a ferromagnetic quantum critical point (FMQCP) [100].

Despite the experimental discovery of weak and itinerant magnetism several theoretical studies have suggested that the system consists of a large orbital $5f$ moment

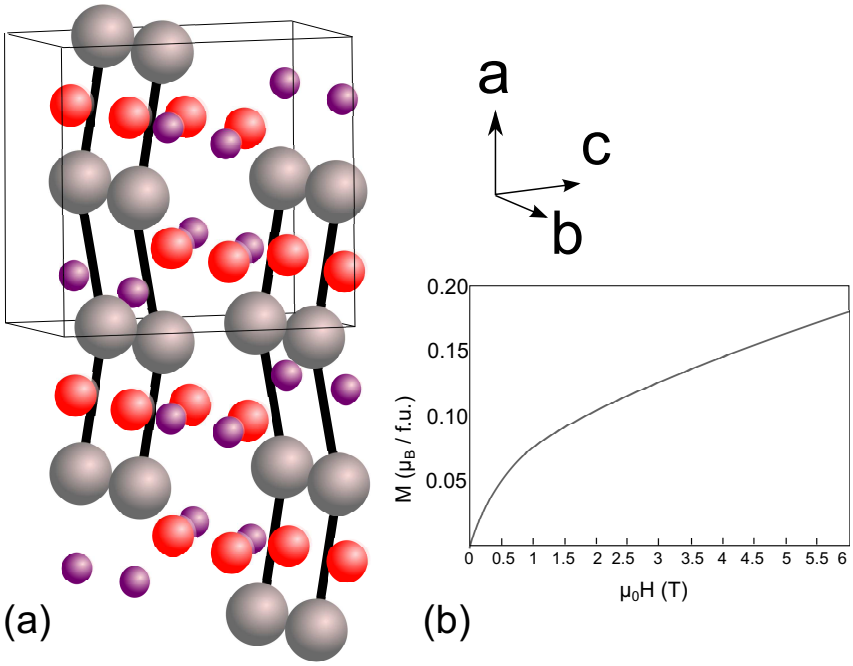

Figure 6.1: (a) Structure of UCoGe showing U-U zigzag chains, the U-U distance is 348 pm, on the border of itinerant and localised behaviour. Large atoms are uranium, red are cobalt and purple are germanium. (b) High field magnetisation of UCoGe.

opposed by a large spin moment (both $> 1\ \mu_B$), resulting in the near cancellation of the total moment [101, 102, 103], one of these papers also suggests that the uranium 5*f* moment is "fairly localised" in clear contraction to experimental studies. All studies predict there should be a significant cobalt spin moment with a quenched Co orbital moment, but calculate a much larger total moment than is experimentally measured. To explain this discrepancy with the magnetic moments Diviš suggested the cobalt moments are not collinear, giving rise to a smaller net moment, as observed in UNiAl [104], however, the degree of canting required would have to be $\sim 20^\circ$ to explain the magnetisation measurements and therefore seems unlikely to be the case. It is more likely that spin fluctuations from the systems proximity to a FMQCP reduce the moment and as such they are not captured by the static LSDA.

UCoGe belongs to the family of ternary compounds U*TX* compounds where *T* is a transition metal and *X* is a *p*-electron atom. UCoGe crystallises into the orthorhombic *Pnma* spacegroup. The uranium atoms arrange themselves in zig-zag chains along the *a*-axis shown in Fig. 6.1. Each uranium atom has only two uranium nearest neighbours at a distance of 348 pm, characteristic for the critical region between localised and itinerant 5*f*-electron behaviour (Hill limit) [95].

The quantity μ_L/μ_S has been used for many years to discuss itinerant / localised behaviour from polarised neutron scattering data [96]. It follows that the spin value of an electron is not much altered by its spatial extent, but the orbital value is greatly reduced as it becomes delocalised because the orbital path becomes less well-defined. The degree of 5*f* localisation depends on the overlap of 5*f* wavefunctions on neighbouring uranium atoms and on the hybridisation of 5*f* states with transition metal electrons. It has been suggested that the degree of U-*T* hybridisation could be small in UCoGe due to the possibility of filling up the cobalt 3*d* shell by transfer of electrons from the uranium, leading to a significantly increased localised behaviour for the uranium 5*f* electrons [105]. For the above reasons, an understanding of the role of cobalt in UCoGe is vital.

A polarised neutron diffraction (PND) experiment [106] was published recently

Table 6.1: Previous studies investigating the magnetic moments in UCoGe. The orbital moment on the Co is negligible, as well as any moment on Ge. (All values in μ_B/f.u.)

	Ref.	U_{Spin}	Co_{Spin}	U_{Orb}	Total	$-\mu_L^U/\mu_S^U$
PND	[106]	-0.05	-0.04	0.18	0.17	3.60
LSDA + U	[101]	-1.12	0.52	1.34	0.77	1.20
FAPW + FPLO	[102]	-1.2	0.25	1.1	0.1 - 0.3	0.92
LSDA	[103]	-1.08	0.23	1.22	0.47	1.13
LSDA + OPC	[103]	-1.25	0.30	2.67	1.95	2.14
SPR-KKR	This work	-0.96	0.25	1.21	0.55	1.26

in an attempt to reconcile the discrepancies between theory and the observed electronic behaviour. The measurement at low field (3 T) suggested that there is a little contribution from the cobalt (-0.04 μ_B) and this contribution is parallel to the uranium spin moment, at odds with all the published theory. Most of the moment is associated with the uranium orbital moment, 0.18 μ_B. However, much of the moment at these fields appeared not to be associated with any particular site, this intistital moment was 0.08 μ_B, almost as big as the uranium and cobalt moments added together. The previous theoretical and experimental investigations are summarised in Table. 6.1. The purpose of this part of the chapter is:

1. to determine the orientation of the magnetic moments.
2. to clarify the sizes of these magnetic contributions in the normal phase which are often non-trivial in 5*f* electron systems [2] which will determine whether the small observed total moment is indeed a result of large canceling spin and orbital moments.
3. to determine the role of the cobalt 3*d* electrons.
4. to investigate the itinerancy of the uranium moment

6.2.1 Sample characterisation

As both of the samples studied in this chapter contain depleted uranium, crystals were prepared and characterised in facilities that specialise in handling radioactive samples. The UCoGe single crystal was grown at Los Alamos National Lab, USA by Dr. Eric Bauer. A 1.09 g single crystal was grown from zone refined ingots. Magnetic measurements for that sample were taken with a Quantum Design SQUID by Dr. Jon Taylor at a base temperature of 1.8 K at the ISIS facility, UK. The data show an effective moment at zero-field of 0.06 $\pm$ 0.01 μ_B and in 5 T of 0.16 $\pm$ 0.01 μ_B. The discrepancy between our sample and those used in other works [107, 108, 98] can be attributed to the effect of annealing as magnetic properties are known to vary largely as a result of this process [109]. Sample alignment was performed on a Laue set at the ESRF on ID20. Ultra-low temperature (down to 0.1 K) ac-susceptibility measurements Ref. [99] on this sample were made confirming the bulk superconducting behaviour ($T \sim 0.8$ K) coexisting with ferromagnetism and estimates the critical field, H_{C_2}, to be in good agreement with Ref. [110], although that study was performed on a polycrystal.

6.2.2 X-ray magnetic circular dichroism

A very important, yet unresolved, issue concerning UCoGe is the orientation of the moments. All band structure calculations performed agree that the uranium spin moment is anti-aligned to the total moment - the rest being composed of a large uranium orbital moment and cobalt spin moment. In all cases the cobalt orbital moment is assumed to be quenched. This however is at odds with PND measurements which measures both uranium and a cobalt spin moments to oppose the total moment. A very useful tool in the separation of magnetic moments is the element specific technique of X-ray magnetic circular dichroism (XMCD). The aim is to directly probe the cobalt $L_{2,3}$ ($2p \rightarrow 3d$) edges thereby investigate the orientation of the cobalt $3d$ moment. A similar investigation on the $N_{4,5}$ ($4d \rightarrow 5f$) edges of the uranium states could also be addressed to study the uranium $5f$ moment. The possible transitions are shown in Fig. 6.2 (a).

The technique of XMCD (introduced in §4.4.1) uses the imbalance of spins at the Fermi level to give information on the electronic and the magnetic structure of a system. Using light of varying (positive and negative) helicity, one can measure the dichroism induced by the spin imbalance. Quantitative information can be gained by applying the magneto-optical sum rules. Whilst these rules work well for early transition metals, the non-negligible T_z component in our non-cubic system and the *jj*-mixing of $4d^{5/2}$ and $4d^{7/2}$ core states means that the analysis is less trivial.

X-ray absorption and XMCD spectra were measured on beamline I06 at Diamond Light Source, RAL, Oxford. The vector superconducting magnet on the I06 branchline has the capability of providing a sample temperature down to 1.3 K and can apply a field in any arbitrary direction with a maximum of 6 T along the direction of the beam and 4 T perpendicular. The branchline is fed by an APPLE II undulator whose useful energy range (i.e. that light which is circularly polarised) is between 106 - 1300 eV. Energy tuning was achieved using a plane grazing monochromator. Spectra were recorded in both total electron yield (TEY) and fluorescence yield (FY). TEY mode is more surface sensitive, with the depth sensitivity given by the escape depth of electrons (20 - 200 Å). However, for the purpose of measuring a *bulk* signal only measurements from the FY mode were used. FY has a depth sensitivity given by the penetration depth of the incident and emitted photon (of the order 1000 Å in the soft X-ray regime).

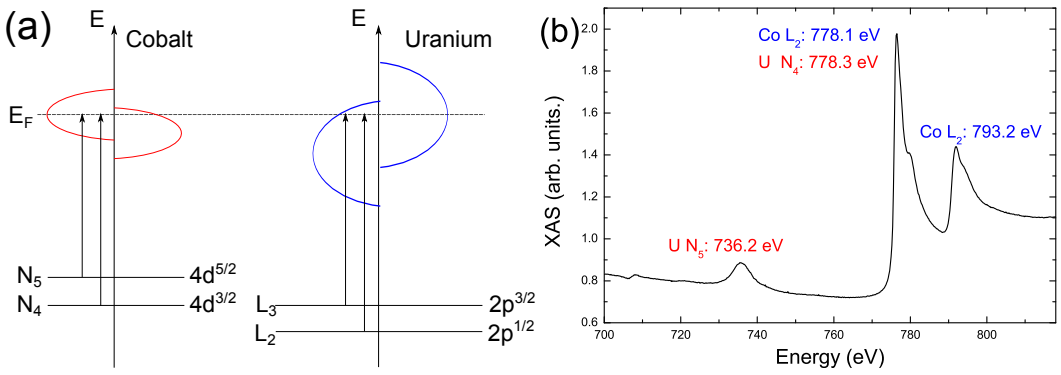

Figure 6.2: (a) Core state energy levels of the probed transitions of cobalt and uranium and (b) a large range energy scan XAS of UCoGe at 1.5 K in zero field.

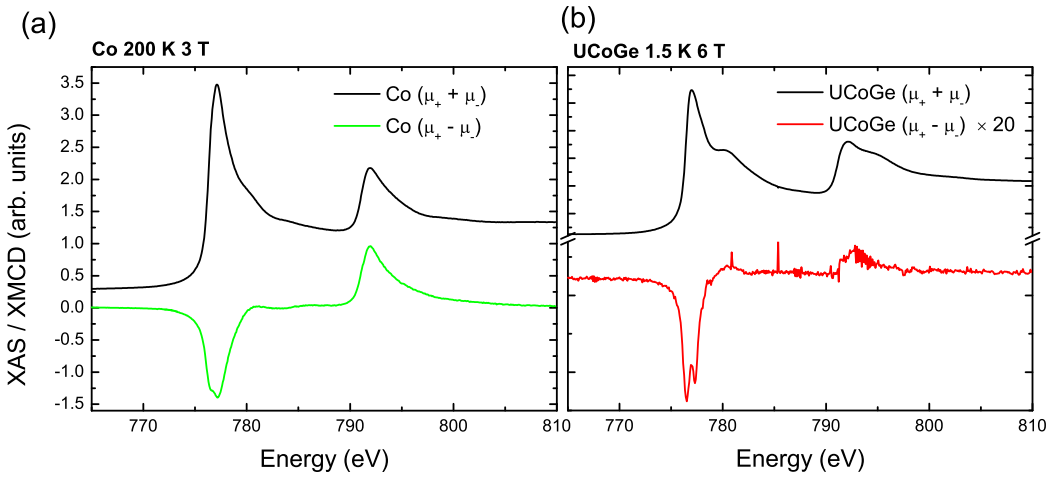

Figure 6.3: XAS and XMCD of (a) hcp Co at 200 K and 3 T and (b) UCoGe at 1.5 K at 6 T showing the same orientation of moments i.e. both aligned with the field. Also visible is structure in the UCoGe L_3 data not present in the pure Co.

One complication of this approach is in the positions of the cobalt L_3 and the uranium N_4 edge, which overlap strongly - in fact the difference in binding energy is only 0.2 eV, shown in Fig. 6.2 (b). However, the distinct uranium N_5 peak could be resolved. This peak was shown to be much smaller than the cobalt L-edges and suggested that the uranium N_4 peak would not influence our cobalt data significantly.

XA and XMCD spectra for pure cobalt and UCoGe are shown in Fig. 6.3 measured at 200 K, 3 T and 1.5 K and 6 T respectively. XAS comparison with reference data for Co^{3+} ($EuCoO_3$) and Co^{2+} (CoO) showed the valence state to be Co^{3+} [61]. At all temperatures within the ferromagnet (FM) regime dichroism at the Co L_3 edge was observed. This was confirmed by a temperature dependence study where dichroism could not be found at temperatures higher than T_C (3 K) and a field dependence study where the peak of dichroism was shown to increase with the applied magnetic field, shown in Fig. 6.4 (a).

Dichroism at the uranium N-edge was unfortunately not observed, shown in Fig. 6.4 (b). This could be for a variety of reasons. The size of the uranium dichroism, with reference to Ref. [111], in UFe_2 is very small compared with the iron dichroism -

this could put the magnetic signal well below the level of sensitivity of the experiment. It may also be important to note that the dichroism from the *N*-edge may be an order of magnitude smaller than that from the hard X-ray dichroism expected from *M*-edge transitions [112]. It may in future prove highly informative to repeat the experiment in the hard X-ray regime.

Given the decent quality of the dichroism, tentative estimates of the moments involved can be deduced. It was assumed that the uranium *N*-edge dichroism is negligibly small. Applying the sum-rules (described in §4.4.1) to the cobalt edges would gives μ_S as 0.05 μ_B and μ_L as 0.0004 μ_B. However, as mentioned before due to the various approximations in the sum rules which may not be valid here and also the presence of a uranium peak the size of these numbers is questionable.

However, important information can be gained when comparing the orientations with those determined by the PND experiment. The PND measures the spin of uranium and cobalt to be aligned, contrary to every band structure calculation. Using a standard cobalt reference it is shown that the cobalt spin moment in UCoGe aligns with the field as the dichroism is the same sign for cobalt where it is assumed the cobalt moment aligns with the field. This test shows that the orientation of the moments obtained by PND is inconsistent with that measured by XMCD.

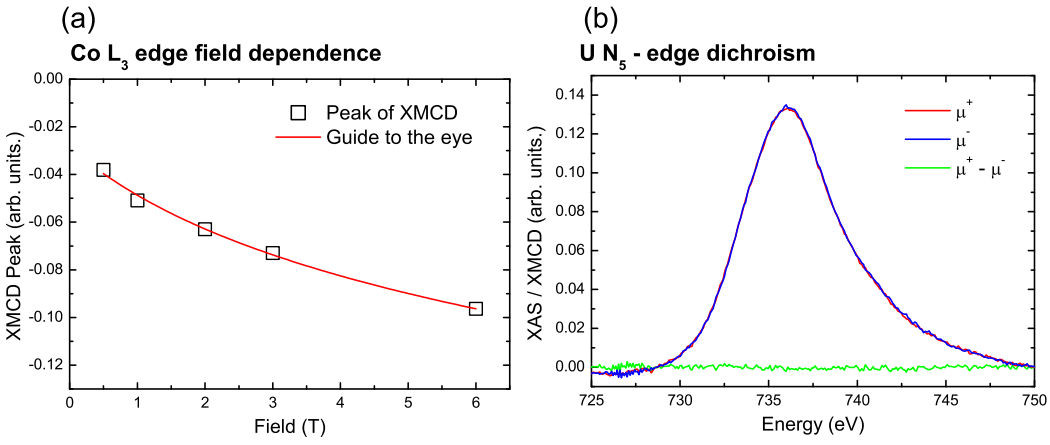

Figure 6.4: (a) Field dependence of the XMCD at L_3 edge and (b) XMCD at the N_4 peak, both in an applied field of 6 T and at 1.7 K.

6.2.3 Band structure calculation

The electronic structure of the UCoGe was calculated self-consistently using the SPR-KKR method in the ASA, the ground state was calculated fully relativistically and the potential was converged to a tolerance of 0.001 Ryd. Using this scheme the moments obtained are -0.97 μ_B of spin per uranium site, 0.25 μ_B per cobalt site and a negligible contribution from the germanium. The orbital moments are 1.22 μ_B on the uranium site and 0.05 μ_B on the cobalt sites, in good agreement with the LSDA calculations performed by other authors in Table. 6.1. The discrepancy of the numbers could be attributed to the limitations of the ASA as much of the moment is expected to be itinerant.

The general features of our calculations are a large uranium spin moment opposed by a larger uranium orbital moment. The uranium spin moment is opposed by a non-

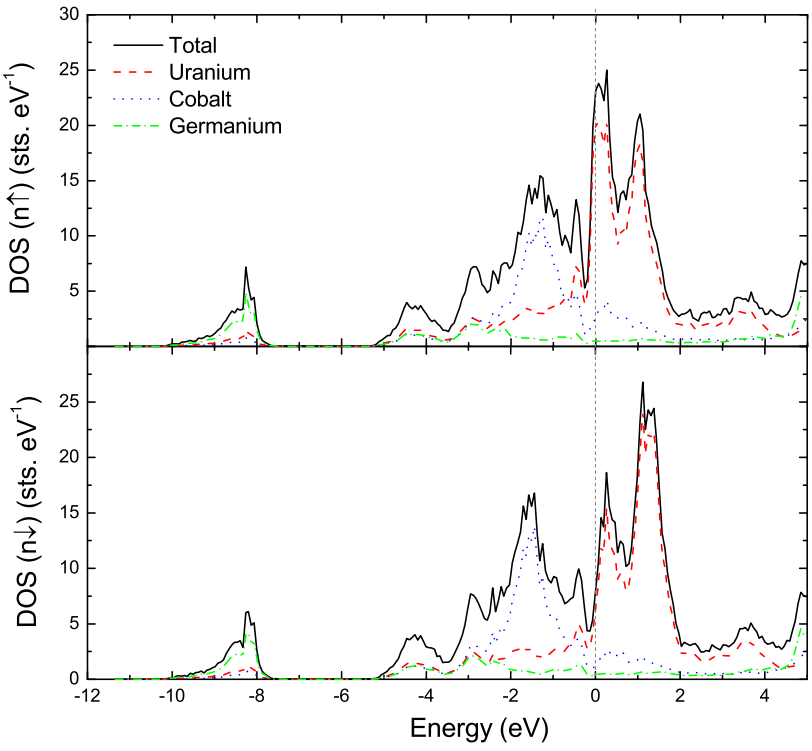

Figure 6.5: Calculated partial densities of state for UCoGe in the ferromagnetic state showing similar behaviour as that of Refs. [101, 102, 103]. The dashed grey line represents Fermi level.

negligible cobalt spin moment, resulting in the uranium moment being aligned opposite to the total moment. The density of states and magnetic Compton profile, $\rho^{\uparrow}(\mathbf{p}) - \rho^{\downarrow}(\mathbf{p})$ for UCoGe calculated from the self-consistent potentials and are shown in Fig. 6.5 and Fig. 6.6 respectively.

All the calculations significantly overestimate the magnetic moments. This is perhaps due to the neglect of spin fluctuations in the calculations [113]. However, it is assumed that the *shape* of the momentum density distributions remains unchanged and it is the *area* that is affected, thus the analysis continues using the shapes of the profiles[1].

6.2.4 Momentum distribution and size of the moments

The spin polarised Compton profiles were measured on beamline ID15A at the ESRF. The measurements were made in an applied magnetic field of $\pm$ 5 T, at 1.5 K. The data were corrected for energy dependent detector efficiency, sample absorption, and the relativistic scattering cross section. An incident energy of 90 keV was used to keep below the K-edge of uranium and avoid flooding the detector with fluorescence. The MCP measured at ID15A is shown in Fig. 6.6, also plotted are the profiles from KKR calculations, renormalised so that the total spin moment has the same area as the measured Compton profile.

The shape of the profile can sometimes result in the individual momentum densities being distinguishable, see §3.2.2, however, the electron momentum distribution of U 5f and Co 3d are essentially (within our error) indistinguishable so cannot be done in this case. Instead, the moments on the other sites has been approximated by comparing the experimental moments with moments predicted by published full potential calculations Ref. [103]. Using this combined method, and the knowledge gained from the XMCD moments summarised in Table. 6.2 are obtained.

[1] The assumption that the exchange splitting is reduced equally across all sites is based with reference to Haynes *et al.* where an investigation into the spin density in the quantum critical $NbFe_2$ was undertaken [114].

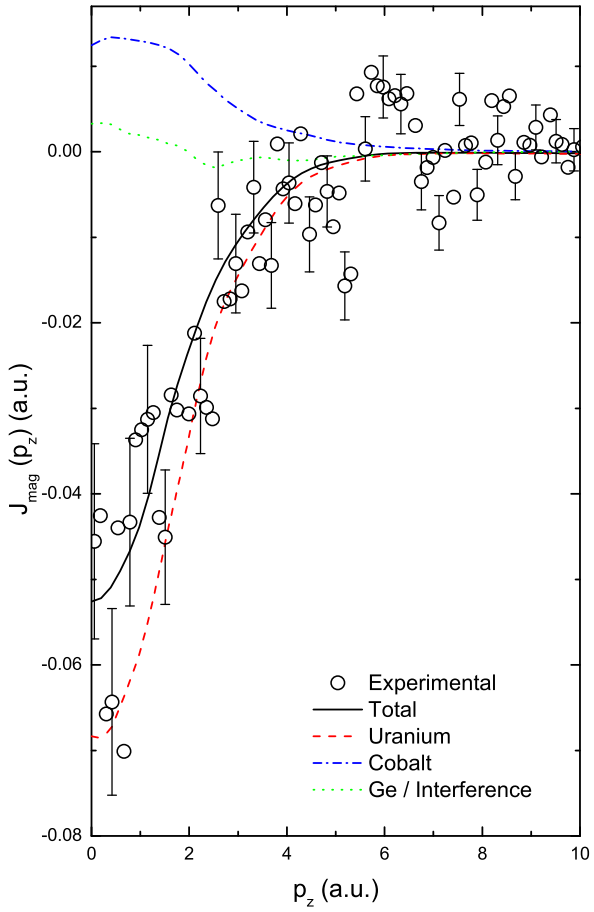

Figure 6.6: Magnetic Compton profile of UCoGe along the *c*-axis, shown with spin density predicted by KKR calculations normalised to the spin moment of -0.22 $\pm$ 0.05 μ_B and de-constructed into the site projected profiles.

From the magnetic Compton scattering data a total spin moment of -0.22 $\pm$ 0.05 μ_B is shown with an opposing orbital moment of 0.38 $\pm$ 0.05 μ_B. When compared with full-potential augmented plane wave calculations from Ref. [103], it can be inferred that UCoGe consists of a uranium spin moment of -0.30 $\pm$ 0.05 μ_B and a larger orbital moment of 0.38 $\pm$ 0.05 μ_B resulting in the spin moment being aligned opposite to the total moment.

Focusing on the uranium moments, the small value of μ_l/μ_s (1.04) suggests a strongly itinerant nature of the 5*f* electrons. This low value, when compared with the free atom value, suggests strong 5*f*-5*f* overlap and strong 5*f*-3*d* hybridisation. It is also

Table 6.2: Scaled moments for UCoGe, using band structure calculation from Ref. [103]) adapted to model our results. Starting from the value of the measured total spin moment with a value of -0.22 μ_B and an orbital moment of 0.38 μ_B and assuming a negligible orbital moment on the cobalt as inferred from XMCD. (All values in μ_B/(f.u)).

	U_{spin}	Co_{spin}	U_{orb}	U_{Tot}	$UCoGe_{Tot}$
FP LSDA	-1.10	0.23	1.22	-0.12	0.47
Rescaled	-0.30	0.06	**0.38**	-0.08	0.17

shown that the cobalt spin moment is of moderately magnitude 0.06 $\pm$ 0.05 μ_B induced by strong hybridisation with the uranium and suggesting that the cobalt orbitals play a significant role in the delocalisation of the uranium electrons.

The conclusions drawn by polarised neutron diffraction at 3 T are now addressed. Prokeš *et al.* suggest that there is a very small cobalt moment anti-aligned with the field, it is shown here that it aligns with the field and it moderately large. The large value of their μ_l/μ_S ($\sim$ 3.6) is indicative of a strongly localised uranium 5*f* orbital in contradiction with other theoretical and transport data.

6.2.5 Conclusions

Unlike theoretical predictions the small total moment in UCoGe is not composed of large opposing orbital and spin moments, but instead consists of opposing, fairly weak spin and orbital moments. The magnitude of the individual moments are indicative of a strongly delocalised electron system, with the delocalisation mechanism being a strong overlap between uranium 5*f* and cobalt 3*d* electrons which consequently result in a non negligible cobalt moment. By means of XMCD experiments the alignment of the moments are determined in agreement with LSDA calculations, but in contrast with PND measurements.

Due to the cancellation of the uranium spin and orbital moment, the majority of the total moment comes from the cobalt 3*d* electrons. However, the majority of the spin moment comes from the uranium 5*f* electrons.

The work detailed in this chapter presents detailed studies of two magnetic X-ray methods used to comprehensively unveil the magnetic structure of this novel compound. The understanding of the magnetic structure is vital for understanding the behaviour of these fascinating materials.

We highlight the vital importance of making experimental determination of the individual spin and orbital contributions of **S** and **L** rather than just the total moment, and as such these measurements provide a more rigorous test of theoretical calculations. We also highlight how a combination of different methods can be used together to provide a more complete picture of the magnetic structure of a material.

6.3 Temperature dependence of the spin moment in UGe_2

The first ferromagnetic superconductor in the uranium series to be discovered was UGe_2 [93] under the application of a pressure of $\sim$ 1 GPa. The phase diagram (Fig. 6.7) shows superconductivity coexisting with FM in a small range around 1 GPa and at low temperatures. The superconducting dome is intersected by a first order phase transition. This phase transition is between a weakly polarised (WP) FM state and a strongly polarised (SP) FM state. It is reached via a metamagnetic transition at a critical temperature (T^*) within the ferromagnetic phase ($\leq$ 60 K) which can be observed in hysteresis loops clearly below $\sim$ 1 K, see Ref. [115].

The nature of this phase transition has prompted much research into it's origin. It has been suggested that a sharp band moving across the Fermi level is responsible

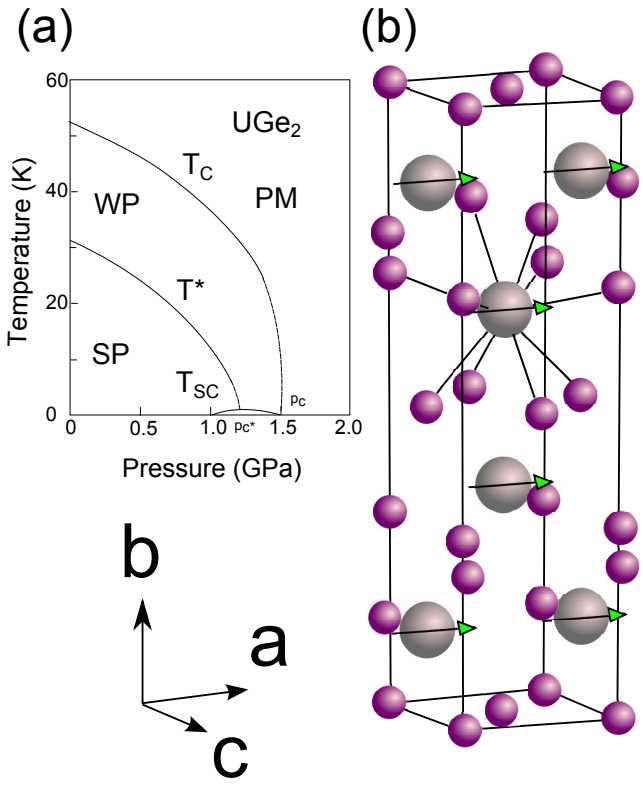

Figure 6.7: (a) Pressure - temperature phase diagram of UGe_2, taken from Ref. [116] (b) Structure of UGe_2. Grey atoms are uranium and purple atoms are germanium. The green arrow indicates the direction of spontaneous moment.

for this behaviour [116]. LSDA + U calculations found two nearly degenerate solutions which differ very slightly in terms of the orbital moment. The nature of the transition at T^* could be due to fluctuations between these two polarised states, Ref. [117]. The phase transition at T^* has also been ascribed to a CDW/SDW formation, although no evidence of long-range order has been found to confirm this by neutron scattering [118]. The interaction of this phase transition and the superconducting region suggests a link between the two phenomena. Clearly a firm understanding of the electronic structure through the WP $\rightarrow$ SP transition is desirable.

In terms of the magnetism, as previously mentioned in §6, the properties of the 5*f* electrons struggle to be explained on a general footing. For UGe_2, the standard LSDA predicts a total moment of $\approx$ 0.25 μ_B, this compares very badly with the $\approx$ 1.4 μ_B shown by bulk magnetisation methods. This was ascribed to an inadequate treatment of correlation effects governed by the presumably localised nature of the 5*f* electrons [117]. UGe_2 bonds below the Hill limit, localising the 5*f* electrons. With the inclusion of the LSDA + U term, the total moment is found to be in accordance with magnetisation measurements for the *total* magnetic moment, but the calculated spin moment 1.52 μ_B is somewhat at odds with previously performed magnetic Compton scattering measurements [119] which measures a saturated spin moment of 1.15 $\pm$ 0.05 μ_B along the *a*-axis. For this novel system, accurate measurements of the constituent values of the spin and orbital moments are desirable if the complex electronic structure is to be fully understood.

In the previous magnetic Compton scattering study, the spin-polarised electron momentum density of UGe_2 was fitted successfully with free-atom wavefunctions to estimate the spin density in each 5*f* orbital [119]. The effect of Ge magnetism was expected to be negligible as the contribution has been shown to be less than 1 % from DFT and XMCD [121, 122]. The purpose of this section is:

1. to investigate the temperature dependence of magnetisation from a spin and orbital point of view

Table 6.3: Results from previous investigations into the magnetic state of UGe_2. All moments are in Bohr magnetons. PND, LSDA + U and XMCD quote values only for the uranium ion.

		Ref	U_{Tot}	U_{Spin}	U_{Orb}	$-\mu_L^U/\mu_S^U$
PND		[120]				
	U^{4+}		1.46	-0.91	2.37	2.60
	U^{3+}		1.45	-1.17	2.62	2.24
LSDA		[121]	0.27	-1.57	1.848	1.17
LSDA + U		[121]	1.46	-1.52	2.98	1.96
XMCD		[122]				
	U^{3+}		1.41	-0.94	2.35	2.51
	U^{4+}		1.41	-0.48	1.89	3.94
MCS						
		[119]	1.90	-1.15	3.05	2.65
		This work	1.46	-0.98	2.42	2.47

2. to investigate the spin-polarised momentum density across the transition to address any change in the orbital configuration of UGe_2.

6.3.1 Sample characterisation

UGe_2 samples were grown at Edinburgh University by Dr. Dmitry Sokolov using the Czochralski technique under a protective atmosphere of purified Ar to suppress the vapour pressure of Ge [123]. The samples have previously been used in neutron scattering studies to investigate the lattice expansion under pressure, Ref. [124]. Temperature dependent magnetisation measurements in a field of 1 T from 2 K up to 100 K confirmed that it had an easy axis along the *a*-direction in agreement with Ref. [125] and is shown in Fig. 6.9. This is in contrast with UCoGe, where the spontaneous moment is confined to the *c*-axis. Fig. 6.9 shows an ordered moment at zero field of 1.48 μ_B.

6.3.2 Magnetic Compton scattering method and results

The spin polarised Compton profiles were measured on beamline ID15A at the ESRF. An incident radiation flux of 90 keV was used to avoid the problem of fluorescence counts dominating the spectra. As the magnetisation of UGe_2 is soft along the *a*-axis, the measurements were made in an applied magnetic field of $\pm$ 1 T, at 10, 30, 40, 50 and 60 K. The field was reversed every 5 minutes in order to measure the difference profile. The data were corrected for energy dependent detector efficiency, sample absorption, and the relativistic scattering cross section. Temperature dependent momentum distributions and magnetic moments are shown in Figs. 6.8 and 6.9 respectively.

Values of the spin and orbital moments for the lowest temperature are shown in Table. 6.3, higher temperatures are shown in Fig. 6.9. Whilst seemingly consistent with the observed total moment, the values of the spin and orbital moments from LSDA + U calculations of Ref. [121] are not consistent with those measured here. A spin moment (at our lowest temperature) of -0.98 $\pm$ 0.05 μ_B is shown, this compares with a spin moment of 1.52 μ_B from the calculations. It may be instructive to perform some optimisation of the *U* and *J* parameters with a fixed spin calculation, using the spin value obtain here, to get a more accurate description of the electronic structure as performed in the $Ca_3Co_2O_6$.

The value -μ_L^U/μ_S^U introduced earlier, can also help to draw conclusion on the localisation state of the uranium electrons in UGe_2. The value of 2.47 obtained from magnetic Compton scattering is over twice as large as that of UCoGe. This suggests a far more localised electronic state, which is expected for this material.

6.3.3 Molecular orbital calculations

The analysis of the magnetic Compton profiles uses the GAMESS quantum chemistry code. A free uranium atom was expanded using a double-zeta valence (DZV) basis set in which 78 electrons were removed and replaced by ECP. The resulting wavefunctions are then transformed into Compton profiles in a manner described in §2.2.1.3. The

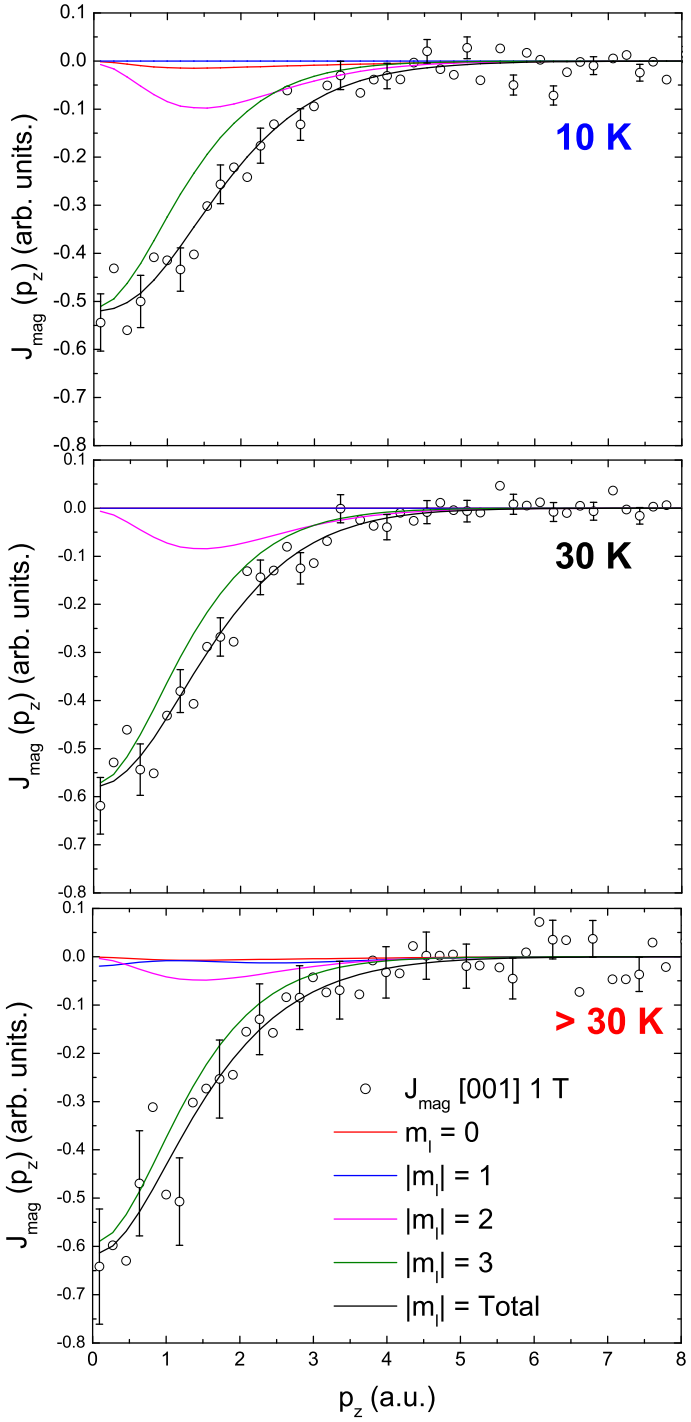

Figure 6.8: Temperature dependent magnetic Compton profiles at 1 T for T = 10 K, 30 K and averaged data for 30, 40, 50 and 60 K for UGe_2 deconstructed using uranium molecular orbital calculations.

profiles have a similar distribution to those reported by Sakurai *et al.* [119], who used tabulated data for the radial and angular distributions of the orbitals.

Due to fact the magnetic Compton profile is a twice projected quantity the distribution along the *a*-axis, for the $m_L = 1$ and -1 orbitals are the same, as are 2 and -2 orbitals *etc*. Thus there are four fitting parameters: $m_L = 0$, $|m_L| = 1$, $|m_L| = 2$ and $|m_L| = 3$. Fig. 6.8 shows these four orbitals fitted to the temperature dependent magnetic Compton profiles. The profiles have been normalised to unity for ease of comparison although in reality they have the areas shown by the spin moments in Fig. 6.9.

With increasing temperature it is apparent there is a narrowing of the normalised profile. This narrowing is indicative of a redistribution of the moment into a more itinerant orbital of perhaps $|m_L| = 3$ character, such a change in the occupied states across T^* has been suggested as a possible mechanism for the T^* transition and thus the mediation of the superconductivity.

Orbital moments obtained by the weighting coefficients multiplied by the angular momentum character are also plotted in Fig. 6.9. These estimates for the orbital moments show far better agreement than those of Sakurai *et al.*, who obtain an orbital moment of 2.92 μ_B - far larger than that which is measured.

6.3.4 Conclusions

A magnetic Compton scattering experiment was performed on UGe_2 to investigate the temperature dependence of the spin and orbital moments as well as the spin-polarised momentum density distribution across the T^* transition. Crucial to the understanding of UGe_2 is what happens to the bandstructure at T^*, where the system changes from a weakly polarised (WP) to a strongly polarised (SP) state. The critical temperature reduces with pressure where it forms into a superconducting region, this leads to the assumption that the WP $\rightarrow$ SP transition plays a role in the superconductivity. The aim of the investigation was to observe any redistribution of the electronic occupation

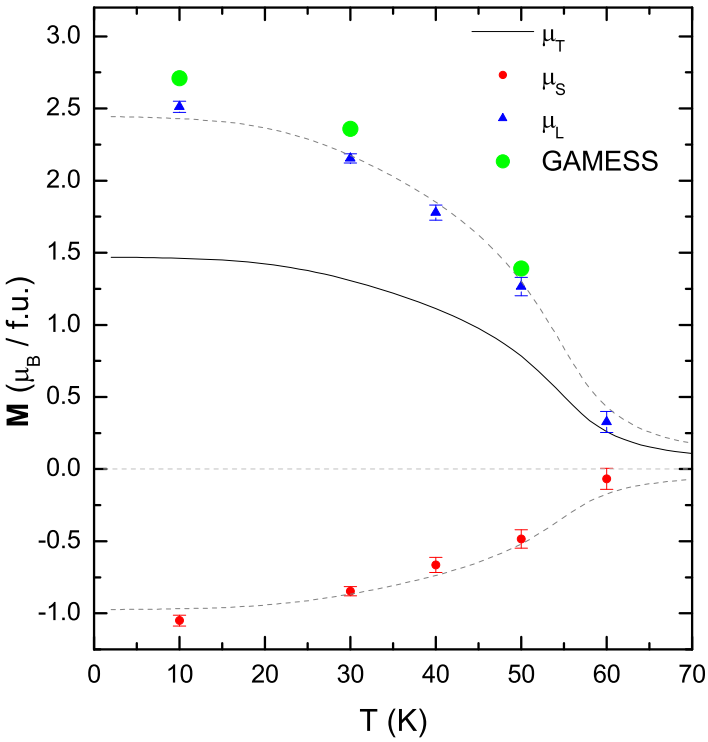

Figure 6.9: Temperature dependence of magnetisation for UGe_2 measured in the weakly-polarised (WP), strongly polarised (SP) and the paramagnetic (PM) phases. Showing magnetic Compton derived spin moments and bulk moments from the SQUID. Also shown in green are the orbital moments derived from GAMESS fitting the profiles to experimental data

associated with the phase transition. It had been suggested that a dramatic change in the Fermi surface could be responsible.

With the aid of molecular orbital calculations, it has been found that the magnetic electron momentum distribution narrows as the temperature is increased. Such a shape change is consistent with a Fermi surface driven superconducting region. More work is needed on improving the statistics at ambient pressure and also extending the investigation into the high-pressure regime.

6.4 Conclusions

In the previous chapter magnetic X-ray experiments on two uranium superconductors are detailed with an aim to better understand their magnetic properties with relation to their electronic properties.

The current understanding is based on agreement of the *total* moment with that predicted by the LSDA or the LSDA + U formalism. This is not enough - vast differences between the spin and orbital moments measured and those predicted by band structure calculations exist in UCoGe, UGe_2 and URhGe.[2]

As well as being fundamental properties of the magnetism of a system, μ_S and μ_L can be used to comment on the localisation of the magnetic electrons. Presented in Table. 6.4 are the constituent values of the moments and the ratio -μ_L^U/μ_S^U for the uranium compounds studied in this thesis. This value can be used to comment on the localisation. The more localised an electron the better defined it's orbital path therefore it possesses a higher -μ_L^U/μ_S^U ratio. Conversely, a low value of -μ_L^U/μ_S^U indicates the electron is more itinerant in character. A brief summary of the spin and orbital moments and the -μ_L^U/μ_S^U value for the systems studied here are present in Table. 6.4.

More work is needed in the case of UCoGe. A clear consensus between any two techniques is yet to be reached. The LSDA is doomed from the start with the lack of consideration of dynamic effects known to re-normalise the size of the moments. A method here of measuring the electron momentum distribution and fitting the magnitudes with the LSDA predictions can associate site specific magnetisation densities. The very low value of -μ_L^U/μ_S^U indicates that the system is strongly itinerant. Given the reasonably large cobalt moment, it can be inferred that the cobalt helps delocalise the uranium 5*f* electrons through hybridisation. Using XMCD, the cobalt moment is shown to be oppositely aligned to the total spin moment - in contradiction with PND work but

[2] There exists a slight mystery with URhGe (not presented in this thesis). Far smaller moments than expected from LSDA calculations are shown although seemingly in accord with PND experiments. The mystery is that the measured Compton profile does not have the expected uranium 5*f* line shape. More work is needed on this system.

consistent with theoretical work.

For UGe_2 the agreement is good for all components of the magnetisation. This is expected in the LSDA + U as the electron is localised by the large d_{U-U} distance. The large -μ_L^U/μ_S^U value verifies that the system is largely localised. An interesting experiment would be to look at the spin and orbital components of the magnetisation as d_{U-U} is shortened, i.e. under pressure - such an experiment is currently feasible. The high pressure experiment would use the diamond anvil cell belonging to the Warwick group and the X-ray beam would pass in and out of the transparent diamond having scattered from the sample held in between a CuBe gasket. With reference to the temperature dependence of the magnetisation performed here, a small redistribution of the orbital occupation was observed on moving across T^*. Such an observation could be evidence for an orbital redistribution which could be related to the superconducting properties.

Table 6.4: Comparison of Compton and theoretical moments for UCoGe and UGe_2. All values are in μ_B / f.u..

		Ref	U_{Tot}	U_{Spin}	Co_{Spin}	U_{Orb}	Total	$-\mu_L^U/\mu_S^U$
UCoGe								
	MCS	This work	-0.08	-0.30	0.06	0.38	0.17	1.04
	PND	[106]	0.1	-0.05	-0.04	0.2	0.17	3.60
	LSDA	[103]	0.14	-1.10	0.23	1.22	0.47	1.1
UGe_2								
	MCS	This work	1.46	-0.98	-	2.42	1.46	2.47
	PND	[126]	1.45	-1.17	-	2.62	1.45	2.24
	LSDA + U	[121]	1.46	-1.52	-	2.98	1.46	1.96

Chapter 7

High temperature magnetic Compton scattering

7.1 Introduction

The understanding of magnetic materials at finite temperatures is an elusive goal for theoreticians and experimentalists alike. Whilst band-structure predictions for transition metals give qualitatively good agreement of the electronic ground state, the agreement at temperatures greater than 0 K is still a challenge. There is considerable difficulty in accounting for temperature effects and specifically in making accurate predictions of a materials Curie temperature.

It is known that magnons and thermal vibrations with energy k_BT compete with exchange interaction energies to destroy magnetic order in itinerant ferromagnets such as nickel at temperatures consistent with the observed Curie temperature. The dynamic thermal behaviour and the possibility of emergent phenomena such as local moment formation is often overlooked in conventional band-structure techniques. The technical difficulties of high-temperature techniques mean that high quality data is rare. As such, the need for experimental data at high temperatures to refine our understanding of finite temperature magnetism is clear.

Detailed here are two examples of how the magnetic Compton scattering technique can be used to shed light on the magnetic behaviour of materials at high temperatures. The chapter first details work on a range of Invar alloys, $Fe_{1-x}Ni_x$, as a function of temperature and composition, the aim of which is to attempt to observe any redistribution of the magnetic electrons which has been, as of yet, unseen. Any such redistribution of the magnetic electrons could be related to the observed magneto-elastic properties. Secondly, the spin-polarised momentum distribution of pure single crystal nickel is investigated in it's ferromagnetic regime and then at T_C. There is considerable disagreement between techniques concerning the size of the itinerant part of the moment across the transition. The aim is to resolve these inconsistencies.

7.2 $Fe_{1-x}Ni_x$ alloy

The Invar effect in metal alloys has been studied extensively since its discovery over 100 years ago [127]. The observation that the thermal expansion coefficient, α, almost vanishes across a large temperature range is well documented (Fig. 7.1) and has subsequently been used in technologies which utilise this lack of expansion, yet the mechanism by which it occurs is yet to be satisfactorily determined. The phenomena has been identified in many materials, for example, alloys of iron and nickel (as studied here) [127], alloys of iron and platinum [128] and $SrRuO_3$ [129]. It was recognised early that in addition to the well-known positive contribution to α from the thermal motion of atoms, there also exists a negative contribution to α that is magnetic in origin. This magnetic origin was inferred from the the correlation of the Invar effect and the Curie point, this can be seen in the lower part of Fig. 7.1, where the magnetic contribution (α_{M}) to the thermal expansion reduces to zero at the Curie point.

In 1963, Weiss proposed a simple two-band model to explain the observed effect [130]. This model relies on two nearly degenerate magnetic states: a high-spin (high-volume) state and a low-spin (low-volume) state as shown in Fig. 7.1 (b). With

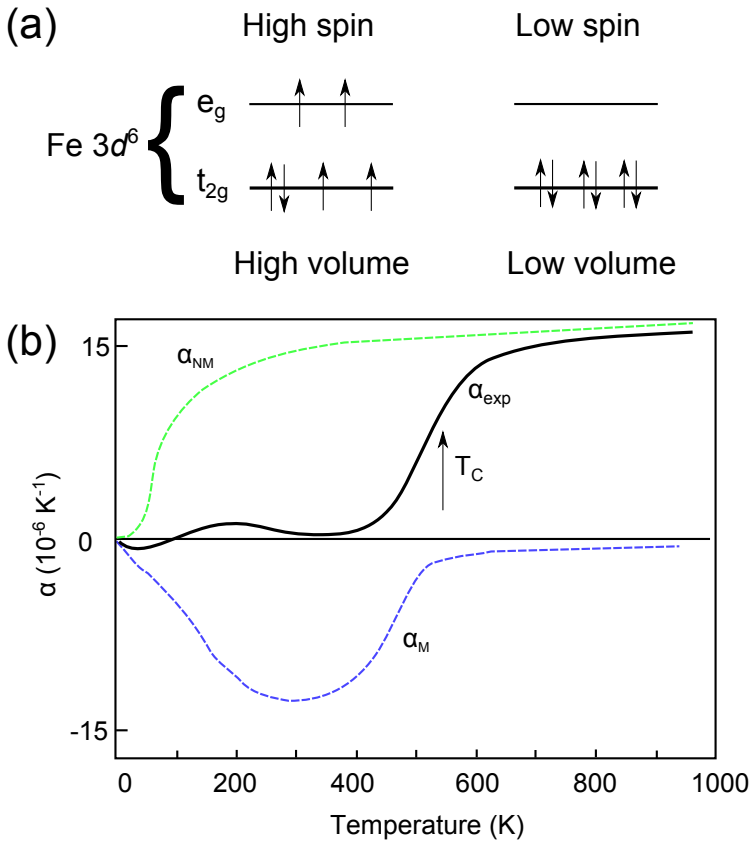

Figure 7.1: (a) Energy levels of low spin and high spin states for Fe $3d^6$ ion. (b) Linear expansion coefficient as a function of temperature of $Fe_{0.65}Ni_{0.35}$ showing the magnetic (α_{M}) (blue) and non-magnetic (α_{NM}) contributions to the measured α (black).

increasing temperature / pressure he proposed there would be a charge transfer from the occupied e_g to t_{2g} orbitals in the Fe 3*d* band near the Fermi energy (i.e. from the high-volume to the low-volume state) thus effectively canceling lattice expansion. This high-spin to low-spin transition has been experimentally hinted at as a function of pressure [131]. However, such a temperature dependent spin-state transition in Fe-Ni or Fe_3Pt has never been experimentally confirmed (see below) although some theoretical work supports its existence [132].

Any t_{2g}/e_g transfer would be expected to be reflected in the magnetisation densities. As such, MCS should be an ideal technique to investigate this. Early form factor measurements with polarised neutrons [133] conclude that a decrease of the observed

total moment near the Invar regions seemed to be brought about by the decrease of the localised moment of Fe and by the increased non-local negative moment contribution in the Invar region. These measurements were followed up by Brown *et al.* [134] who studied a greater temperature range (100 - 600 K) and a slightly larger $\sin\theta/\lambda$ range on the optimally doped ($x = 0.35$) system. They concluded that the e_g orbital population does not change as a function of temperature. These data were analysed in terms of localised free atom iron and nickel 3*d* moments where the structure factor was composed of free-atom iron and nickel magnetisation distributions randomly distributed on an *fcc* lattice. It could be that this model used for describing the magnetic scattering is too simplistic. Also, the itinerant part of the moment is not well measured in neutron scattering due to the lack of Bragg peaks, thus it is possible to miss changes if the charge transfer involves an itinerant band.

More recently, a non-collinear magnetic structure has been proposed to describe the Invar effect. It was suggested that the magnetic structure is characterised, even at zero temperature, by a continuous transition from the ferromagnetic state at high volumes to a disordered non-collinear configuration at low volumes [135]. The non-collinearity gives rise to an anomalous volume dependence of the binding energy, and explains other peculiarities of Invar systems.

Recent unpublished μSR data shows a robust peak in the relaxation rate, indicative of a population renomalisation *only* in the Invar composition ($x \sim 0.35$) [136]. However, anything more quantitative is difficult muon spectroscopy. The muon is sensitive to some change in the spin fluctuation bandwidth and this peak of the relaxation rate is, to date, the only data that shows any population reordering concurrent with the Invar behaviour.

Crisan *et al.* [132] reported that chemical short- or long-range order and negative interatomic exchange interaction of electrons in anti-bonding majority-spin states force the *fcc* lattice to compete simultaneously for a smaller volume (from AF tendencies) and a larger volume (from Stoner ferromagnetic tendencies). This additional negative

lattice anharmonicity is very large for Fe-Ni alloys while absent for Fe-Pt alloys.

A similar study focusing of the Invar material Fe_3Pt was performed using magnetic Compton scattering by Taylor *et al.* [137] to try and observe any change in the band-structure as a function of temperature to support the Weiss model. In alloys of Fe-Pt, the Invar effect is observed near Fe_3Pt stoichiometry. Magnetic Compton scattering was performed on chemically ordered and disordered samples of this composition. The measurements were performed in an applied magnetic field of 1 T and in a temperature range of 15 - 500 K. The aim of that experiment was to observe some degree of charge transfer between the e_g and t_{2g} Fe 3*d* band, as suggested by the Weiss model. A charge transfer had been tentatively suggested in a statistically limited magnetic Compton scattering experiment by Srajer *et al.* [138]. However, the work by Taylor *et al.* showed there to be no shape difference in the temperature dependence of the profiles.

The purpose of this section is to present a systematic temperature and composition dependent magnetic Compton scattering study into the binary alloy $Fe_{1-x}Ni_x$, at the optimum Invar composition and above and below, where there is little or partial effect.

7.2.1 Sample characterisation

Polycrystalline samples of $Fe_{1-x}Ni_x$ ($x = 0.20, 0.35$ and $x = 0.60$) were arc-melted from 4N purity constituents and vacuum annealed at 800 °C for a week. The composition was verified by energy-dispersive X-ray spectroscopy. The samples used for this study have previously been used in a muon spin relaxation experiment (described above, Ref. [136]) and a magnetic Compton scattering experiment on the temperature dependence of the spin and orbital moments of $Fe_{1-x}Ni_x$ but were limited to below room temperature, and was the inspiration for this study, Ref [139].

7.2.2 Experimental details

The MCPs were measured on beamline BL08w at SPring-8, Japan. The measurements were made on the polycrystalline samples (cut into plates) using an incident photon energy of 183 keV in an applied magnetic field of $\pm$ 2.5 T at temperatures between 50 K and 500 K. The high temperatures were achieved with a custom built furnace insert for the magnet described below.

7.2.3 Miniature sample heater for BL08w setup

For this experiment temperatures up to 500 K were required. To achieve these high temperatures a custom built miniature heater was designed and built. The heater was designed so that it could be attached to the set up on BL08w. The sample was held between the poles of a superconducting magnet by a brass holder connected to a closed-cycle refrigerator (CCR). The brass holder was divided into two parts: a hot part and a cold part. The hot part clamped the sample and consisted of two Watlow-heater cartridges and a calibrated Pt-100. The cold part acted as an in between area, designed not to heat the cold finger and damage the CCR. The cold part also held a Pt-100 for monitoring. Good thermal contact was achieved by using MoS_2 heat-sink paste.

Due to the setup of the system, a large thermal gradient was required. To maintain this gradient, the two parts were connected by two brass screws, these screws were not threaded into the brass holder but instead into ceramic washers to minimise heat flow. As part of the experiment required the sample to be cooled, three sapphire (Al_2O_3) rods were added to bridge the two parts of the holder. Sapphire has the remarkable property of being a very good conductor of heat at low temperatures but effectively isolating itself when it gets above a certain temperature. This meant the sample could be actively cooled by the CCR through the sapphire, but when a high temperature was needed on the sample, the sapphire acts as to isolate the two parts of the holder, thus protecting the cold finger.

The system was first tested on the EMU muon spectrometer at ISIS. The cold

finger remained at 20 K whilst the hot stage reached 700 K. For the experiment at SPring-8, thermal cutoffs were installed on the Lakeshore 800 temperature controller which allowed the power to be cut to the heaters if the monitored sensors reached temperatures above the predetermined limits. If the temperature of the cold finger increased above 300 K, then the power to the heaters would be cut.

7.2.4 Results, analysis and discussion

The spin-polarised Compton profiles for the extremal temperatures of the optimum ($x = 0.35$) composition are shown in Fig. 7.4 (a). The profiles were carefully analysed so that the data at high momentum was consistent where the spin-polarised momentum density should be effectively zero. The profiles were then normalised to unit area so that subtle differences in the *shape* could be observed. As is evident in the figure, there exists a bump above the statistical noise in the region 1 - 2 a.u.. The difference profile after

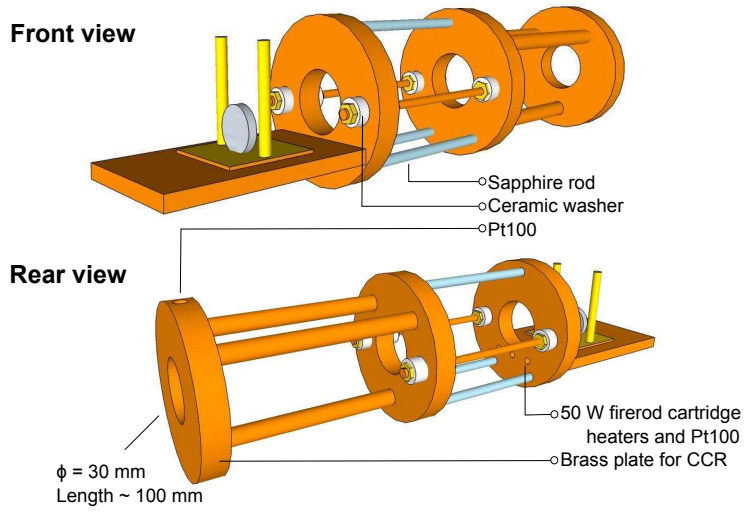

Figure 7.2: High temperature setup used for the experiments on BL08w, SPring-8. Based on a similar design for a sample heater on EMU, ISIS, Oxford

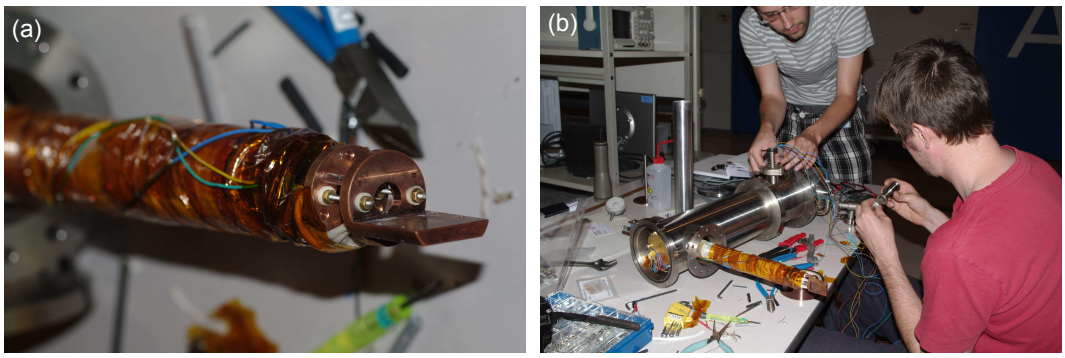

Figure 7.3: (a) Heater on the cold finger of the cryostat on BL08 W. (b) The cryostat and feedthrough.

$\approx$ 3 a.u. is consistently slightly below zero but returns to an average of zero past 9 a.u.. This suggests that the high temperature data is slightly narrower in the tails with a more pronounced peak at $\approx$ 1.5 a.u.. This narrowing would be the case if there was a charge transfer between two bands of different orbital symmetries. The effect is small but the size of the bump is shown to be temperature dependent shown in Fig. 7.4 (a):Inset. This can be most easily seen by the height of the normalised MCP peak. The average of the four data points surrounding the maximum was taken to rule out rogue points and also to increase the statistical accuracy for that temperature. Importantly, with reference to the non-Invar compositions the difference between the extremal temperatures is statistically zero (within error) i.e. there exists no structure in the difference profiles above random noise. This suggests that the population renormalisation is strongest in the Invar region ($x \approx 0.35$).

As has been shown in the oxide chapter, the shape of the Compton profile reflects the magnetic orbitals occupied. The Compton profile of a spherically averaged e_g band and a t_{2g} band are unfortunately very similar in a polycrystal. It may be possible to associate this charge transfer with a specific orbital if the experiment was repeated for a single-crystal as the different orbitals possess different angular dependencies.

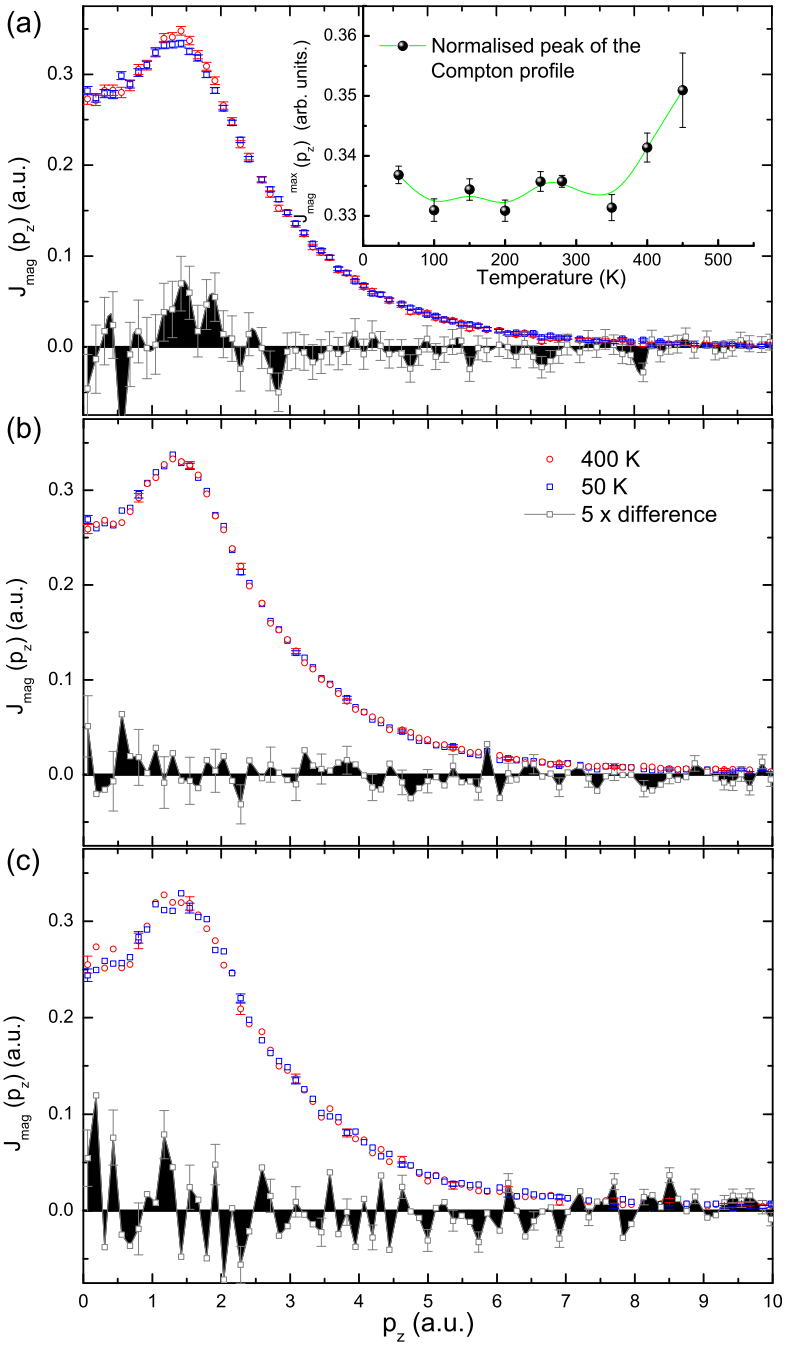

Figure 7.4: (a) Difference (grey) of high temperature (400 K, red) distribution and low temperature (100 K, blue) distributions for the $Fe_{0.65}Ni_{0.35}$ composition (Inset) Normalised peak of the magnetic Compton profile of the Invar sample. (b) $Fe_{0.8}Ni_{0.2}$ and (c) $Fe_{0.4}Ni_{0.6}$.

Table 7.1: Comparison of ASA-CPA and FP-CPA for $x = 0.20$, 0.35, 0.60 and 1.00 tabulating the different moment contributions to the magnetic Compton profile.

x	Fe (spin)	Ni (spin)	Fe-d (spin)	Ni-d (spin)	Spin (total)	Orbital (total)
ASA						
0.20	2.64	0.87	2.71	0.99	2.28	0.06
0.35	2.67	0.77	2.72	0.97	2.00	0.06
0.60	2.54	0.69	2.57	0.75	1.43	0.05
1.00		0.60		0.63	0.60	0.05
FP						
0.20	2.53	0.86	2.59	0.96	2.20	0.06
0.35	2.58	0.76	2.62	0.85	1.94	0.06
0.60	2.64	0.69	2.67	0.77	1.47	0.05
1.00		0.62		0.66	0.62	0.05

7.2.5 Band structure calculations

The electronic structure of $Fe_{1-x}Ni_x$ was calculated using the Munich SPR-KKR package [26] in both the ASA and the FP mode. The face-centered cubic crystal structure was used for $x \geq 0.35$ and the body-centered cubic lattice for $x \leq 0.35$ with lattice parameters from X-ray diffraction data from Ref. [140]. Calculations were performed fully relativistically using 1500 special k-points. Exchange correlation effects were estimated using the generalised-gradient approximation function as described in Ref. [70], as this functional has proven to describe the momentum space magnetisation distribution in pure nickel better than the LDA [11]. Table. 7.1 shows the contributions from the different bands. Due to limitations in the code the spin polarised momentum density was only calculated in the ASA but the momentum distribution is not expected to differ greatly between ASA and FP.

Calculated Compton profiles projected along the [110], [100] and [111] directions as well as a spherically averaged profile necessary to describe the polycrystallinity are

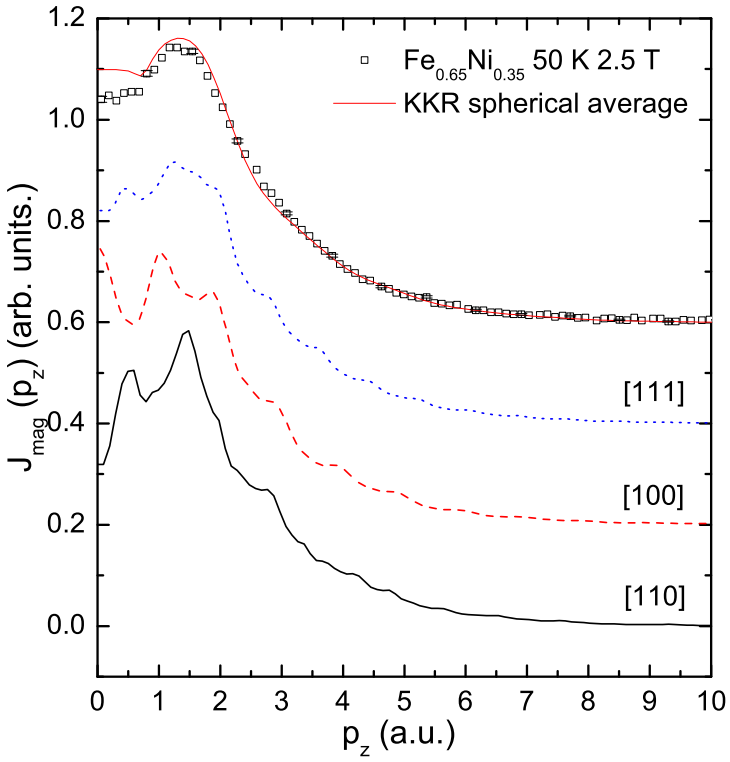

Figure 7.5: Theoretical magnetic Compton profiles for $Fe_{0.65}Ni_{0.35}$ [110],[100] and [111] directions and experimental polycrystalline magnetic Compton profile with spherically averaged and convoluted prediction (error bars are smaller than symbol size).

shown in Fig. 7.5 along with a typical experimental Compton profile. The agreement is very good. The disagreement at low momentum is not unexpected in itinerant magnetic systems and is perhaps due to an inadequate treatment of the electron-electron correlation by the code [11].

7.2.6 Conclusions

A systematic, temperature and compositional dependent spin-polarised Compton scattering experiment has been performed to investigate the changes in band occupation in the Invar materials $Fe_{1-x}Ni_x$. Subtle but distinct changes can be seen in the high temperature data for the Invar material ($x = 0.35$) but not in the off-Invar ($x = 0.2$ and $x = 0.6$) samples. This change in shape is associated with a charge transfer that

may be consistent with the Weiss two-state model. However, due to the polycrystallinity of the samples used in this experiment, a more quantitative analysis is not possible, As such, a single crystal experiment on the Invar samples is planned. The benefit of a single crystal investigation is that individual orbitals can be determined as information is not lost through the random orientation of the orbitals in the polycrystal. This population renormalisation is consistent with recent unpublished μSR data. In reference to the neutron data which observed no change, it is important to appreciate that the itinerant part of the moment contributes to the scattering at low values of $\sin\theta/\lambda$, where there are no Bragg peaks to measure on certain PND instruments. The neutron data does not see any significant change in the form-factor across the temperature range this observation is not consistent with what is measured in this thesis. More work is needed in this area to confirm the observed population renormalisation in single-crystal samples.

7.3 Spin density in pure nickel

Nickel, below T_C (632 K) is an itinerant ferromagnet. The magnetism of nickel arises from the relatively localised 3*d* band electrons, which induce a negatively polarised moment on the hybridised *sp*-like electrons. The ferromagnetic properties of nickel (at zero temperature) are well understood and have been reported by many authors [11, 141, 142]. Above T_C, however, the LDA fails to account for the local spin fluctuations. The disordered local moment (DLM) scheme was designed to account for these fluctuations and indeed works well for iron. For the weak, itinerant ferromagnet nickel, however, it fails. A framework that predicts the Curie temperature for *bcc* iron *and fcc* nickel is still yet to exist. Analysing the spin fluctuations in iron and nickel above their Curie temperatures (in their paramagnetic states) beyond the mean-field limit provides an improvement over the DLM method and finds that the magnetic properties of iron can be related to a Heisenberg model but nickel is better described by traditional Stoner theory. It is therefore expected that the exchange splitting will reduce "Stoner" fashion as the temperature is raised and local moments do not form [143].

Over the past few decades, a number of attempts have been made to directly measure the electronic structure of nickel across the Curie point. A previous magnetic Compton scattering experiment (performed in an applied magnetic field of 2 T) claimed to show a change in the lineshape along the [100] direction, indicating that the negatively polarised *sp*-contribution persists more strongly than the local 3*d* moment at 640 K. The statistical accuracy of their measurement make the validity of this claim uncertain. Results shown in Fig. 7.6 (a) [144].

Spin-polarised (two-dimensional angular-correlation of annihilation radiation) 2D ACAR spectroscopy in an applied magnetic field of 4 T was also performed [145] which suggests very little change on the spin-polarised momentum distribution. The positron is biased to annihilate electrons away from the core due to positron-core repulsion. As such, if there were any change in the itinerant electron distribution, then the positron would

be sensitive to it. Polarised neutron scattering (at 4.6 T) [146] measured 22 independent reflections. By comparing neutron diffraction and bulk magnetisation measurements, the authors saw no significant change in the nickel form factor except in the (111) reflection where it was suggested that the negatively polarised moment disappears at temperatures $\approx T_C$, however, then changes sign and increases above T_C, shown in Fig. 7.6 (b).

As with the Invar alloys described in §7.2, these neutron diffraction data were analysed in terms of cubic free atom Ni form factors. According to their analysis at room temperature the *sp*-hybridised bands contribute more than $\sim$ -0.1 μ_B to the spin moment. It is shown however, that the *sp*-contribution is significantly lower, -0.042 μ_B in calculations performed for this thesis.

More recently, the transient electronic structure of nickel was investigated by XMCD [147]. The authors compared XMCD spectra of thin film nickel taken at room temperature and spectra taken after heating the thin film with a 100 ps laser pulse. They estimated the heated temperature to be $T/T_C = 0.93$ (588 K) from the reduction in the XMCD peak. Additionally, they saw that the *shape* was different at high T, the nickel absorption spectra was characterised by a shift of the L_2 edge and satellite. This,

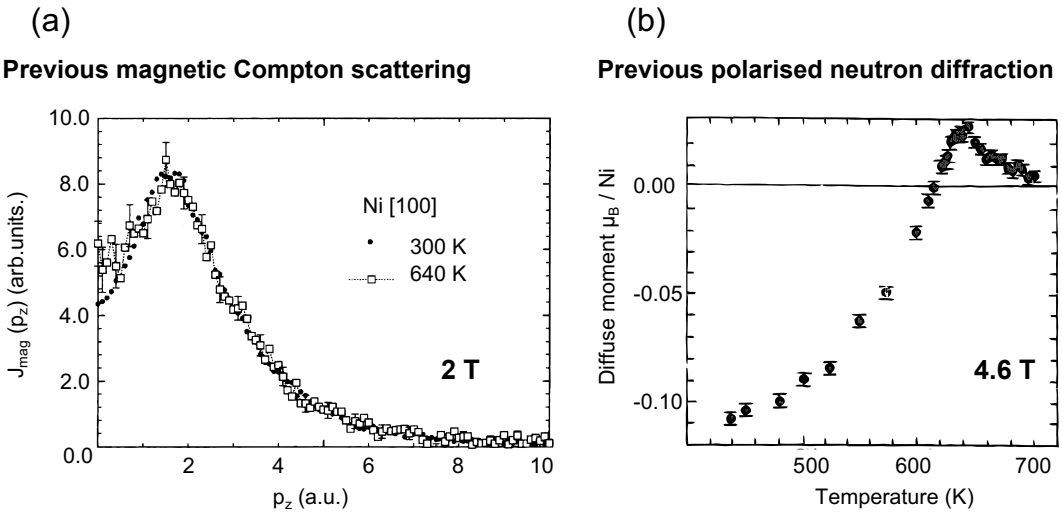

Figure 7.6: (a) Temperature dependence of spin-polarised electron momentum density at in an applied field of 2 T adapted from [144] (b) Temperature dependence of the diffuse magnetisation in nickel in an applied field of 4.6 T adapted from [146].

in conjunction with cluster calculations, the authors attributed to a reduction in the 3*d*-*sp* hybridisation.

The purpose of this section is to contribute new results from a higher statistic magnetic Compton scattering experiment into the spin density of nickel below and above T_C.

7.3.1 Sample characerisation

Single crystalline samples of nickel were grown and oriented along the [100] direction using a Laue diffraction camera. The nickel sample has been fully characterised in previous magnetic Compton scattering experiments as it is routinely used as the normalisation sample. High temperature SQUID magnetometry was made on our sample in a commercial insert for a 5 T SQUID magnetometer, the temperature dependent magnetisation is shown in Fig. 7.9.

7.3.2 Experimental details

Whilst in the ferromagnetic regime the magnetic signal is large (typically 0.5 % of the charge signal), at T_C and at $T/T_C = 1.1$, the moment is very small and requires a large external field in order to induce a moment. This has only recently become possible due to the advances in detector technology and incident photon flux. The spin polarised Compton profiles were measured on beam line ID15A at the ESRF. The measurements were made using an incident photon energy of 220 keV in an applied magnetic field of 1 T in the FM (250 K) regime and 4 T in the paramagnetic (650 K) regime. The experiment was performed at a scattering angle of 172°. The momentum resolution of the magnetic Compton spectrometer was 0.44 a.u. of momentum. The data were corrected for energy dependent detector efficiency, sample absorption and the relativistic scattering cross section. The high temperatures were achieved with a new custom built furnace insert for the high-field magnet, detailed below.

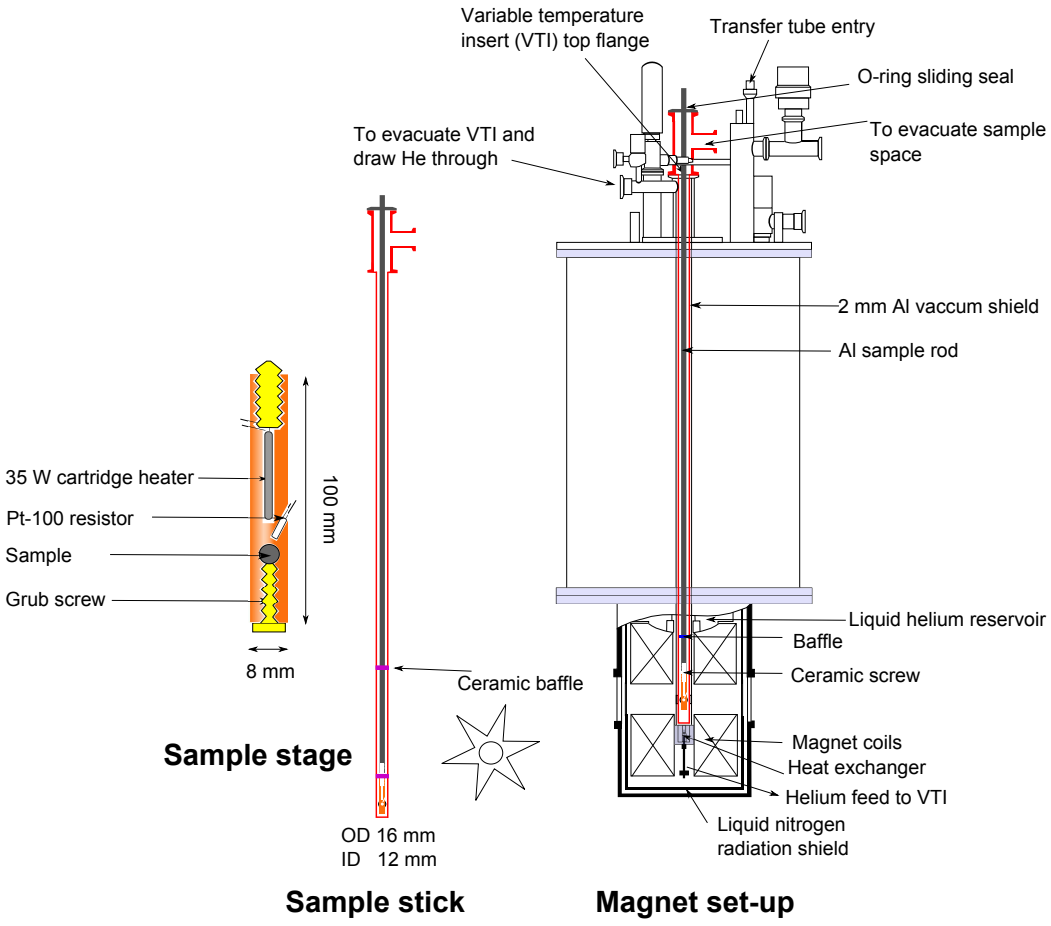

Figure 7.7: Custom built high temperature sample stick in high-field Spectromag magnet used for magnetic Compton experiment on nickel.

7.3.3 Miniature sample heater for ID15A setup

The high temperatures needed for this experiment were achieved using a specially designed and constructed furnace different from the one used on BL08w. The furnace needed to fit inside the already present VTI but be thermally isolated from it. To achieve this isolation a vacuum shield was first installed with the heater stick inside. The heat-shield was evacuated to minimise convection and heat transfer from the sample stage.

The sample heater was a cylinder of copper drilled out to accommodate the nickel sample, a Pt-100 and a 35 W Watlow-firerod cartridge. Good thermal contact

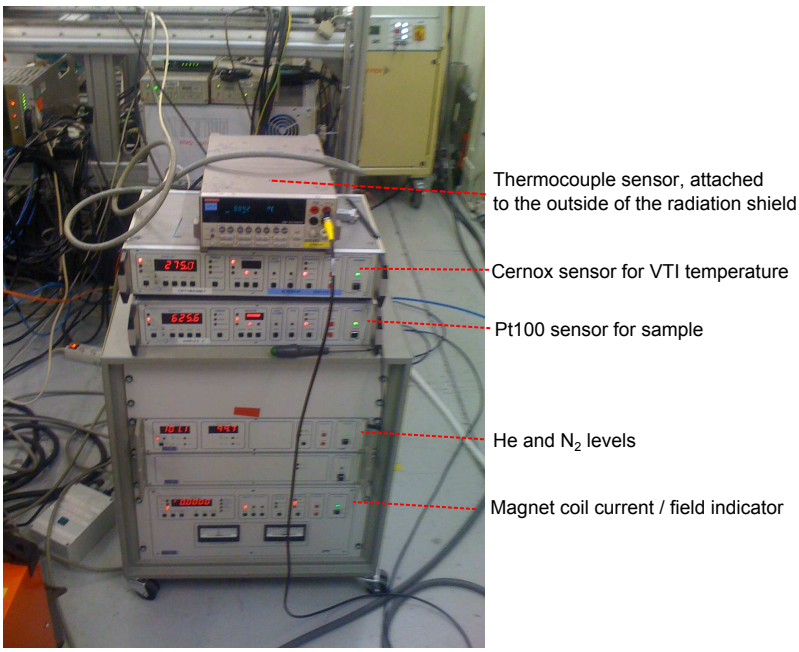

Figure 7.8: Equipment required to provide high-field, high-temperature environment for the Compton experiment. (Value of top Keithley in °C, both ITCs are in K, level meters in % and field indicator in T.)

was achieved using ZnO suspended in silicone. The copper was graphene coated by chemical vapour deposition to minimise oxidation, thereby retaining its shininess and therefore minimise its emissivity. The copper was attached to the main aluminium shaft by a ceramic screw and baffled to the heat-shield by ceramic washers to avoid movement in a field. The ceramic washers were shaped to minimise the touching area.

The sample temperature was regulated by an Oxford Instruments ITC^{503} temperature controller. The maximum output voltage for the heaters was set to 25 V into a resistance of 30 Ω resulting in a (maximum) power of 20.8 W. This power was found necessary to adequately control the temperature at 650 K. To keep a low temperature on the VTI, a small flow of exchange helium gas was used to maintain the temperature being actively and independently controlled by another separate ITC^{503}.

Due to the high-temperatures, high-fields and (potentially) high pressure gases used in the setup, various safety features were installed. The radiation shield had a thermocouple (non-magnetic type-T- constantan and copper) attached to it around the

hottest part. The temperature of the VTI was also monitored. The macro used to run the experiment and acquire the data was rewritten with a trap for monitoring all the temperatures.

- T_{sample}. If the temperature of the sample increases by 10 K unexpectedly, this could indicate a failure of the Pt-100. If it falls (by 10 K) then the heater cartridge could have failed. Either event would cut power to the heater.

- T_{shield}. If the temperature of the shield increased to above previously determined acceptable limits, this indicates that the heater could be touching the heat shield and the heater power would be cut.

- T_{VTI}. If the VTI temperature rises to above room temperature, this could indicate of heating directly from the hot-source to the VTI and the power is cut. This limit is set particularly low as the VTI is close to indium seals on the magnet which can distort above room temperature.

When running for extended periods the temperatures recorded on the three monitors were. $T_{\mathrm{shield}} = 351 \pm 3$ K, $T_{\mathrm{VTI}} = 275 \pm 1$ K and $T_{\mathrm{sample}} = 650 \pm 3$ K.

7.3.4 Results, analysis and discussion

7.3.4.1 Magnetic Compton scattering results

Magnetic Compton profiles from ID15 A are shown in Fig. 7.9. Both the high temperature, 650 K (red) and low temperature, 250 K (blue) data are shown along with a calculated profile from *fcc* nickel projected along the [100] crystal direction and convoluted with the a Gaussian expressing the experimental resolution (full-width half-maximum (FWHM) = 0.44 a.u.).

The data were treated in the same way as the Invar polycrystals. i.e. the high momentum tails were checked for consistency. The difference was then taken to identify any change in the shape of the profile. Plotted in Fig. 7.9 is the difference

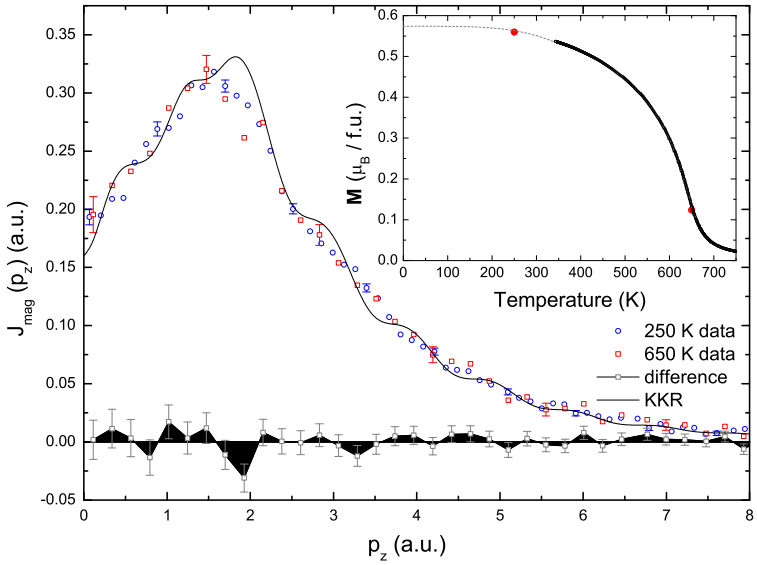

Figure 7.9: (Main) High temperature (650 K (red)) and low temperature (350 K (blue)) MCPs with difference. Experimental low temperature profile with predicted KKR calculation broadened by the experimental momentum resolution (0.44 a.u.).. (Inset) Saturation magnetisation as a function of temperature in an applied 4 T field. Plotted with spin moments from magnetic Compton scattering. Error bars are smaller than the symbol size.

of the high temperature and the low temperature data. The difference is shaded to highlight the oscillations above and below zero. There is no structure in the oscillations as there was in the $Fe_{0.65}Ni_{0.35}$ data. The reduction of the total moment is shown in the inset of Fig. 7.9, the 250 K data was taken near the saturated moment. The high temperature data however, shows that the total moment has been reduced by a factor of approximately 4.

From this it is shown there is no change in the itinerancy of the moment as this would manifest itself as an increase or decrease in the low-momentum component. This is at odds with previous magnetic Compton scattering result and XMCD data which show a reduction in the *sp*-hybridisation at elevated temperatures, but in agreement with positron annihilation.

7.4 Conclusions

A temperature dependent study into the spin-polarised momentum distribution was performed on single crystal nickel. No change was found in the momentum distribution across the ferromagnetic to paramagnetic transition. It is shown that the exchange splitting reduces the same for 3*d* electrons and the *sp*-like electrons, with no observable change in the hybridisation. This is at odds with a previously reported, statistically limited magnetic Compton scattering experiment and polarised neutron data, however, it is consistent with spin-polarised 2D-ACAR data.

Chapter 8

Conclusions

8.0.1 Concluding remarks

Over the past decade magnetic Compton scattering has evolved from a proof of principle technique into a cutting edge research tool in the field of magnetisation densities. The work contained in this thesis describes results from magnetic Compton scattering experiments applied to the field of strongly correlated electron systems. The purpose of this research was to utilize the unique abilities of magnetic Compton scattering and in conjunction with new high-field facilities and novel modeling techniques shed light on some exciting, novel materials.

8.0.2 High field oxides

Complex oxides exhibit a huge range of properties, studied here are two metamagnetic oxides. Of interest are the orbitals responsible for the magnetic behaviour. Using a molecular orbital modeling technique, the orbitals which compose the magnetic Compton profiles are identified as is the magnitude of any oxygen contribution. The relevance of this work is in how individual orbital contributions can be made by measuring as few a one magnetic Compton profile, this allows detailed comparisons with band structure calculations to be made. This work also demonstrates some of the highest field, lowest

moment results ever obtained. Extensions to this work would be in pushing the limit of the size of the signals measurable. There are currently plans to move the high-field 9 T magnet to BL08w, SPring-8 to exploit the ultra-stable beam.

8.0.3 Uranium superconductors

The technique is unique in its ability to separate the magnetic moment of a sample into its spin, **S** and orbital, **L** contributions without the need of modeling. Work in this thesis on the uranium class of superconductors shows the importance of separating **S** and **L** when describing the magnetism in these novel systems. UCoGe is a ferromagnet on the verge of a magnetic phase transition. Work in this thesis determines the magnetic structure in the normal phase and relates it to the itinerancy of the uranium $5f$ electrons. UGe_2 is studied to determine the nature of the magnetic transition at T^* in the ferromagnetic regime. A temperature dependent shape change is observed which could be related to its superconducting properties. The relevance of this work is in highlighting the importance of separating **S** and **L** to better describe the underlying electronic structure of these complex materials. Further work investigating the pressure dependence of the magnetism are currently feasible and would be highly instructive in these materials. Further studies are also required on URhGe so that conclusions across the entire range or uranium superconductors can be drawn.

8.0.4 High temperature magnetic Compton scattering

The magnetism in the $Fe_{1-x}Ni_x$ range of alloys has been studied in chapter 6. The aim was to observe subtle changes in the magnetisation density which could be related to the observed macroscopic properties. Changes perhaps related with the Invar effect were observed in the $x = 0.35$ composition. However, no change was seen in pure nickel which had been hinted at in previous studies. A single crystal investigation of $Fe_{0.65}Ni_{0.35}$ would be advantageous for a fuller understanding. The relevance of this work highlights the flexibility of the magnetic Compton scattering technique in its ability to

study samples at high temperatures and without the need of high quality, single crystals.

8.0.5 Future trends

Using the ultra-stable, automatically topped-up beam at SPring-8 it is hoped that even smaller signals will be measurable. The application of higher pressures will extend the range of magnetic Compton scattering studies further into a larger area of a samples phase diagram. The work in this thesis shows how high quality, high magnetic field data can be gathered and in conjunction with some modeling techniques described here can be used to obtain unique and vitally important information on strongly correlated electron systems. These trends will continue to see magnetic Compton scattering as an invaluable technique in the study of strongly correlated materials.

Bibliography

[1] Stephen Blundell. Magnetism in condensed matter. Oxford University Press, 2001.

[2] C. Pfleiderer. Superconducting phases of f-electron compounds. Review of Modern Physics, 81:1552, 2009.

[3] Arthur H. Compton. A Quantum Theory of the Scattering of X-rays by Light Elements. Physical Review, 21(5):483, 1923.

[4] A. M. Bebb, J. W. Taylor, J. A. Duffy, Z. F. Banfield, M. J. Cooper, M. R. Lees, J. E. McCarthy, and D. N. Timms. Temperature and field dependence of the spin magnetization density in $SmMn_2Ge_2$. Phys. Rev. B, 71(2):024407, 2005.

[5] J. A. Duffy, J. W. Taylor, S. B. Dugdale, C. Shenton-Taylor, M. W. Butchers, M. J. Cooper, Y. Sakurai, and M. Itou. Spin and orbital moments in Fe_3O_4. Phys. Rev. B., 81:134424, 2010.

[6] P. K. Lawson, M. J. Cooper, M. A. G. Dixon, D. N. Timms, E. Zukowski, F. Itoh, and H. Sakurai. Magnetic-Compton-scattering study of spin moments in UFe_2. Phys. Rev. B, 56:3239, 1997.

[7] A. Koizumi, S. Miyaki, Y. Kakutani, H. Koizumi, N. Hiraoka, K.i Makoshi, N. Sakai, K. Hirota, and Y. Murakami. Study of the e_g orbitals in the bilayer manganite $La_{2-2x}Sr_{1+2x}Mn_2O_7$ by using magnetic Compton-profile measurement. Journal of Physics and Chemistry of Solids, 66(24):2183, 2005.

[8] C. Rumble, M. Itou, N. Hiraoka, Y. Sakurai, Y. Tomioka, Y. Tokura, J. E. Penner-Hahn, and A. Deb. Imaging of 3*d* Mn orbitals in the ferromagnetic state for Ca-substituted manganite: Magnetic Compton investigation. Phys. Rev. B., 85:045128, 2012.

[9] N. Hiraoka, M. Itou, A. Deb, Y. Sakurai, Y. Kakutani, A. Koizumi, N. Sakai, S. Uzuhara, S. Miyaki, H. Koizumi, K. Makoshi, N. Kikugawa, and Y. Maeno. Ru-O orbital hybridization and orbital occupation in $SrRuO_3$: A magnetic Compton-profile study. Phys. Rev. B, 70:054420, 2004.

[10] N. Qureshi, M. Zbiri, J. Rodríguez-Carvajal, A. Stunault, E. Ressouche, T. C. Hansen, M. T. Fernández-Díaz, M. R. Johnson, H. Fuess, H. Ehrenberg, Y. Sakurai, M. Itou, B. Gillon, Th. Wolf, J. A. Rodríguez-Velamazan, and J. Sánchez-Montero. Experimental magnetic form factors in $Co_3V_2O_8$: A combined study of ab initio calculations, magnetic Compton scattering, and polarized neutron diffraction. Phys. Rev. B., 79:094417, 2009.

[11] M. A. G. Dixon, J. A. Duffy, S. Gardelis, J. E. McCarthy, M. J. Cooper, S. B. Dugdale, T. Jarlborg, and D. N. Timms. Spin Density in ferromagnetic nickel: a magnetic Compton scattering study. J. Phys. Condens. Matter, 10:2759, 1998.

[12] J. W. Taylor, J. A. Duffy, A. M. Bebb, M. J. Cooper, S. B. Dugdale, J. E. McCarthy, D. N. Timms, D. Greig, and Y. B. Xu. Magnetic Compton scattering study of the ferromagnetic amorphous alloys $Fe_{1-x}B_x$. Phys. Rev. B., 63:220404(R), 2001.

[13] J. T. Okada, P. H.-L. Sit, Y. Watanabe, Y. J. Wang, B. Barbiellini, T. Ishikawa, M. Itou, Y. Sakurai, A. Bansil, R. Ishikawa, M. Hamaishi, T. Masaki, P.-F. Paradis, K. Kimura, T. Ishikawa, and S. Nanao. Persistence of Covalent Bonding in Liquid Silicon Probed by Inelastic X-ray Scattering. Phys. Rev. Lett., 108:067402, 2012.

[14] Neil W. Ashcroft and N. David Mermin. Solid state physics. Saunders College Publishing, 1976.

[15] Charles Kittel. Introduction to solid state physics. Wiley, Hoboken, NJ, 8th edition, 2005.

[16] J. B. Goodenough. An interpretation of the magnetic properties of the perovskite-type mixed crystals $La_{1-x}Sr_xCoO_{3-\lambda}$. J. Phys. Chem. Solis., 6:287, 1958.

[17] Hans Ludwig Schläfer and Günter Giliemann. Basic principles of ligand field theory. Wiley-Interscience, 1969.

[18] G H Lander. Handbook on the Physics and Chemistry of Rare Earths,. Elsevier Science, Amsterdam, 1993.

[19] Patrik Fazekas. Lecture notes on electron correlation and magnetism. World Scientific Pub Co Inc, 1999.

[20] Rajbir Singh. Inorganic chemistry, transition elements. Mittal, 2002.

[21] David S. Sholl and Janice A. Steckel. Density functional theory. Wiley, 2009.

[22] M. W. Schmidt, K. K. Baldridge, J.A. Boatz, S.T. Elbert, M.S. Gordon, J.H. Jensen, S. Koseki, N. Matsunaga, K.A. Nguyen, S. Su, T.L. Windus, M. Dupuis, and J.A. Montgomery. General atomic and molecular electronic structure system. J. Comput. Chem, 14:1347, 1993.

[23] A. Saenz, T. Asthalter, and W. Weyrich. Methods for the calculation of spherically averaged Compton profiles with GTOs. International Journal of Quantum Chemistry, 65:11, 1997.

[24] P. Hohenberg and W. Kohn. Inhomogenous electron gas. Phys. Rev., 36:B864, 1964.

[25] W. Kohn and L. J. Sham. Self-consistent equations including exchange and correlation effects. Phys. Rev., 140:A1133, 1965.

[26] The Munich SPR-KKR package, version 5.4,
H. Ebert et al.
http://www.ebert.cup.uni-muenchen.de/SPRKKR
Rep. Prog. Phys. **74**, 096501, 2011.

[27] http://elk.sourceforge.net/ .

[28] David J. Singh and Lars Nordström. Planewaves, Pseudopotentials and the LAPW method. Springer US, 2006.

[29] O. Klein and T. Nishina. Über die Streuung von Strahlung durch freie Elektronen nach der neuen relativistischen Quantendynamik von Dirac. Zeitschrift für Physik a Hadrons and Nuclei, 52:853, 1929.

[30] J. W. M. DuMond. Compton modified line structure and its relation to the electron theory of solid bodies. Phys. Rev., 33:643, 1929.

[31] Malcolm Cooper. X-ray Compton scattering. Oxford series on synchrotron radiation. Oxford University Press, Oxford, 2004.

[32] Alastair I M Rae. Quantum Mechanics. Institute of Physics, 2005.

[33] P.M. Platzman and N. Tzoar. Magnetic scattering of X rays from electrons in molecules and solids. Phys. Rev. B., 2(9):3556–3559, 1970.

[34] M. J. Cooper. Compton scattering and electron momentum determinationk. Rep. Prog. Phys., 48:415, 1985.

[35] F. W. Lipps and H. A. Tolhoek. Polarization phenomena of electrons and photons. ii: Results for Compton scattering. Physica, 20:385, 1954.

[36] Mark Dixon. Studies of spin and charge momentum densities using Compton scattering. PhD thesis, School of Physics, University of Warwick, 1998.

[37] N. Sakai and Kazuo Ono. Compton profile due to magnetic electrons in ferromagnetic iron measured with circularly polarized gamma rays. Physical Review Letters, 37(6):351, 1976.

[38] M. J. Cooper, S. P. Collins, D. N. Timms, A. Brahmia, P. P. Kane, R. S. Holt, and D. Laundy. Magnetic anisotropy in the electron momentum density of iron. Nature, 333:151, 1988.

[39] J. E. McCarthy, J. A. Duffy, C. Detlefs, M. J. Cooper, and P. C. Canfield. $4f$ spin density in the reentrant ferromagnet $SmMn_2Ge_2$. Physical Review B, 62:R6073, 2000.

[40] M. J. Cooper. Magnetic Compton scattering from $HoFe_2$. Physica B, 192:191, 1993.

[41] James A. Clarke. The science and technology of undulators and wigglers. Oxford science publications, 2004.

[42] Philip John Duke. Synchrotron radiation: production and properties. Oxford science publications, 2000.

[43] N. Sakai. Magnetic Compton scattering and measurements of momentum distribution of magentic electrons. J. Appl. Cryst., 29:81, 1996.

[44] Caroline Shenton-Taylor. Development of high field magnetic Compton scattering studies of strongly correlated materials. PhD thesis, University of Warwick, 2007.

[45] F. Bell, J. Felsteiner, and L. P. Pitaevskii. Cross section for Compton scattering by polarized bound electrons. Physical Review A, 53:R1213, 1996.

[46] J. Felsteiner, P. Pattison, and M. J. Cooper. Effect of multiple scattering on experimental Compton profiles: a Monte Carlo calculation. Philos. Mag., 30:537, 1974.

[47] B. T. Thole, P. Carra, F. Sette, and G. van der Laan. X-ray circular dichroism as a probe of orbital magnetization. Physical Review Letters, 68:1943, 1992.

[48] S. W. Lovesey and S. P. Collins. X-ray scattering and absorption by magnetic materials. Oxford series on synchroton radiation. Clarendon Press, Oxford, 1996. S.W. Lovesey, S.P. Collins. ill ; 24cm. Oxford series on synchrotron radiation.

[49] Andreas Scherz. Spin-dependent x-ray absorption spectroscopy of 3d transition metals: systematics and applications. PhD thesis, Freien Universität Berlin, 2003.

[50] C. T. Chen, Y. U. Idzerda, H. J. Lin, N. V. Smith, G. Meigs, E. Chaban, G. H. Ho, E. Pellegrin, and F. Sette. Experimental confirmation of the X-ray magnetic circular dichroism sum rules for iron and cobalt. Physical Review Letters, 75(1):152, 1995.

[51] S. Agrestini, C. Mazzoli, A. Bombardi, and M. R. Lees. Incommensurate magnetic ground state revealed by resonant X-ray scattering in the frustrated spin system $Ca_3Co_2O_6$. Physical Review B, 77:140403, 2008.

[52] B. Barbiellini, A. Koizumi, P. E. Mijnarends, W. Al-Sawai, Hsin Lin, T. Nagao, K. Hirota, M. Itou, Y. Sakurai, and A. Bansil. Role of oxygen electrons in the metal-insulator transition in the magnetoresistive oxide $La_{2-2x}Sr_{1+2x}Mn_2O_7$ probed by Compton scattering. Physical Review Letters, 102(20):206402, 2009.

[53] S. R. Giblin, J. W. Taylor, J. A. Duffy, M. W. Butchers, C. Utfeld, S. B. Dugdale, T. Nakamura, C Visani, and J. Santamaria. Magnetic correlation in the normal phase of a superconducting oxide. Phys. Rev. Lett., 109:137005, 2012.

[54] R. Fresard, C. Laschinger, T. Kopp, and V. Eyert. Origin of magnetic interactions in $Ca_3Co_2O_6$. Phys. Rev. B., 69:140405, 2004.

[55] A. Maignan, V. Hardy, S. Hebert, M. Drillon, M. R. Lees, O. Petrenko, D. McK. Paul, and D. Khomskii. Quantum tunneling of the magnetization in the Ising chain compound $Ca_3Co_2O_6$. J. Mater. Chem., 14:1231, 2004.

[56] Yuri B. Kudasov. Steplike magnetization in a spin-chain system: $Ca_3Co_2O_6$. Physical Review Letters, 96:027212, 2006.

[57] R. Soto, G. Martínez, M. N. Baibach, J. M. Florez, and P. and Vargas. Metastable states in the triangular-lattice Ising model studied by Monte Carlo simulations: Application to the spin-chain compound $Ca_3Co_2O_6$. Phys. Rev. B., 79:184422, 2009.

[58] S. Aasland, H. Fjellvåg, and B. Hauback. Magnetic properties of the one-dimensional $Ca_3Co_2O_6$. Solid State Communications, 101:187, 1997.

[59] Hua Wu, M. W. Haverkort, Z. Hu, D. I. Khomskii, and L. H. Tjeng. Nature of magnetism in $Ca_3Co_2O_6$. Physical Review Letters, 95:186401, 2005.

[60] R. Vidya, P. Ravindran, H. Fjellvåg, A. Kjekshus, and O. Eriksson. Tailor-made electronic and magnetic properties in one-dimensional pure and Y-substituted $Ca_3Co_2O_6$. Physical Review Letters, 91:186404, 2003.

[61] T. Burnus, Z. Hu, M. W. Haverkort, J. C. Cezar, D. Flahaut, V. Hardy, A. Maignan, N. B. Brookes, A. Tanaka, H. H. Hsieh, H. J. Lin, C. T. Chen, and L. H. Tjeng. Valence, spin, and orbital state of Co ions in one-dimensional $Ca_3Co_2O_6$: An X-ray absorption and magnetic circular dichroism study. Physical Review B, 74(24):245111, 2006.

[62] S. Agrestini, L. C. Chapon, Daoud-Aladine A., J. Schefer, A. Gukasov, C. Mazzoli,

M. R. Lees, and O. A. Petrenko. Nature of the Magnetic Order in $Ca_3Co_2O_6$. Phys. Rev. Lett., 101:097207, 2008.

[63] S. Agrestini, C. L. Fleck, L. C. Chapon, C. Mazzoli, A. Bombardi, M. R. Lees, and O. A. Petrenko. Slow magnetic order-order transition in the spin-chain antiferromagnetic $Ca_3Co_2O_6$. Phys. Rev. Lett., 106:197204, 2011.

[64] C. L. Fleck, M. R. Lees, S. Agrestini, G. J. McIntyre, and O. A. Petrenko. Field-driven magnetisation steps in $ca_3co_2o_6$: A single-crystal neutron-diffraction study. Europhysics Letters, 90:6, 2010.

[65] G. Allodi, R De Renzi, S. Agrestini, C. Mazzoli, and M. R. Lees. NMR study of magnetic order, metamagnetic transitions, and low-temperature spin freezing in $Ca_3Co_2O_6$. Phys. Rev. B., 83:104408, 2011.

[66] C. Mazzoli, A. Bombardi, S. Agrestini, and M. R. Lees. Resonant x-ray scattering study of $Ca_3Co_2O_6$ ground state: Preliminary results of magnetic field effects. Physica B, 404:3042, 2009.

[67] A. Bombardi, C. Mazzoli, S. Agrestini, and M. R. Lees. Resonant x-ray scattering investigation of the multipolar ordering in $Ca_3Co_2O_6$. Phys. Rev. B., 78:100406(R), 2008.

[68] V. Hardy, S. Lambert, M. R. Lees, and D. McK. Paul. Specific heat and magnetization study on single crystals of the frustrated quasi-one-dimensional oxide $Ca_3Co_2O_6$. Physical Review B, 68:01442, 2003.

[69] H. Fjellvåg, E. Gulbrandsen, A. Aasland, A. Olsen, and B. C. Haunback. Crystal structure and possible charge ordering in one-dimensional $Ca_3Co_2O_6$. Journal of Solid State Chemistry, 124(0224):4, 1996.

[70] J. P. Perdew, K. Burke, and M. Ernzerhof. Generalized gradient approximation made simple. Phys. Rev. Lett., 77:3865, 1996.

[71] D. Stoeffler. Electronic structure and magnetic properties of $Ca_3Co_2O_6$ cobaltites: Intrachain magnetic ordering. Microelectronic Engineering, 85:2451, 2008.

[72] A. Villesuzanne and M.-W. Whangbo. Comparative electronic band structure study of the intrachain ferromagnetic versus antiferromagnetic coupling in the magnetic oxides $Ca_3Co_2O_6$ and Ca_3FeRhO_6. Inorg. Chem., 44:6339, 2005.

[73] B. Raquet, M. N. Baibich, J. M. Broto, H. Rakoto, S. Lambert, and A. Maignan. Hopping conductivity in one-dimensional $Ca_3Co_2O_6$ single crystal. Phys. Rev. B., 65:104442, 2002.

[74] A. L. Efros and B. I. Shklovskii. Coulomb gap and low temperature conductivity of disordered systems. J. Phys. C: Solid State Phys., 8:L49, 1975.

[75] A. Schäfer, C. Huber, and R. Ahlrichs. Fully optimized contracted Gaussian basis sets of triple zeta valence quiality for atoms Li to Kr. J. Chem. Phys., 100:5829, 1994.

[76] F. Biggs, L. B. Mendelsohn, and J. B. Mann. Hartree-Fock Compton profiles for the elements. Atomic Data and Nuclear Data Tables, 16:201, 1975.

[77] L. Capogna, E. M. Forgan, S. M. Hayden, A. Wildes, J. A. Duffy, A. P. Mackenzie, R. S. Perry, S. Ikeda, Y. Maeno, and S. P. Brown. Observation of two-dimensional spin fluctuations in the bilayer ruthenate $Sr_3Ru_2O_7$ by inelastic neutron scattering. Physical Review B, 67(1):012504, 2003.

[78] J. A. Duffy, S. M. Hayden, Y. Maeno, Z. Mao, J. Kulda, and G. J. McIntyre. Polarized-neutron scattering study of the Cooper-pair moment in Sr_2RuO_4. Physical Review Letters, 85(25):5412, 2000.

[79] S. A. Grigera, R. S. Perry, A. J. Schofield, M. Chiao, S. R. Julian, G. G. Lonzarich, S. I. Ikeda, Y. Maeno, A. J. Millis, and A. P. Mackenzie. Magnetic field-tuned

quantum criticality in the metallic ruthenate $Sr_3Ru_2O_7$. Science, 294:329–332, 2001.

[80] R.S. Perry, T. Tayama, K. Kitagawa, T. Sakakibara, K. Ishida, and Y. Maeno. Investigation into the itinerant metamagnetism of $Sr_3Ru_2O_7$ for the field parallel to the ruthenium oxygen planes. Journal of the Physical Society of Japan, 74(4):1270, 2005.

[81] A. V. Puchkov, Z.-X. Shen, and G. Cao. Electronic band structure of $Sr_3Ru_2O_7$. Phys. Rev. B, 58:6671, 1998.

[82] D. J. Singh and I. I. Mazin. Electronic structure and magnetism of $Sr_3Ru_2O_7$. Phys. Rev. B., 63:8, 2000.

[83] A. Tamai, M. P. Allan, J. F. Mercure, W. Meevasana, R. Dunkel, D. H. Lu, R. S. Perry, A. P. Mackenzie, D. J. Singh, Shen Z.-X., and F. Baumberger. Fermi surface and van Hove singularities in the itinerant metamagnet $Sr_3Ru_2O_7$. Physical Review Letters, 101:026407, 2008.

[84] D. J. Singh and D. A. Papaconstantopoulos. Electronic structure and magnetism of complex materials. Springer-Verlag, 2003.

[85] H. Shaked, J. D. Jorgensen, O. Chmaissem, S. Ikeda, and Y. Maeno. Neutron diffraction study of the structural distortions in $Sr_3Ru_2O_7$. Journal of Solid State Chemistry, 154:361, 2000.

[86] K. Kitagawa, K. Ishida, R. S. Perry, H. Murakawa, K. Yoshimura, and Y. Maeno. Orbital properties of $Sr_3Ru_2O_7$ and related ruthenates probed by ^{17}O NMR. Physical Review B (Condensed Matter and Materials Physics), 75(2):024421, 2007. APS.

[87] R. S. Perry and Y. Maeno. Systematic approach to the growth of high-quality single crystal $Sr_3Ru_2O_7$. Journal of Crystal Growth, 271:134, 2004.

[88] R. A. Borzi, A. McCollam, J. A. N. Bruin, A. P. Perry, R. S. ad Mackenzie, and S. A. Grigera. Hall coefficient anomaly in the low-temperature high-field phase of $Sr_3Ru_2O_7$. Phys. Rev. B., 84:205112, 2011.

[89] W. Wu, S. A. McCollam, Grigera, R. S. Perry, A. P Mackenzie, and S. R. Julian. Quantum critical metamagnetism of $Sr_3Ru_2O_7$ under hydrostatic pressure. Phys. Rev. B., 83:045106, 2011.

[90] J. F. Mercure, A. W. Rost, E. C. T. O'Farrell, S. K. Goh, R. S. Perry, M. L. Sutherland, S. A. Grigera, R. A. Borzi, P. Gegenwart, A. S. Gibbs, and A. P. Mackenzie. Quantum oscillations near the metamagnetic transition in $Sr_3Ru_2O_7$. Phys. Rev. B., 81:235103, 2010.

[91] B. Barbiellini, S. B. Dugdale, and T. Jarlborg. The EPMD-LMTO program for electron-positron momentum density calculations in solids. Computational Materials Science, 28:287, 2003.

[92] P. J. Hay and W. R. Hadt. Ab initio effective core potentials for molecular calculations. potentials for the transition metal atoms Sc to Hg. Journal of Chemical Physics, 82:270, 1985.

[93] S. S. Saxena, P. Agarwal, K. Ahilan, F. M Grosche, R. K. W. Haselwimmer, M. J. Steiner, E. Pugh, I. R. Walker, S. R. Julian, P. Monthoux, G. G. Lonzarich, A. Huxley, I. Sheikin, D. Braithwaite, and J. Flouquet. Superconductivity on the border of itinerant-electron ferromagnetism in UGe_2. Nature, 406:587, 2000.

[94] J. Bardeen, L. N. Cooper, and J. R. Schrieffer. Theory of superconductivity. Phys. Rev., 108:1175, 1957.

[95] H. H. Hill. Plutonium and Other Actinides. AIME, New York, 1970.

[96] G. H. Lander, M. S. S. Brook, and B. Johansson. Orbital band magnetism in actinide intermetallics. Phys. Rev. B., 43:13672, 1991.

[97] D. Benea, J. Minár, L. Chioncel, S. Mankovsky, and H. Ebert. Magnetic Compton profiles of Fe and Ni corrected by dynamical electron correlations. Phys. Rev. B., 2012.

[98] N. T. Huy, A. Gasparini, D. E. de Nijs, Y. Huang, J. C. P. Klaasse, T. Gortenmulder, A. de Visser, A. Hamann, T. Gorlach, and H. v. Lohneysen. Superconductivity on the border of weak itinerant ferromagnetism in UCoGe. Physical Review Letters, 99(6):067006–4, 2007.

[99] S. R. Giblin. Private Communication, 2012.

[100] N. T. Huy and A. de. Vissier. Ferromagnetic order in U(Rh, Co)Ge. Solid State Communications, 149:703, 2009.

[101] P. de la Mora and O Navarro. Electronic structure of the ferromagnetic superconductor UCoGe from first principles. Journal of Physics: Condensed Matter, 20(285221):285221, 2008.

[102] M. Diviš. Electronic structure and magnetism of UCoGe from first principles. Physica B: Condensed Matter, 403(13-16):2505–2508, 2008.

[103] M. Samsel-Czekala, S. Elgazzar, P. M. Oppeneer, E. Talik, W. Walerczyk, and Troć. The electronic structure of UCoGe by *ab initio* and XPS experiment. J. Phys: Condens. Matter., 22:015503, 2010.

[104] K. Prokeš, E. Bruück, and V. Sechovsý. Melting of the antiferromagnetic structure in UNiAL near T_N. Physica B: Condensed Matter, 385:369, 2006.

[105] R. Troć and V. H. Tran. Magnetic properties of UT(Si, Ge) series. Journal of Magnetism and Magnetic Materials, 73:389, 1988.

[106] K. Prokeš, A. de Visser, Y. K. Huang, B. Fak, and E. Ressouche. Anomalous spin distribution in the superconducting ferromagnet UCoGe studied by polarized neutron diffraction. Phys. Rev. B., 2010.

[107] E. Hassinger, D. Aoki, G. Knebel, and J. Flouquet. Pressure-phase diagram of UCoGe by ac-susceptibility and resitivity measurements. Unpublished.

[108] N. T. Huy, D. E. de Nijs, Y. K. Huang, and A. de Visser. Unusual upper critical field of the ferromagnetic superconductor UCoGe. Physical Review Letters, 100:077002, 2008.

[109] N. T. Huy, Y. K. Huang, and A. de Visser. Effect of annealing on the magnetic and superconducting properties of single-crystalline UCoGe. Journal of Magnetism and Magnetic Materials, 321:2691, 2009.

[110] K. Deguchi, S. Ban, E. Osaki, I. Satoh, and N. K. Sato. Unusual Meissner state of the superconducting ferromagent UCoGe revealed by differential susceptibility mesurements with polycrystalline sample. Physica C, 470:S575, 2010.

[111] T. Okane, Y. Takeda, S.-i. Fujimori, K. Terai, Y. Saitoh, Y. Muramatsu, A. Fujimori, Y. Haga, E. Yamamoto, and Y. Onuki. Soft X-ray magnetic circular dichroism study of UFe_2. Physica B: Condensed Matter, 378:959, 2006.

[112] V. N. Antonov, B. N. Harmon, O. V. Andryuschenko, L. V. Bekenev, and A. N. Yaresko. Electronic structure and X-ray magnetic circular dichroism in uranium compounds. II. UTAl (T = Co, Rh, and Pt) intermetallics. Phys. Rev. B, 68:214425, 2003.

[113] A. Aguayo, I. I. Mazin, and D. J. Singh. Why Ni_3Al is an itinerant ferromagnet but Ni_3Ga is not. Phys. Rev. Lett., 92:147201, 2004.

[114] T. D. Haynes, I. Maskery, M. W. Butchers, J. A. Duffy, J. W. Taylor, S. R. Giblin, C. Utfeld, J. Laverock, S. B. Dugdale, Y. Sakurai, M. Itou, C. Pfleiderer, M. Hirschberger, A. Neubauer, W. Duncan, and Grosche F. M. Ferrimagnetism in Fe-rich $NbFe_2$. Phys. Rev. B., 85:115137, 2012.

[115] N. Tateiwa, K. Hanazono, T. C. Kobayashi, Amayam K., T. Inoue, K. Kindo, Y. Koike, N. Metoki, Y. Haga, R. Settai, and Y. Onuki. Magnetic properties of a presuure-induced superconductior UGe_2. J. Phys. Soc. Jpn., 70:2876, 2001.

[116] Y. Haga, M. Nakashima, R. Settai, S. Ikeda, T. Obuka, S. Araki, T. C. Kobayashi, N. Tateiwa, and Y. Onuki. A change of the Fermi surface across the metamagnetic transition under pressure in UGe_2. Journal of Physics: Condensed Matter, 14:L125, 2002.

[117] A. B. Shick, V. Janiš, V. Drchal, and W. E. Pickett. Spin and orbital magnetic state of UGe_2 under pressure. Physical Review B., 70:134506, 2004.

[118] A. Huxley, I. Sheikin, E. Ressouche, N. Kernavanois, D. Braithwaite, R. Calemczuk, and J. Flouquet. UGe_2: A ferromagnetic spin-triplet superconductor. Phys. Rev. B., 63:144519, 2001.

[119] Y. Sakurai, M. Itou, E. Yamamoto, Y. Haga, and Y. Onuki. Orbital-wise decomposition of magnetic Compton profiles in ferromagnetic uranium compound. J. Phys. Soc. Jpn., 75:96, 2006.

[120] N. Kernavanois, B. Greiner, A. Huxley, E. Ressouche, J. P. Sanchez, and J. Flouquet. Neutron scattering study of the ferromagnetic superconductor UGe_2. Phys. Rev. B., 64:174509, 2001.

[121] A. B. Shick and W. E. Pickett. Magnetism, spin-orbit coupling, and superconducting pairing in UGe_2. Phys. Rev. Lett., 86:300, 2001.

[122] T. Okane, J. Okamoto, K. Mamiya, S. Fujimori, Y. Takeda, Y. Saitoh, Y. Maramatsu, A. Fujimori, Y. Haga, E. Yamamoto, A. Tanaka, T. Honma, Y. Inada, and Y. Onuki. Soft X-ray absorption magnetic circular dichroism study of ferromagnetic superconductor UGe_2. Journal of the Physical Society of Japan, 75:024704, 2006.

[123] D. A. Sokolov, R. Ritz, C. Pfleiderer, T. Keller, and A. D. Huxley. Neutron scattering studies of the lattice expansion in a ferromagnetic superconductor UGe_2 under pressure. Journal of Physics: Conference Series, 273:012085, 2011.

[124] D. A. Sokolov, R. Ritz, C. Pfleiderer, T. Keller, and A. D. Huxley. Neutron scattering studies of the lattice expansion in a ferromagnetic superconductor UGe_2 under pressure. International Conference on Strongly Correlated Electron Systems, 273:012085, 2011.

[125] T. Sakon, S. Saito, K. Koyama, S. Awaji, I. Sato, T. Nojima, K. Katanabe, M. Motokawa, and N. K. Sato. Magnetic anisotropy study og UGe_2 in a static high magnetic field. Journal of Physics: Conference Series, 51:255, 2006.

[126] N. Kernavanois, P. Delmas de Réotier, A. Yaouane, J-P. Sanchez, V. Honkim $a$ki, T. Tschentscher, J. McCarthy, and O. Vogt. Orbital and spin magnetism in US comparison with USe and UTe. J. Phys: Condens. Matter, 13:9677, 2001.

[127] C. E. Guillaume. C. R. Acad. Sci., 125:235, 1897.

[128] E. Kisker, E. F. Wassermann, and C. Carbone. Evidene for the high-spin to low-spin state transition in ordered Fe_3Pt invar. Phys. Rev. Lett., 58:1784, 1987.

[129] T. Kiyama, K. Yoshimura, K. Kosuge, Y. Ikeda, and Y. Bando. Invar effect of $SrRuO_3$: Itinerant electron magnetism of Ru 4*d* electrons. Physical Review B, 54:R756, 1996.

[130] R. J. Weiss. Proc. R. Soc. Lond. A., 82:281, 1963.

[131] M. Matsushita, T. Inoue, I. Yoshimi, T. Kawamura, Y. Kono, T. Irifune, T. Kikegawa, and F. Ono. Anomolous variations in the volume of $Fe_{69}Ni_{31}$ Invar alloys under high pressure and temperatures. Phys. Rev. B., 77:064429, 2008.

[132] V. Crisan, P. Entel, H. Ebert, H. Akai, D. D. Johnson, and J. B. Staunton.

Magnetochemical origin for invar anomalies in iron-nickel alloys. Physical Review B, 66:014416, 2002.

[133] Y. Ito, J. Akimistu, M. Matsui, and S. Chikazumi. Magnetic form factor of $Fe_{0.66}Ni_{0.34}$ invar alloy. Journal of magnetism and magnetic materials, 10:194, 1979.

[134] P. J. Brown, K.-U. Neumann, and K. R. A. Ziebeck. The temperature dependence of the magnetization distribution in $Fe_{65}Ni_{35}$ invar: incompatibility of the two-state model. J. Phys.: Condens. Matter, 13:1563, 2001.

[135] M. van. Schilfgaarde, I. A. Abrikosov, and B. Johansson. Origin of the Invar effect in iron-nickel alloys. Nature, 400:46, 1999.

[136] J. W. Taylor, J. A. Duffy, and S. R. Giblin. Private Communication, 2012.

[137] J. W. Taylor, J. A. Duffy, A. M. Bebb, J. E. McMarthy, M. R. Lees, M. J. Cooper, and D. N. Timms. Spin-polarized electron momentum density distributions in the Invar system Fe_3Pt. Phys. Rev. B., 65:224408, 2002.

[138] G. Srajer, C. J. Yahnke, Haeffnerm D. R., D. M. Mills, L. Assoufid, B. N. Harmon, and Z. Zuo. Magnetic Compton scattering of the Invar alloy Fe_3Pt. J. Phys.: Condens. Matter, 11:L253, 1999.

[139] J. A. Duffy. Private Communication, 2009.

[140] B. Glaubitz, S. Buschhorn, F. Brüssing, R. Abrudan, and H. Zabel. Development of magnetic moments in $Fe_{1-x}Ni_x$-alloys. J. Phys.: Condens. Matter, 23:254210, 2011.

[141] P. Aebi, T. J. Kreutz, J. Osterwalder, R. Fasel, P. Schwaller, and L. Schlapbach. *k*-space mapping of majority and minority bands on the Fermi surface of nickel below and above the Curie temperature. Phys. Rev. Lett., 76:1150, 1996.

[142] P. J. Brown, H Capellman, J. Déportes, D. Givord, S. M. Johnson, and K. P. A. Ziebeck. The paramagnetic response of nickel at high temperature. J. Physique, 47:491, 1986.

[143] J. B. Staunton and B. L. Gyorffy. Onsager cavity fields in itinerant-electron paramagnets. Phys. Rev. Lett., 69:371, 1992.

[144] Y. Tanaka, I. Matsumoto, H. Adachi, and H. Kawata. Temperature dependence of magnetic Compton profiles of Ni. Jpn. J. Appl. Phys., 38s:389, 1999.

[145] P. Genoud, A. A. Manuel, and E Walker. Spin-polarised 2D ACAR in nickel across the Curie temperature. J. Phys: Condens. Matter, 3:4201, 1991.

[146] P. J. Brown, J. Deportes, K.-U. Neumann, and K. R. A. Ziebeck. High-temperature magnetisation distribution in nickel. J. Magn. Magn. Matt., 104:2083, 1992.

[147] T. Kachel, N. Pontius, C. Stamm, M. Wietstruk, E. F. Aziz, H. A. Dürr, W. Eberhardt, and F. M. F. de Groot. Transient electronic and magnetic structures of nickel heated by ultrafast laser pulses. Phys. Rev. B., 80:092404, 2009.